Schweizerische Eidgenossenschaft
Confédération suisse
Confederazione Svizzera
Confederaziun svizra

Federal Department of the Environment, Transport, Energy and Communications DETEC

Swiss Federal Office of Energy SFOE
Energy Research and Cleantech Division

Report dated 08.10.2024, revised 3.6.2025

Efficient Small-Scale Methanol Synthesis from Biogas

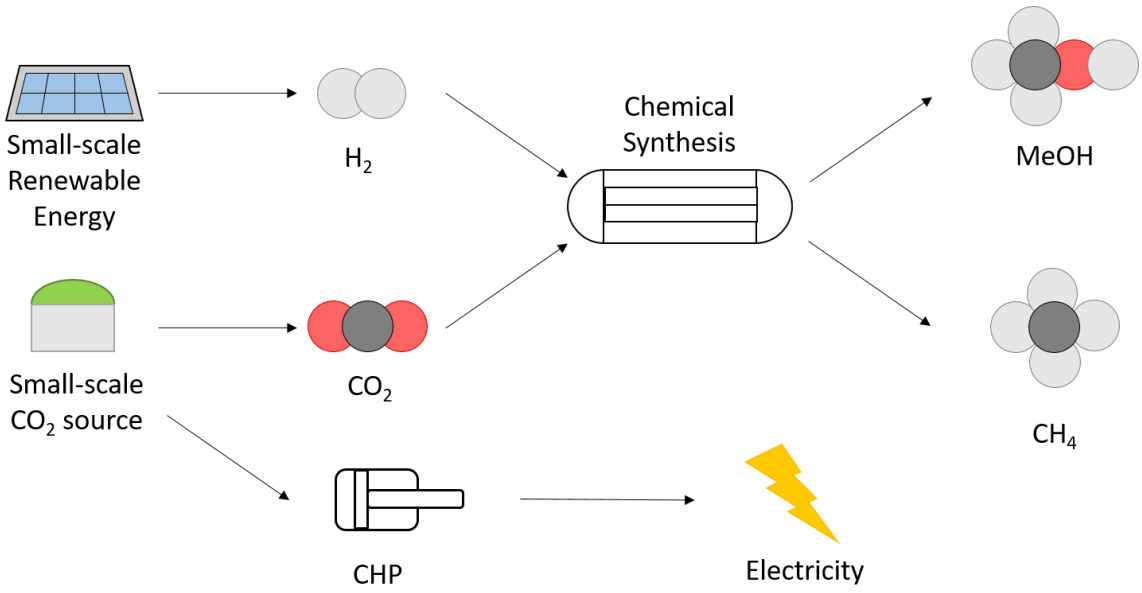

Source: ©E. Moioli 2021

Date: 8th October 2024

Location: Bern

Publisher:
Swiss Federal Office of Energy SFOE
Energy Research and Cleantech
CH-3003 Bern
www.bfe.admin.ch

Co-financing: ETH Rat
Synfuels initiative of the ETH Rat
Hirschengraben 3
CH-3011 Bern, Switzerland
www.ethrat.ch

Subsidy recipient:
Paul Scherrer Institut
Forschungstrasse 111, CH-5232 Villigen PSI
www.psi.ch

Authors:
Emanuele, Moioli, Paul Scherrer Institut, emanuele.moioli@psi.ch
Chiara Berretta, Paul Scherrer Institut, chiara.berretta@psi.ch
Tilman, Schildhauer, Paul Scherrer Institut, tilman.schildhauer@psi.ch

SFOE project coordinators:
Carina Alles, carina.alles@bfe.admin.ch
Sandra Hermle, Sandra.hermle@bfe.admin.ch

SFOE contract number: SI/502147
The authors bear the entire responsibility for the content of this report and for the conclusions drawn therefrom.

Zusammenfassung

Die Nutzung von Biogas ist ein wesentliches Element für die Entwicklung eines sauberen und erneuerbaren Energiesystems. Trotz der breiten Verfügbarkeit dieses Rohstoffs gibt es keine marktbeherrschende Standardtechnologie für die Verwertung von Biogas. Die vorliegende Studie vergleicht die Möglichkeiten der Verwertung von Biogas in Strom, Methan und Methanol. Zunächst werden die drei Technologien zur Erzeugung dieser Energieträger verglichen, um die Zielkosten für Biogas zu ermitteln. Anschließend werden die Möglichkeiten zur Erzielung eines zusätzlichen Gewinns durch die Kopplung von Biogasnutzung und Energiespeicherung mittels Power-to-X bewertet. Es zeigte sich, dass die Auswahl der besten Technologie stark von den Marktbedingungen abhängt. In jedem Fall erscheinen flexible Verfahren, die die Verwertung des verfügbaren biogenen CO_2 einschließen, günstiger, da sie eine Anpassung der Produktlieferung an die Marktbedingungen ermöglichen. Auf der Grundlage der angenommenen Marktbedingungen (d.h. billiger Strom im Sommer und teurer im Winter) wurde festgestellt, dass Methan der Energieträger der Wahl für die Stromerzeugung ist, während Methanol die beste Lösung für die saisonale H_2-Speicherung ist. Die Studie konzentriert sich dann auf die Methanolerzeugung und untersucht, welcher Prozessweg sich am besten für Anwendungen im kleinen Maßstab eignet. Es wurde festgestellt, dass die lokale Dampfreformierung die beste Technologie in Bezug auf den Prozessgewinn ist. Allerdings hat diese Technologie einen erheblichen Kohlenstoff-Fußabdruck, der keine wesentliche Verbesserung der Nachhaltigkeit der Methanolproduktion ermöglicht. Daher wurde festgestellt, dass die direkte Methanolerzeugung aus biogenem CO_2 und erneuerbarem H_2 vorteilhaft wäre, vorausgesetzt, dass neue Technologien entwickelt werden, die die Investitionskosten für diesen Prozessweg senken.

Résumé

La valorisation du biogaz est un élément essentiel du développement d'un système énergétique plus propre et renouvelable. Malgré la grande disponibilité de cette matière première, une technologie standard de valorisation du biogaz n'est pas dominante sur le marché. Cette étude compare les possibilités de valorisation du biogaz en électricité, méthane et méthanol. Tout d'abord, les trois technologies permettant de produire ces vecteurs énergétiques sont comparées afin de déterminer le coût cible du biogaz. Ensuite, la possibilité d'obtenir un bénéfice supplémentaire en couplant la valorisation du biogaz et le stockage de l'énergie via le power-to-X est évaluée. Il a été constaté que le choix de la meilleure technologie dépend fortement des conditions du marché. Dans tous les cas, les processus flexibles incluant la valorisation du CO_2 biogénique disponible semblent plus appropriés, car ils permettent d'adapter la livraison du produit aux conditions du marché. Sur la base des conditions de marché supposées (c'est-à-dire une électricité bon marché en été et chère en hiver), il a été déterminé que le méthane est le vecteur énergétique de choix pour la production d'électricité, tandis que le méthanol est la meilleure solution pour le stockage saisonnier d'H_2. L'étude se concentre ensuite sur la production de méthanol, en évaluant quelle voie de procédé s'adapte le mieux aux applications à petite échelle. Il s'avère que le reformage à la vapeur localisé est la technologie la plus performante en termes de rentabilité du procédé. Cependant, cette technologie a une empreinte carbone importante, ne permettant pas une amélioration significative de la durabilité de la production de méthanol. Par conséquent, il a été déterminé que la production directe de méthanol à partir de CO_2 biogénique et de H_2 renouvelable serait bénéfique, à condition que de nouvelles technologies réduisant les coûts d'investissement de cette voie de procédé soient développées.

Summary

Biogas utilization is an essential element of the development of a cleaner and renewable energy system. Despite the broad availability of this raw material, a standard technology for biogas

valorisation is not dominant on the market. This study compares the possible valorisation of biogas in electricity, methane and methanol. First, the three technologies to produce these energy carriers are compared to determine the target biogas cost. Then, the possibility of achieving additional profit by coupling biogas utilisation and energy storage via power-to-X are assessed. It was found that the selection of the best technology strongly depends on the market conditions. In any case, flexible processes including the valorisation of the available biogenic CO_2 appear more convenient, because they allow the adaptation of the product delivery to the market conditions. On the base of the assumed market conditions (i.e. cheap electricity in summer and expensive in winter), it was determined that methane is the energy carrier of choice for electricity production, while methanol is the best solution for seasonal H_2 storage. The study then focused on methanol production, assessing which process route adapts best to small-scale applications. It was found that the localized steam reforming is the best performing technology in terms of process profit. However, this technology has an important carbon footprint, not allowing a significant improvement of the methanol production sustainability. Hence, it was determined that the direct methanol production from biogenic CO_2 and renewable H_2 would be beneficial, provided that new technologies reducing the investment costs of this process route are developed.

Contents

Zusammenfassung **3**

Résumé **3**

Summary **3**

Contents **5**

Abbreviations **6**

1 Introduction **8**

1.1 Background information and current situation 8

1.2 Purpose of the project 9

2 Procedures and methodology - Modelling **9**

3 Activities and results - Modelling **20**

4 Experimental procedure and methodology **34**

5 Experimental results **38**

6 Evaluation of results **63**

7 Next steps **65**

8 National and international cooperation **65**

9 Communication **65**

10 Publications **65**

11 References **66**

Abbreviations

AEL = Alkaline Electrolyser

CAPEX = Capital Expenditures

CEPCI = Chemical Engineering Plant Cost Index

CHP = Combined Heat and Power Production

CNG = Compressed Natural Gas

IRENA = International Renewable Energy Agency

IRR = Internal Rate of Return

MeOH = Methanol

MI = Methanol Institute

OPEX = Operative Expenditures

PtG = Power to Gas

PtMeOH = Power to Methanol

PtX = Power to X

RWGS = Reverse Water Gas Shift Reaction

SNG = Synthetic Natural Gas

STY = Space Time Yield

TRL = Technology Readiness Level

Uppercase letters

C_{BM} = Bare Module Cost (CHF)

$C_{BM,today}$ = Current Bare Module Cost (CHF)

C_p = Equipment Purchase Cost (CHF)

E_i = the electrical output of the system (kW)

F = Stoichiometric Factor (H_2:CO_2)

F_C = Cost Factor

F_e = Exchange Rate

F_M = Material Factor

F_P = Pressure factor

Q_{Bio} = the volumetric flowrate of biogas (m^3/h)

R_T = Process income (CHF/y)

Re = Reynolds number

S_p = surface area of the catalyst particle (m^2)

U_T = global heat transfer coefficient ($W/K/m^2$)

X_i = Conversion of the component i

V_p = volume of the catalyst particle (m^3)

Y_i = Yield of the component i

Lowercase letters

a = Plant Lifetime (years)

d = reactor diameter (m)

i = Interest Rate (%)

k_i = local heat transfer coefficient ($W/K/m^2$)

n = order of reaction

r = reactor radius (m)

Greek letters

η = efficiency factor

ν_i = stoichiometric coefficient of the component i

ρ_i = density of the component i (kg/m^3)

ϕ = Thiele modulus

ΔH^R = reaction enthalpy (kJ/mol)

1 Introduction

1.1 Background information and current situation

Currently, an important share of the organic waste produced in urban environments and in agriculture is sent to landfills or anaerobic digestion plants. This leads to significant environmental concerns linked to the gas emissions from these plants [1]. However, this product gas can be valorised in several ways, leading to the reutilisation of the original carbon coming from the waste feedstock. Biogas coming from anaerobic digestion (AD) generally contains methane (30–70% CH_4), carbon dioxide (30–70% CO_2), and other impurities such as hydrogen sulphide (0–2000 ppm H_2S) [2]. For a full utilization of biogas, this must be cleaned and processed to obtain a product gas with acceptable heating value. This can be in principle done by two ways: either by removing the CO_2 from the stream or by using CO_2 in the production of valuable products [3].

A common biogas valorisation strategy is the production of electricity and heat from biogas combustion. This process is commonly referred to as combined heat and power production (CHP) [4]. The development of this technology was fostered by the simplicity of use and by significant incentives, allowing the sale of the products at a preferential rate [5]. However, the CHP technology is affected by a low efficiency due to significant heat losses (up to 40 %) [3] and it is strongly dependent on the availability of incentives. Additionally, the production of electricity cannot be adapted to the demand without gas storage, hence making CHP a less flexible technology. An alternative process is biogas upgrading. This process produces a concentrated methane stream by removing CO_2 from biogas. The final product is often referred to as biomethane. CO_2 separation can be performed by chemical or physical processes, frequently by scrubbing, pressure swing adsorption or membrane separation [6]. The main advantages of this technology are related to the high efficiency and to the production of an energy carrier that can be directly injected in the existing infrastructure (i.e. in the gas grid) and can eventually be stored and used as fuel in compressed form (compressed natural gas, CNG) or liquefied form (Liquefied Biogas, LBG; bio-LNG) [7]. However, this technology is affected by significant CO_2 emissions (due to the release of the CO_2 contained in biogas). The utilization of this biogenic CO_2 in the production of additional valuable products would be of interest in numerous process [8]. An appropriate management of biogenic CO_2, connected with capture and storage, can also lead to negative CO_2 emissions [9]. The largest focus of research is linked to the coupling of biogas upgrading and power-to-X (PtX), which means the reaction of biogenic CO_2 with renewable H_2 produced from renewable energy, with the aim of synthesizing valuable products [10].

Most of the research programs in the context of coupling Power-to-X with use of biogenic CO_2 are currently devoted to the production of synthetic methane. However, methane is a gaseous fuel and can be efficiently stored and used only in presence of an appropriate infrastructure (gas grid) or as liquefied LBG with the related logistics. In this project, we explore an alternative to methane production: the synthesis of methanol. Methanol is a liquid fuel and can be used as a substitute of gasoline (e.g. as maritime fuel), serve as chemical platform chemical (e.g. for the production of plefins, formaldehyde etc., or Sustainable aviation fuels, SAF), and it can be easily transported. In this way, biogas plants not directly connected to the natural gas grid can be used for energy storage purposes. However, standard methanol production systems are not suitable for such a small scale. Therefore, new reactor technologies have to be developed, allowing for a profitable operation of this type of systems. The determination of appropriate systems for the small-scale methanol synthesis in the context of Power-to-X is still an open question in the technical literature.

1.2 Purpose of the project

This project is aimed at determining the best solutions for coupling Power-to-X and biogenic CO_2 utilization. In particular, the projects wants to understand the most appropriate energy carriers to produce according to the market conditions and the target use of biogas and of the final products.

The first goal (determination of the potential of methanol production from biogas) is achieved by a series of consecutive steps. In the first place, the project aims at answering the research question: “How does the process profit of biogas valorisation in methanol compare to CHP and compressed natural gas (CNG) production?” This question is addressed by a detailed analysis of the three different processes in various conditions. Primarily, the profitability of electricity by CHP, CNG and methanol production is determined according to the current market conditions and to the possible future market perspective. Second, the profitability of using biogas as a platform for electricity or hydrogen storage is determined. The second research question is: “What is the production cost of methanol from biogas?” This question is answered by comparing three different process alternatives:

- Methanol production via biogas steam reforming;
- Methanol production from biogenic CO_2 via power-to-methanol;
- Methanol production by centralized reforming of biomethane (concentrating the biogas from several biogas plants).

This analysis is complemented by the comparison of the methanol production from biogas with the Power-to-methanol process from pure CO_2 (e.g. from point capture or from direct air capture).

The second goal (development of a new technology for power-to-methanol from biogas) is achieved by a combination of modelling and experimental activities. First, various reactor technologies for the downscaling of methanol production are analysed by detailed reactor modelling, determining the limits of the existent technologies in the new conditions. In this way, it is possible to define the technical solutions to overcome these limits, developing new reactor technology (sorption enhanced methanol synthesis) specifically designed for small-scale. The results of the modelling phase determine the specific reactor type to test in laboratory, i.e. testing of sorbents and catalysts as well as proof of the fluid-dynamic feasibility. The new reactor technology will be the final product of this project.

2 Procedures and methodology - Modelling

In a first section, the generic reactor model (Series of fixed bed reactors with intermediate product condensation) for the systemic analysis is presented, together with the economic calculations and assumptions.

In the second section, the concepts and the more detailed models for three different types of reactors for sorption-enhanced methanol synthesis are described.

The results of both modelling sections (systemic analysis and detailed sorption enhanced reactors) are presented in chapter 3; while the experimental procedures and results are described in chapters 4 and 5, respectively.

Procedures for systemic analysis

Modelling of fixed bed reactors in series with intermediate product condensation

In the techno-economic assessment, the reactors are modelled with a pseudo-homogeneous 1D model, with the intra-phase diffusion accounted with the Thiele modulus method. The coolant temperature is considered constant. The mass and heat balances are calculated as:

$$\frac{d(uc_i)}{dz} = \nu_i \eta \rho_b r \quad (1)$$

$$(u\rho_b c_{tot})\frac{dT}{dz} = \nu_i \eta \rho_b r(-\Delta H_R) + \frac{4}{d_{tube}} U_T (T - T_w) \quad (2)$$

The kinetics models used are from Xu and Froment [11] for methane steam reforming, from Koschany et al. [12] for CO_2 methanation and from Vanden Bussche and Froment [13] for methanol synthesis.

For all the reactors, the catalyst efficiency factor is calculated via the Thiele modulus:

$$\phi = \frac{V_p}{S_p}\sqrt{\frac{n+1}{2}\cdot\left(\frac{kc_{i,s}^{n-1}}{D}\right)} \quad (3)$$

$$\eta = \frac{3}{\phi^2}(\phi\coth(\phi) - 1) \quad (4)$$

The heat transfer coefficient (in W/m^2K) is calculated considering the transport phenomena on tube and shell side, as well as the conductivity of the tube:

$$\frac{1}{U_A} = \frac{1}{k_i} + \frac{k_c}{\ln\left(\frac{r_i}{r_e}\right)} + \frac{1}{k_e} \quad (5)$$

k is calculated considering a stagnant and a dynamic contribution:

$$k = k_0 + 0.024 \cdot \frac{l \cdot Re}{d_p} \quad (6)$$

The explanation of symbols is reported in the 'Abbreviations' section.

CHP system modelling

The CHP system is modelled according to the methodology developed in [14]. The electrical output is modelled as:

$$E_{CHP} = \eta_{CHP} \cdot Q_{Bio} \cdot HHV_{Bio} \quad (7)$$

Where E_{CHP} is the electrical output of the system (kW_{el}), η_{CHP} is the efficiency of the CHP plant (kW_{el}/kW_{HHV}), Q_{Bio} is the volumetric flowrate of biogas Nm^3/h and HHV_{Bio} the heating value of biogas (kWh_{HHV}/Nm^3).
The capital cost is accounted as:

$$C_{CHP} = C_C \cdot E_{CHP} \quad (8)$$

C_{CHP} is the total installation cost of the CHP system, C_C is the average cost of a new CHP system per kWh. This mathematical relationship is based on the real market data recorded by the US Department of Energy [15]. The annual operation and maintenance costs are accounted as 5% of the installation cost.

Biogas upgrading modelling

Among the possible technologies for biogas upgrading, it was found that water scrubbing is the most suitable technology for the case here considered. Hence, the techno-economic performance was calculated as follows [16]:

$$P_{BM} = \eta_{met} \cdot Q_{Bio} \cdot (HHV_{Bio} - \eta_{ug}) \quad (9)$$

Where P_{BM} is the biomethane output of the system (kW), η_{ug} is the methane efficiency, Q_{Bio} is the volumetric flowrate of biogas, HHV_{Bio} the heating value of biogas and η_{ug} is the upgrading efficiency. The upgrading efficiency accounts for the energy required for the operation (solvent regeneration and utilities) and the product compression, as shown in equation 4:

$$\eta_{ug} = \eta_{op} + \eta_{comp} \quad (10)$$

η_{met} accounts for the methane losses in the operation (methane lost with the CO_2-rich stream). The efficiency values are reported in table 1. The installation cost of the water scrubbing system is calculated according to [6]. The capital cost includes the scrubbing unit, the compressor and the post treatment units. The operative costs include the biogas cost, the process water, electricity and operation and maintenance (corresponding to 5% of the investment costs).

Table 1 Efficiency values used in the assessment of biogas upgrading

Efficiency term	Value	Source
η_{op} (kWh/ m^3)	0.30	[16]
η_{met} (m^3_{out}/ m^3_{in})	0.98	[6]
η_{comp} (kWh/ m^3)	0.32	[3]

Power-to-X economic assessment

The equipment cost is calculated on the base of the dimensions determined in the modelling phase. The capital cost is accounted as:

$$C_{BM,k} = C_{pur} \cdot F_{BM}, with\ F_{BM} = f(F_M, F_P) \quad (11)$$

Where C_{BM} is the bare module cost, C_{pur} is the purchase cost and F_{BM} is the bare module factor, accounting for the material of the equipment and for the pressure of the system. The bare module costs are calculated for each process unit k. The costs and factors are retrieved from literature [17]. The electrolyser cost is accounted as 1200 CHF/kWh. The purchase cost of the reformer is calculated according to [18]. The bare module costs are used to calculate the installation costs, by multiplying for a plant cost factor (including supplementary costs, such as piping, instruments, electrical connections, engineering and buildings). Additionally, the costs are actualized by use of the CEPCI index. The resulting installed cost is:

$$C_{tot}^{inv} = \sum_{k=1}^{NE} C_{BM,k} \cdot \frac{CEPCI_{current}}{CEPCI_{ref}} \cdot (1 + F_{PC}) \quad (12)$$

The CEPCI index $\left(\frac{CEPCI_{current}}{CEPCI_{ref}}\right)$ is 1.548 (value for January 2019). The total plant cost factor is 1.13. For the installation costs, electrolyser, reactors, compressors, membranes and ancillary units were considered. The operative costs include biogas, electricity, process water, operation and maintenance (2.5% of the installed cost of electrolyser and 5% of the remaining units).

Flexible processes

The analysed processes are divided into two categories, here named as winter and summer mode. In winter mode, no additional electricity is needed in the process (i.e. no energy storage is performed). In this case, the process is operated in the same way during the entire year. Among these processes, CHP, biogas upgrading and methanol production via biogas steam reforming are accounted. In the summer mode, electricity is used to convert the biogenic CO_2 into valuable products, when the electrolyser can be operated in a convenient way. The operation time of the summer mode is calculated as 6000 h/y. This value is calculated based on the number of hours with electricity cheaper than 0.05 CHF/kWh in Switzerland in 2019 [19]. The flexible processes integrate the summer and winter mode, operating the former mode when cheap electricity is available and the latter when this is not available. In this way, it is possible to increase the operating hours of the processes performing energy storage, with a limited increase in the investment cost. The schematic description of the flexible operations is shown in figure 1 (methane) and 2 (methanol).

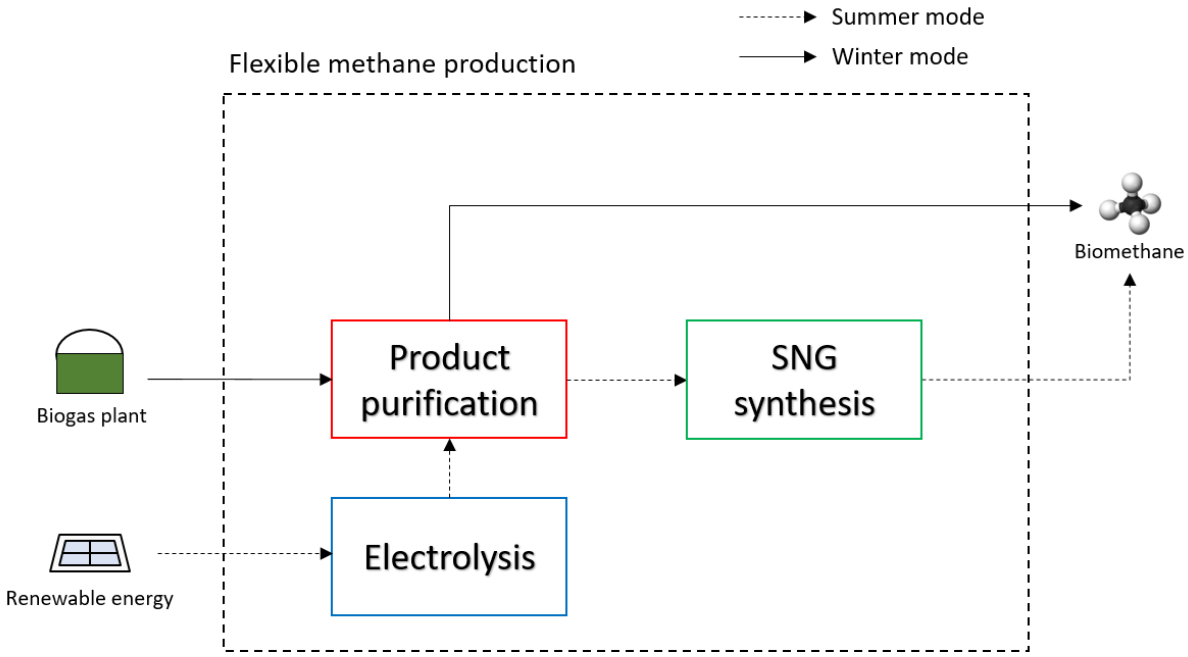

Figure 1 Process scheme of the flexible biomethane production

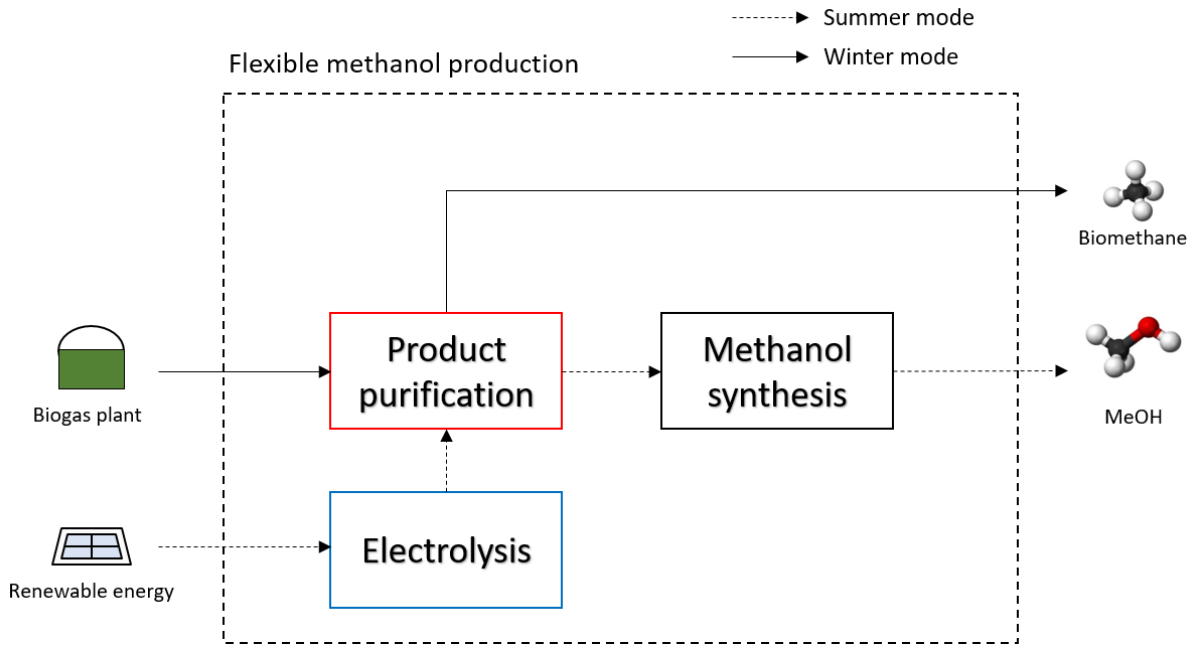

Figure 2 Process scheme of the flexible biomethanol production

Benchmark of the methanol synthesis processes

In order to assess the differences between the designed methanol synthesis strategies from biogas and the existing methanol production processes, the techno-economic performance of the large-scale methanol production via natural gas reforming is calculated. The schematic representation of the compared processes is reported in figure 3. The main benchmark process is the centralized methanol synthesis from steam reforming (process a). In this case, several biogas plants produce biomethane by biogas upgrading, so that sufficient gas is available for the operation of the centralized process (with a size of several thousand tons of methanol produced). Consequently, the large-scale production can take advantage of the state-of-the-art process integration strategies, allowing for significant cost savings. The process modelling follows the methodology exposed by Collodi et al. [20] The process is also representative of a centralized process compensating the CO_2 emissions of natural gas by the purchase of certificates. The processes synthesizing methanol via biogas steam reforming (process b in figure 3) and via power-to-methanol with biogenic CO_2 (process c in figure 3) are assessed according to the same methodology used in the previous sections.

Economic assumptions

The results of the techno-economic assessment depend on the price and value of the various products involved in the processes. Additionally, the economic indicators depend on the financial conditions considered. In order to assess the economic performance of the processes, the discounted cash flow was calculated considering a rate of 6% and a plant lifetime (a) of 15 years. With these values and from the installation cost of the equipment, it is possible to determine the capital expenditures (CAPEX):

$$CAPEX = C_{tot}^{inv} \cdot \left(\frac{((1+i)^a \cdot i)}{(1+i)^a - 1}\right) \quad (13)$$

Several economic indicators were used according to the specific needs of the analysis. The biogas break-even price is the price of biogas for which the net present value (NPV) of the various solution equals zero.

Hence, the formula is:

$$NPV\ (CHF) = f(C_{bio}^{BE}) = \frac{\sum_1^t R_t}{(1+i)^t} = 0 \quad (14)$$

Where C_{bio}^{BE} is the biogas break-even price, i is the discount rate and R_t is the cash flow at the year t:

$$R_t = Income - OPEX - CAPEX \quad (15)$$

The production cost (C_{prod}) is defined as:

$$C_{prod} = (OPEX + CAPEX)/P_{prod} \quad (16)$$

P_{prod} is the total energy content of the product. From the production cost, it is possible to determine the potential profit (G_p):

$$G_p = E_{prod} - C_{Prod} \cdot P_{prod} \quad (17)$$

E_{prod} is the selling price of the product. The product values are reviewed in table 3. The price of biogas is 0.06 CHF/kWh. This price is not directly representative of the biogas production cost, but as an opportunity cost referring to the possibility of valorising biogas in CHP [21]. The assumed biomethane price is 0.12 CHF/kWh, as currently offered on the market in Switzerland [22]. The price of biomethanol is set as 0.20 CHF/kWh, from the possible utilization of methanol as an additive to gasoline fuel (price of gasoline in Switzerland in 2019). The price of electricity is considered to change between a low value when electricity is abundant (summer case) and a high value when electricity is scarce (winter case). The summer value is 0.05 CHF/kWh, which was the average price in 2019 in Switzerland during the 6000 hypothesized hours of operation of the power-to-X system. The winter value was calculated by imposing a 200 CHF/t_{CO2} carbon tax in addition to the electricity cost reported by Swissgrid (prices referred to 2019) [19].

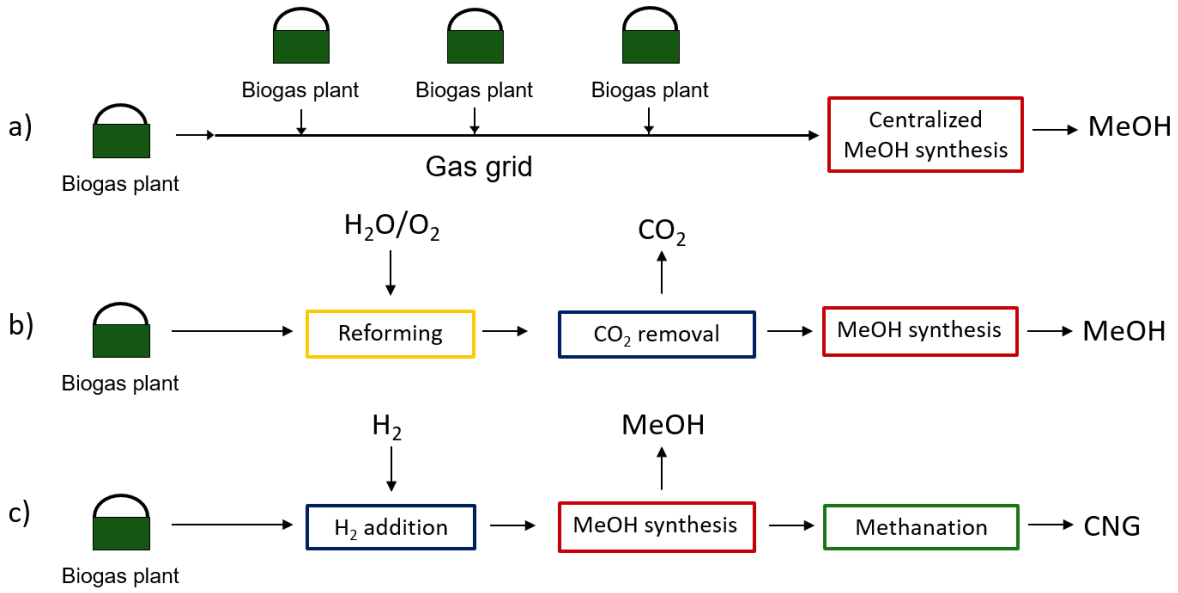

Figure 3 Processes compared in the benchmarking procedure: a) the centralised methanol production from biomethane; b) the methanol synthesis via localized biogas steam reforming; c) the methanol synthesis via power-to-methanol process with biogenic CO_2

Table 2 The assumed values for the compounds and for electricity

Item	Price (CHF/kWh)
Biogas	0.06
Biomethane	0.12
Biomethanol	0.20
Electricity (summer)	0.05
Electricity (winter)	0.20
Hydrogen (winter)	0.15

Procedure for detailed reactor modelling

The details of the three reactor types analysed are shown in figure 4. The dynamic fixed bed reactor is composed of two reactors in parallel, one operated in reaction mode and the other in regeneration mode. The regeneration is operated by feeding an inert gas (e.g. N_2) and by keeping the reactor warm by use of the waste heat coming from the reactor in reactive mode. The regeneration step is not modelled in detail. The entrained flow reactor is operated by entraining both catalyst and sorbent. When leaving the reactor, the particles are separated from the gas phase and fed to regeneration unit, which is operated with an inert gas and using the waste heat from the methanol reactor. The regenerated sorbent is then fed back, together with the catalyst, to the main reactor. The entrained/fluidised bed reactor generates two different flow patterns in the reactor by using different particle sizes. The catalyst remains in suspension in the reactor (fluidised phase), while the sorbent is sufficiently small to be entrained from the gas. The entrained sorbent is separated from the gas phase and regenerated in analogy to the entrained flow reactor.

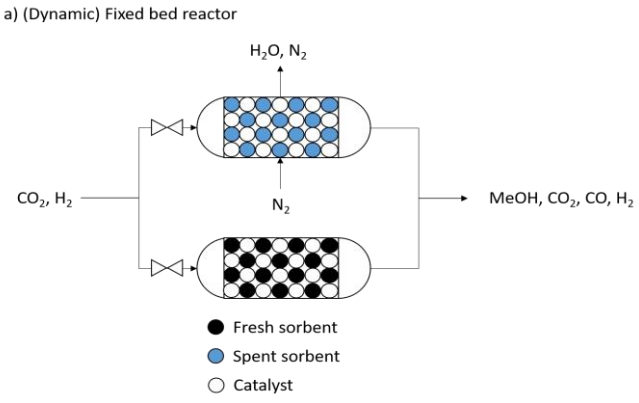

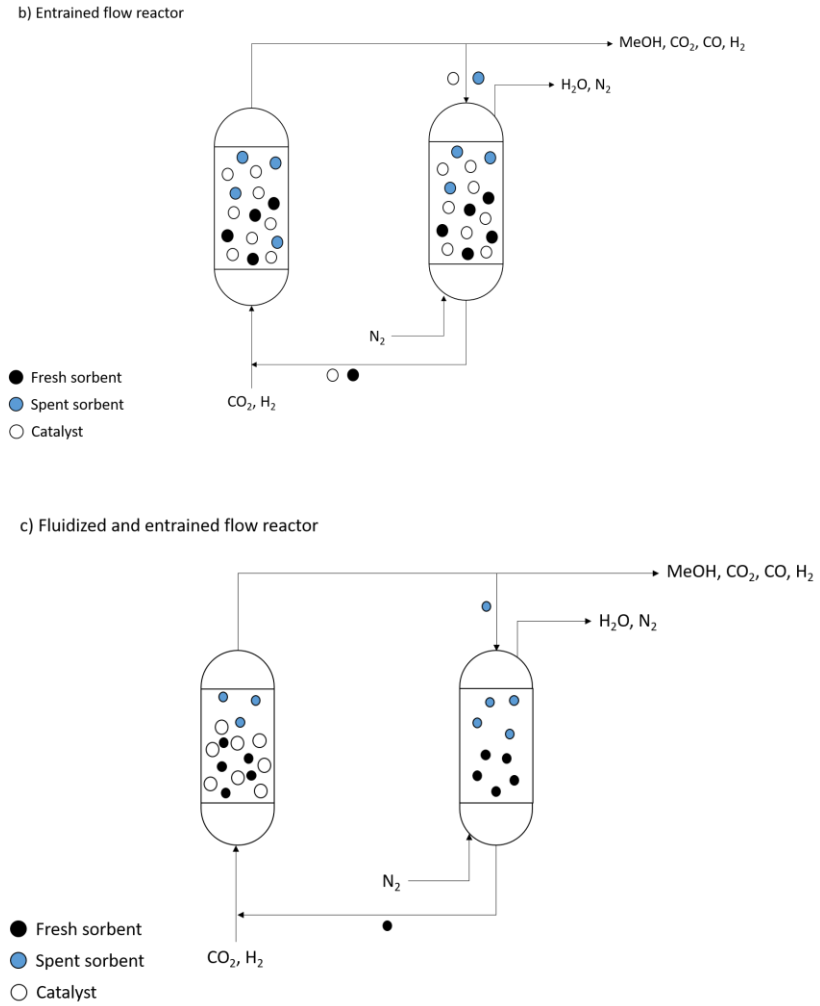

Figure 4. The three reactor types analysed: a) dynamically operated fixed bed reactor; b) entrained flow reactor; c) fluidised bed (catalyst) and entrained flow (sorbent) reactor

Dynamic fixed bed reactor

The dynamic fixed bed reactor has a volume of 20 m^3 and a diameter of 0.01m. The total feed is 20 kmol/h of a stoichiometric 1:3 CO_2:H_2 gas mixture at 30 bar. The reactor is composed of 5000 pipes in parallel. The sorbent to catalyst ratio is 1:1. The kinetic model for the methanol synthesis is from Vanden Bussche and Froment [21] and the sorbent model is from Maksimov et al. [16]. The model is as follows:

Mass balance for component *i* (except H_2O):

$$\frac{\partial y_i}{\partial t} = \frac{\varepsilon_b}{\varepsilon_t} v_0 \frac{\partial p_i}{\partial z} - \frac{\rho_{cat} RT}{\varepsilon_t} \sum_{j=1}^{NR} \eta \nu_{i,j} R_j (1 - \varphi_c) \quad (3)$$

Mass balance for H_2O:

$$\frac{\partial y_{H2O}}{\partial t} = \frac{\varepsilon_b}{\varepsilon_t} v_0 \frac{\partial p_i}{\partial z} - \frac{\rho_{cat} RT}{\varepsilon_t} \sum_{j=1}^{NR} \eta \nu_{H2O,j} R_j (1 - \varphi_c) - \frac{\rho_{ads} RT}{\varepsilon_t} \frac{\partial q_{H2O}}{\partial t} \quad (4)$$

Energy balance:

$$\rho_{tot} c_p \frac{\partial T}{\partial t} = \frac{c_p \varepsilon_b}{R} v_0 \frac{\partial T}{\partial z} - \frac{\rho_{cat} RT}{\varepsilon_t} \sum_{j=1}^{NR} \eta R_j \left(-\Delta H_j^R\right)(1-\varphi_c) - \rho_{ads}(-\Delta H_{ads}) \frac{\partial q_{H2O}}{\partial t} - \frac{2U}{r_{in}}(T - T_w) \quad (5)$$

Water absorption model:

$$\frac{\partial q_{H2O}}{\partial t} = k_w (q^*_{H2O} - q_{H2O}) \quad (6)$$

Equilibrium loading of the adsorbent:

$$q^*_{H2O} = \frac{m_{H2O} b_{H2O} p_{H2O}}{1 + m_{H2O} p_{H2O}} \quad (7)$$

For the calculation of the gas velocity, the continuity equation is used. The catalyst efficiency is calculated with the Thiele modulus for a catalyst pellet. The parameters of the system are obtained from [16] and reported in table 1.

Entrained flow reactor

The entrained flow reactor is simulated with a 1D model, assuming steady state conditions, negligible axial and radial dispersion and uniform water adsorption following the formulation in [20]. The intraphase limitations are considered via the Thiele modulus. The superficial velocity of the gas is 0.3 m/s. The particles diameter is 0.00003 m. The reactor is diameter is 1.5 m and the length is 7 m (reference case). This corresponds to a flow rate of 80 kmol/h in the reference case. The material balances are expressed as:

$$\frac{dF_i}{dz} = (1-\varphi_c)\rho_s \varepsilon_{sd} AH \sum_{j=1}^{NR} \eta \nu_{\mathrm{I,j}} R_j \quad (8)$$

The water balance is expressed as:

$$\frac{dF_{H2O}}{dz} = (1-\varphi_c)\rho_s \varepsilon_{sd} AH \sum_{j=1}^{NR} \eta \nu_{\mathrm{H2O,j}} R_j - \varphi_c \varepsilon_{sd} A G_s q_{H2O} \quad (9)$$

The energy balance is:

$$\sum_{i=1}^{NS} F_i c_{p,i} \frac{dT}{dz} = (1-\varphi_c)\rho_s \varepsilon_{sd} AH \sum_{j=1}^{NR} \eta \nu_{\mathrm{I,j}} R_j - U\pi D(T - T_w)H \quad (10)$$

The solid circulating rate (G_s) is given by:

$$G_s = U_S^0 \rho_s \quad (11)$$

U_S^0 is the superficial solids velocity. The momentum balance is written assuming negligible gas gravity, wall friction and gas velocity variation. Under these assumptions, the balance results in the formula [22]:

$$(-\Delta P)_{dense\ bed} = g\rho_s \varepsilon_{sd} H + \rho_s U_g \varepsilon_{sd} U_t \quad (12)$$

U_g is the gas velocity in the dense region, expressed as:

$$U_g = \frac{U_g^0}{1+\varepsilon_{sd}} \quad (13)$$

U_g^0 is the superficial gas velocity. ε_{sd} can be calculated by assuming that a critical holdup value exists after which the solids holdup becomes independent from the superficial gas velocity (dense region filling the entire riser). Hence, ε_{sd} is calculated as [23]:

$$\frac{\varepsilon_{sd}}{\varepsilon'_s} = 1 + 6.14 \times 10^{-3} \left(\frac{U_g^0}{U_s^0}\right)^{-0.23} \left(\frac{\rho_s - \rho_g}{\rho_g}\right)^{1.21} \left(\frac{U_g^0}{\sqrt{gD}}\right)^{-0.383} \quad for\ G_s < G_s^* \quad (14)$$

$$\frac{\varepsilon_{sd}}{\varepsilon'_s} = 1 + 0.103 \left(\frac{U_g^0}{U_s^0}\right)^{1.13} \left(\frac{\rho_s - \rho_g}{\rho_g}\right)^{-0.013} \quad for\ G_s \geq G_s^* \quad (15)$$

ε_s' is the solids holdup when the slip velocity equals U_t:

$$\varepsilon_s' = \frac{G_s}{\rho_s(U_g^0 - U_t)} \tag{16}$$

The saturation carrying capacity is expressed as [24]:

$$\frac{G_s^* d_s}{\mu_g} = 0.125 Fr^{1.85} Ar^{0.63} \left(\frac{\rho_s - \rho_g}{\rho_g}\right)^{-0.44} \tag{17}$$

The Froude (Fr) number is expressed as:

$$Fr = \frac{U_g^0}{\sqrt{gD}} \tag{18}$$

The Archimedes (Ar) number is calculated as:

$$Ar = \frac{d_s^3 \rho_g g(\rho_s - \rho_g)}{\mu_g^2} \tag{19}$$

The particle terminal velocity (U_t) is obtained by calculating the dimensionless terminal velocity (U_t^*) and the dimensionless particle diameter (d_s^*) as follows [25]:

$$U_t^* = \left(\frac{18}{d_s^{*2}} + \frac{2.3348 - 1.7439\,\phi_p}{d_s^{*0.5}}\right)^{-1} \tag{20}$$

$$d_s^* = \left(\frac{3}{4} C_D Re^2\right)^{\frac{1}{3}} = d_s \left(\frac{g\rho_g(\rho_s - \rho_g)}{\mu_g^2}\right)^{\frac{1}{3}} \tag{21}$$

$$U_t = U_t^* \left(\frac{g\mu_g(\rho_s - \rho_g)}{\rho_g^2}\right)^{\frac{1}{3}} \tag{22}$$

ϕ_p is the sphericity of the particles, Re is the Reynolds number:

$$Re = \frac{d_s U_t \rho_g}{\mu_g} \tag{23}$$

C_D is the drag coefficient, expressed as:

$$C_D = \frac{4}{3} \frac{g d_s}{U_t^2} \left(\frac{\rho_s - \rho_g}{\rho_g}\right) \tag{24}$$

*Table 3 The parameters for the dynamic fixed bed reactor (elaborated from [16], *the water adsorption parameter is calculated according to the Langmuir isotherm $b_{H2O} = b_{H2O,0} exp\,(-\frac{\Delta H_{ads}}{RT})$)*

Symbol	**Parameter**	**Value**
ε_b	Bed porosity	0.34
ε_t	Total porosity	0.52
ρ_{cat}	Catalyst density	1450 kg/m^3
φ_{cat}	Catalyst fraction	0.5
ΔH_{ads}	Heat of water adsorption	78 kJ/mol
$b_{H2O,0}$	Langmuir adsorption parameter for water adsorption	1.04×10^{-15}*
ε_{sd}	Solids holdup	

Fluidised and Entrained flow reactor

The fluidised and entrained flow reactor is simulated with a modified two-phase reactor model [26]. The reactor has a diameter of 1.5 m and a length of 2 m. The sorbent has a diameter of 0.0003 m, while the catalyst has a diameter of 0.0015 m. The model consists of the bubble phase and two dense phases: one canonical fluidised phase and one entrained phase. In the canonical fluidised phase, the main reactions take place, while in the entrained phase only the water adsorption occurs. The main assumptions of this model are similar to the previous cases: steady state conditions, plug flow behaviour of the bubble phase, the dense phase is well mixed, interphase and intraparticle diffusion resistances are negligible due to small catalyst particles. The resulting model equation are:

Mass balance on the main components (bubble phase):

$$\frac{dF_{ib}}{dh} = -(K_{bd})_{ib}\left(\frac{F_{ib}}{Q_b} - \frac{F_{id}}{Q_d}\right)A_b \quad (24)$$

The mass balance of water contains an additional term of adsorption on the entrained sorbent particles:

$$\frac{dF_{H2O,b}}{dh} = -(K_{bd})_{ib}\left(\frac{F_{ib}}{Q_b} - \frac{F_{id}}{Q_d}\right)A_b - \varphi_c \varepsilon_{sd} A G_s q_{H2O} \quad (25)$$

The energy balance is:

$$\frac{dT_b}{dh} = \frac{(H_{bd})_b A_b (T_d - T_b) - \varphi_c \varepsilon_{sd} A G_s q_{H2O} \Delta H_{ads}}{\rho_g C_{pg} Q_b} \quad (26)$$

The mass balance of the dense phase is:

$$F_{id} = (F_{id})_F + \int_0^H (K_{bd})_{ib}\left(\frac{F_{ib}}{Q_b} - \frac{F_{id}}{Q_d}\right)A_b dh + V(1-\delta)(1-\varepsilon_{mf})\rho_s \sum_{j=1}^{NR} \gamma_{ij} R_j \quad (27)$$

The energy balance of the dense phase is:

$$\rho_g C_{pg} Q_d (T_F - T_{ref}) - \rho_g C_{pg} Q_d (T_d - T_{ref}) - \int_0^H (H_{bd})_b A_b (T_d - T_b) dh + V(1-\delta)(1-\varepsilon_{mf})\rho_s \sum_{j=1}^{NR} \Delta H_j R_j - U\pi D(Td - T_{sh}) = 0 \quad (28)$$

Comparison parameters

The comparison of the reactors is made according to the following parameters:

CO_2 conversion:

$$X_{CO2} = \frac{F_{CO2}^0 - F_{CO2}^{out}}{F_{CO2}^0} \quad (29)$$

Methane yield:

$$Y_{MeOH} = \frac{F_{MeOH}^{out}}{F_{CO2}^0} \quad (30)$$

CO yield:

$$Y_{CO} = \frac{F_{CO}^{out}}{F_{CO2}^0} \quad (31)$$

Space velocity:

$$GHSV = \frac{F_{tot}\left[\frac{Nm^3}{h}\right]}{V_{react}[m^3]} \quad (32)$$

Table 4 The assumed values for the compounds and for electricity

Item	Price (CHF/kWh)
Biogas	0.06
Biomethane	0.12
Biomethanol	0.20
Electricity (summer)	0.05
Electricity (winter)	0.20
Hydrogen (winter)	0.15

3 Activities and results - Modelling

In the first section, the results of the systemic analysis are presented, while the results of the detailed reactor modelling are shown in the second part.

The procedures and results of experimental part can be found in chapter 4 and 5, respectively.

Systemic analysis

Comparison of biogas valorisation processes

For a better comprehension of the results, the analysed processes are summarized in table 5. These include all the most commonly biogas valorisation processes, both in standard and in flexible operation. The efficiency values of the various process configurations for biogas valorisation analysed are reported in figure 5. The total efficiency is divided in the fractions obtained from the various products (electricity, compressed natural gas and methanol). Additionally, the fraction of the input that is converted into usable heat is shown in the dashed area. CHP has the lowest efficiency (ca. 35 %), because of the relatively low effectiveness of the internal combustion engine used in the biogas valorisation [14]. In fact, an important part of the biogas (more than 40 %) is converted into heat that can be further used in several applications [4]. However, the economic valorisation of this heat is challenging, especially when the heat demand is low (e.g. in summer). The highest efficiency value (ca. 88 %) is found with biogas upgrading. This is due to the low amount of energy required in this process and to the low product losses. Additionally, this process configuration does not produce significant waste heat. The methane production via PtG shows a lower efficiency value (ca. 76 %). In this case, the decrease in efficiency is due to the energy losses in the electrolyser. Note that the result is a combination of the operation hours in CO_2 methanation mode and in upgrading by membrane (i.e. with efficiency similar to the previous case). The combination of biogas methanation and CHP shows an even lower efficiency value (ca. 70 %), because of the low efficiency of the CHP operation. An advantage of this process configuration is the production of heat and electricity only in times of high electricity price, hence following the market demand. For what concerns the methanol production, one can observe that the synthesis via steam reforming is significantly less efficient (ca. 65 % efficiency) than the processes yielding methane. This is due to the large energy losses in the reforming stage, required to produce H_2 from syngas [23]. In this configuration, no waste heat is produced, as the entire process is integrated to efficiently use the heat generated by biogas combustion. The methanol production from CO_2 and renewable H_2 shows higher efficiency with a value of ca. 77 %. Compared to the production via steam reforming, this pathway is more efficient. This is thanks to the higher H_2 production efficiency in the electrolyser than in the reformer unit. The performance of the methanol synthesis is slightly higher than

the methanation process due to the better efficiency of the synthesis reaction (the former is less exothermic than the latter) [24]. As in the methane case, the flexible process coupled with CHP show a lower efficiency (ca 70 %), because of the low efficiency to electricity of this latter operation mode.

Table 5 Summary of the analysed process configurations

Acronym	Process description	Input	Output	Operation hours (h/y)
CHP	Combined heat and power production	Biogas	Electricity	8000
Upg.	Upgrading	Biogas	Biomethane	8000
Meth. + Upg.	Methanation and upgrading	Biogas and electricity	Biomethane	6000 methanation 2000 upgrading
Meth. + CHP	Methanation and CHP	Biogas and electricity	Biomethane and electricity	6000 methanation 2000 CHP
MeOH from SR	Methanol synthesis via biogas steam reforming	Biogas	Methanol	8000
MeOH from H_2 + upg.	Methanol synthesis with upgrading	Biogas and electricity	Methanol and biomethane	6000 methanol 2000 upgrading
MeOH from H_2 + CHP	Methanol synthesis and CHP	Biogas and electricity	Methanol and electricity	6000 methanol 2000 CHP

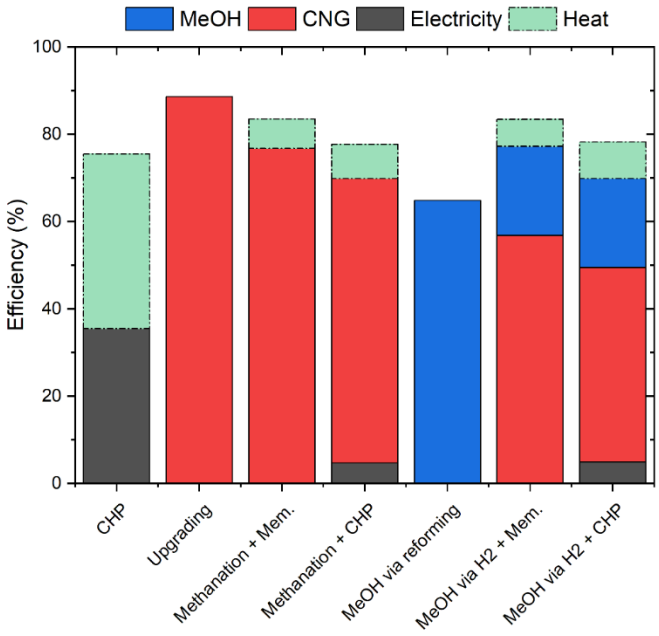

Figure 5 Process efficiency of the analysed biogas valorisation strategies

Figure 6 reports the results of the economic assessment of the various technologies. The results are summarized in terms of the biogas production cost that causes the net present value to equal zero (considering 15 years of plant lifetime and 6% of interest rate). The error bar represents the variation in the product price (the most influential parameter) of ±20 percentage. The dashed line represents a reference biogas price, calculated on the base of the feed-in tariffs for electricity from biogas (0.06 CHF/kWh) [25]. CHP was considered in two different cases: the current conditions, where electricity is supported with a price of 0.20 CHF/kWh all over the year, and the possible future case, where electricity must be sold in the electricity market (i.e. with low price in summer). The biogas cost for the current CHP

is slightly above 0.06 CHF/kWh, confirming the assumptions made on the biogas to electricity process. However, the change in the boundary conditions would cause a significant decrease in the economic performance of the CHP system, causing a drop in the maximum biogas price to ca. 0.025 CHF/kWh. This particularly low value would make it unsustainable to produce electricity from most of the existing biogas plants. This result reflects the trend in act in several countries that are incentivising more efficient and flexible biogas valorisation strategy, causing the decrease in the number of CHP plants installed.

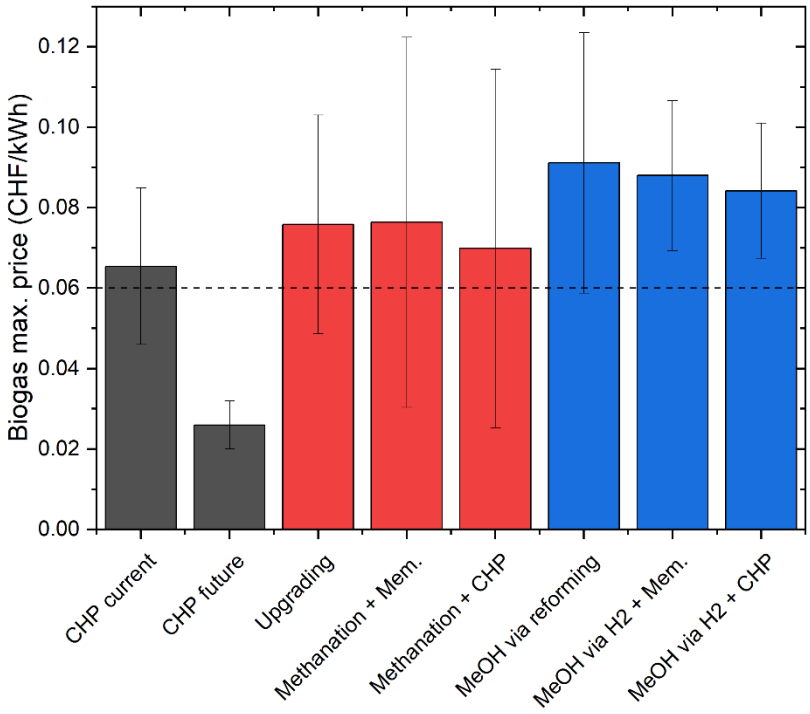

Figure 6 The calculated maximum biogas price for the technologies analysed

The break-even biogas price for biogas upgrading is ca. 0.075 CHF/kWh. This result is in line with what reported in several studies [16,26,27]. This shows the important potential of this technology, which may become the reference process for standard biogas valorisation in the near future. In fact, in addition to a better profitability of this technology compared to CHP, the production of biomethane has a positive influence on the flexibility of the energy system, as the final product does not need to be consumed as the same time as it is first available. However, this flexibility aspect is further enhanced in the coupling of biogas upgrading and CO_2 methanation. In this case, the system would not only have a passive influence on the energy system (avoiding the injection of further electricity when this is already in excess), but it would actively participate into the stabilization of the electricity grid, by consuming electricity when this is available in excess. This view is confirmed by the results of the economic calculations. In fact, the break-even biogas price is slightly higher than in the biogas upgrading case, thanks of this additional energy storage effect. This effect was recognized in several studies in the past [28–30]. However, the extent of this advantage should be confirmed by a detailed analysis of the boundary conditions that make this possible. To this purpose, a sensitivity analysis was performed, as shown in figure 7 and 8. Figure 7 reports the sensitivity analysis results for the variation of the product price. It can be observed that the equivalence point of upgrading and flexible methanation is at 0.118 CHF/kWh of methane value. Additionally, the graph shows that the flexible methanation is more sensitive to the product price than upgrading (larger slope of the curve). This is due to the larger productivity of the flexible process. The sensitivity over the electricity price (figure 8) shows a different

trend, as biogas upgrading requires a limited amount of electrical power for the operation. Therefore, this process is relatively insensitive to the electricity price, while the profitability of the flexible process is strongly dependent on the electricity price. The equivalence point of the two processes lies at 0.051 CHF/kWh. These results show how a slight decrease in the electricity price during the energy storage phase would significantly favour the flexible operation over the standard biogas upgrading. This confirms the hypothesis formulated in literature that the market of the energy storage solutions may increase significantly already in the near future [30].

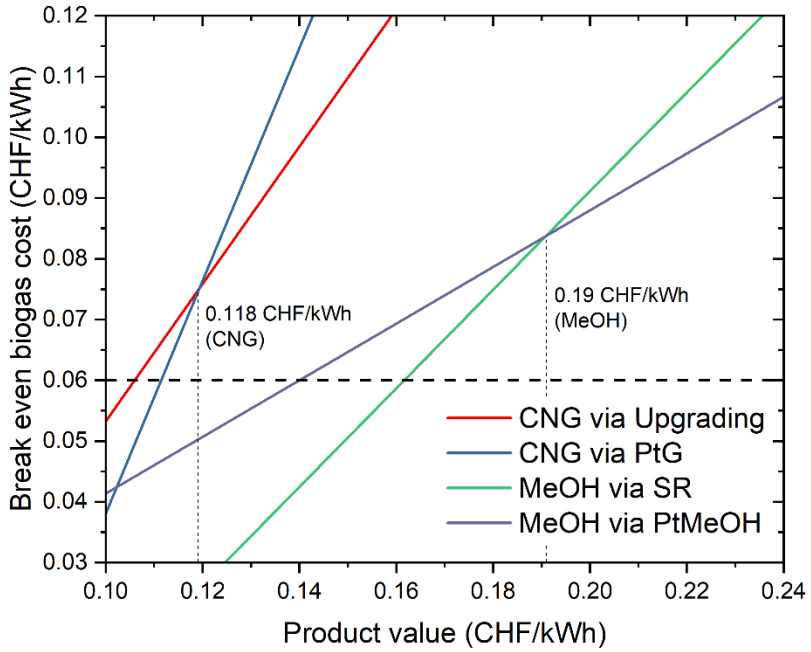

Figure 7 Sensitivity analysis on the product value

The break-even biogas price for methanol production via biogas steam reforming is 0.091 CHF/kWh. This is the highest value found in this study, thanks to the high value of the product and the cheapest way to produce the required H_2. However, as explained above, this solution has also a significant carbon footprint, which makes it less desirable from an environmental point of view. The results of the analysis of this process option are in line with the techno-economic assessment of similar plants available in literature [31–34]. The methanol production via PtMeOH is slightly less profitable than the previous process, due to the higher cost of H_2 from electrolysis. Hence, the break-even biogas price lies at 0.088 CHF/kWh, a significant higher value than the methanol production processes. The assessment of this process configuration yields similar results as the biomethanol production route described by Baena-Moreno et al. [35], despite the different integration of upgrading and methanol synthesis. A deeper comparison of the two methanol production processes is possible thanks to the sensitivity analysis reported in figure 8. The equality point of the two configurations lies at 0.19 CHF/kWh for the methanol value and at 0.046 CHF/kWh for the electricity price. Interestingly, the process via steam reforming is more sensitive to methanol process than the process via PtMeOH. This is due to the important difference in productivity, in favour of the latter configuration. The methanol synthesis via biogas steam reforming is practically insensitive to the change in electricity price, because the electricity requirements in this process are limited. From this analysis, one can conclude that a clear trade-off exists between cheap and green methanol. The profitability of the process decreases significantly with

the decreasing of the CO_2 emissions. This reflects directly the trade-off already present between green and grey H_2 [36].

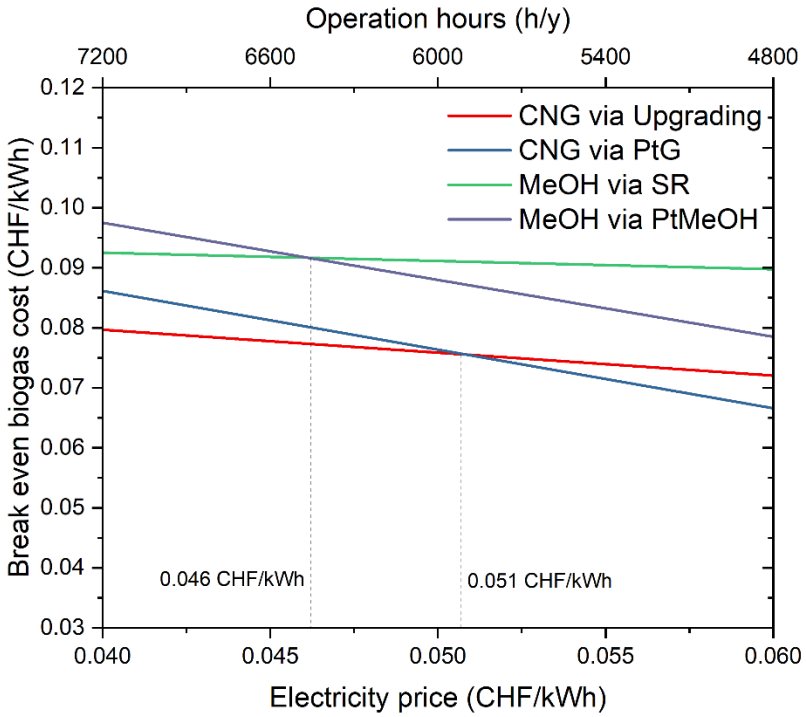

Figure 8 Sensitivity analysis on the electricity price

Systemic analysis: Use of biogas in energy storage

In addition to the evaluation of the direct production of various energy carriers from biogas and power-to-X, it is convenient to analyse the possible use of these carriers in the context of energy storage. This means that the produced CNG and methanol are stored over the seasons to be then used as electricity or H_2 precursors when the availability of renewable energy is scarce. To this purpose, electricity is produced in a gas-fired combined cycle or in a methanol fuel cell, while H_2 is produced by steam reforming. As the results here reported do not include the capital costs related to the electricity production/reforming plant (as this would go beyond the scope of the study), the costs presented here should be considered as the minimum cost the operator of such plants should ponder to purchase the energy carriers when electricity is scarce. Figure 9 shows the electricity/H_2 production cost. The cost of electricity production from CHP and the relative cost of H_2 produced from the same electricity are reported as reference. These are 0.20 and 0.27 CHF/kWh, respectively. For a better discussion of these results, Figure 10 reports the productivity in terms of GWh of electricity or H_2 per year of the various technologies.

Biogas upgrading is the best technology in terms of production cost for both outputs. The production costs are 0.14 CHF/kWh for electricity and 0.11 CHF/kWh for H_2. The cost of electricity is higher than the cost of H_2 for all the energy storage processes because the reforming efficiency is significantly higher than the efficiency of electricity production. The production cost of the flexible configuration upgrading/methanation is 0.18 CHF/kWh for electricity and 0.14 for H_2. These significantly higher costs for the flexible over the standard process reflects the intrinsic cost of energy storage. In particular, this is related to the significant amount of electricity that is used in the production of the synthetic fuel. In fact, the additional amount of product obtained in the energy storage mode (ca. 65 % higher, as visible in figure 10) is sensibly more expensive, hence resulting in a higher total production cost per kWh. The production costs of the flexible process CHP/methanation are slightly higher (0.19 CHF/kWh for electricity and 0.16 CHF/kWh for H2), due to the higher specific cost of CHP over biogas upgrading.

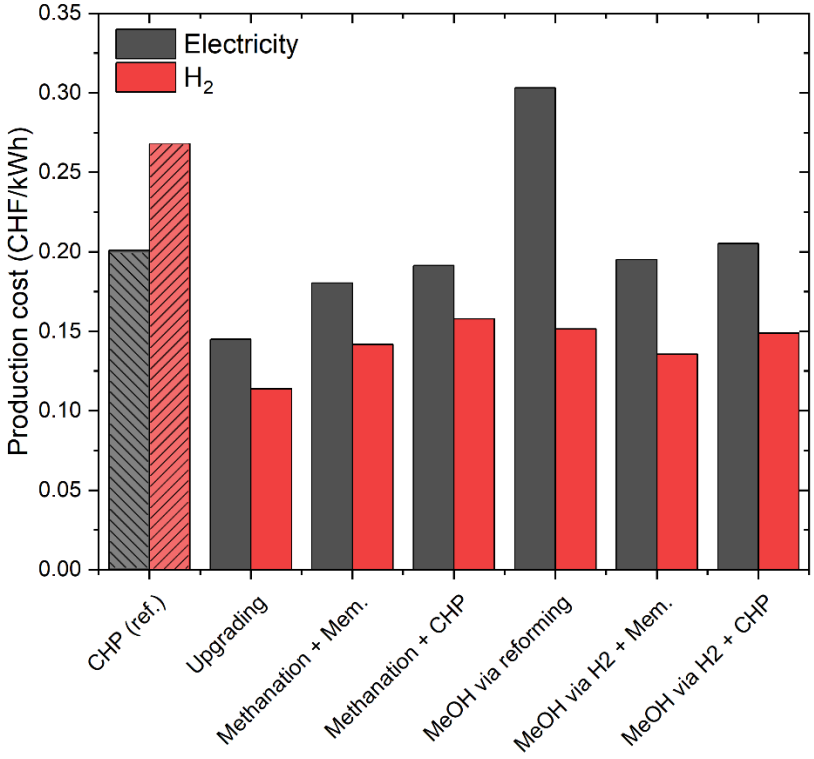

Figure 9 The production cost of electricity and H_2 in the context of energy storage with biogas and power-to-X

The results are significantly different for the methanol case. The cost of production of electricity in the case of standard methanol production from biogas is high (0.21 CHF/kWh). This is due to the low productivity (lower than the CHP case, as visible in figure 12) and to the low efficiency in the methanol to electricity process. The production costs of H_2 are significantly lower (0.15 CHF/kWh), thanks to the efficient methanol steam reforming. The economic performance of the flexible upgrading/methanol synthesis process is superior, with 0.19 CHF/kWh and 0.135 CHF/kWh for electricity and H_2, respectively. The significantly better performance in electricity storage is related to the larger output of the system and to the important share of methane in the products (hence ensuring a better efficiency). The production cost of H_2 is lower than the standard biogas to methanol process, thanks to the better process efficiency (see figure 5), leading to a higher productivity (ca. 78 % higher, as visible in figure 10). Note that the trends are reversed compared to the biomethane case, because H_2 production is necessary for both the standard and the flexible methanol processes. The flexible CHP/methanol

synthesis process is slightly more costly than the flexible biogas upgrading/methanol synthesis route. The production costs in this case are 0.20 CHF/kWh and 0.15 CHF/kWh for electricity and H_2, respectively. As in the biomethane case, these slightly worse results are originated by the lower performance of CHP over biogas upgrading.

To conclude this comparison, one can observe that a clear trend is present in the results: biomethane is a better option for electricity storage, while biomethanol is more suitable for H_2 storage.

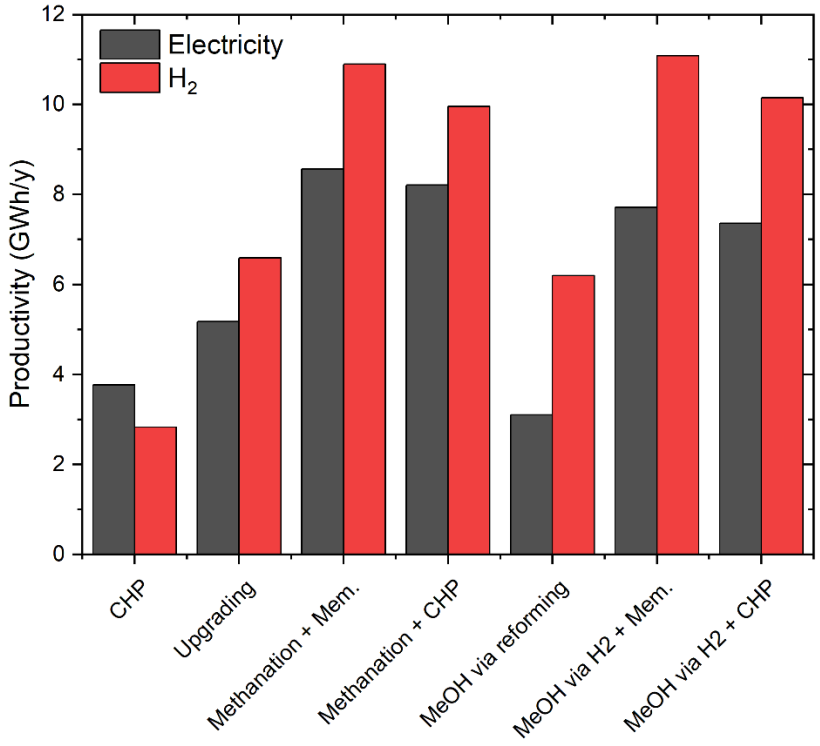

Figure 10 productivity in terms of electricity or H_2 of the selected processes

Assessment of the CO_2 emissions

In order to complete the analysis, the CO_2 emissions of the energy storage processes are calculated. Figure 11 reports the CO_2 emissions of the various technologies in the production of the energy carriers and in their reconversion to electricity or H_2. As a comparison, the reference values of electricity and H_2 (via electrolysis) production from photovoltaics [37] and from the standard EU electricity mix [38] are reported. The results reflect directly the process efficiency (see figure 5). Interestingly, the electricity storage causes a 5-fold increase of the CO_2 emissions (from 45 gCO_2/kWh of the photovoltaics to ca. 250 gCO_2/kWh) for all the configurations used apart from methanol synthesis via reforming. This latter configuration causes emissions for ca. 500 gCO_2/kWh due to the low efficiency. Note that this value is even higher than the emissions originated from CHP. The other processes cause less CO_2 emissions than CHP thanks to the higher energy output and, for energy storage processes, to the input of clean energy. The increase of emissions from the original green H_2 to the final H_2 released in winter is instead lower and limited to 4-fold (from ca. 60 to 250 gCO_2/kWh). The total CO_2 emissions can be further improved if H_2 production is associated with pre-combustion CO_2 capture [39,40].

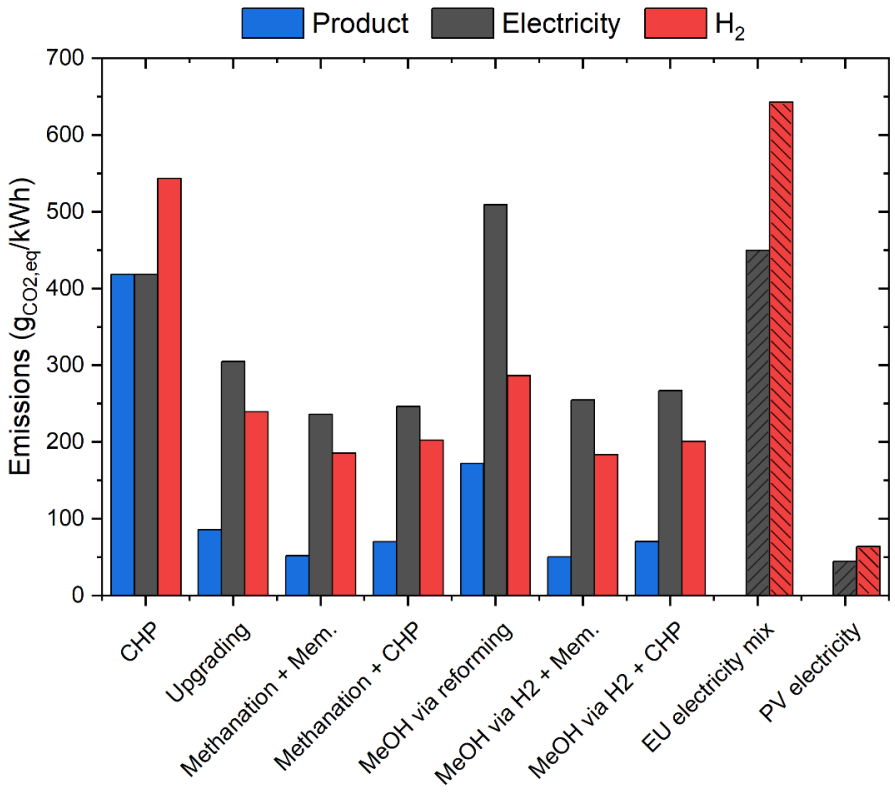

Figure 11 CO_2 emissions for the various technologies analyzed

Benchmarking of the methanol production processes

As the comparison of the biogas valorization processes showed that methanol production may play a role in context of biogas use, it is essential to understand how these processes relate to the state-of-the-art methanol synthesis route. In order to fully understand these last aspects, we compared the cost breakdown for these processes, as shown in figure 12. We included the current costs of a large-scale methanol production plant from biomethane (case Bio LS in the figure) and the target cost indicated by the methanol institute (MI-IRENA in the figure) [41]. The cost of the fuel is the most important part of the plant balance in the state-of-the-art technology. Therefore, the change towards a carbon neutral fuel (i.e. the use of biomethane) already increases significantly the production cost of methanol, from ca. 300 CHF/t of a fossil-based plant to ca. 1000 CHF/t of a renewable gas-based process. Hence, even considering the state-of-the-art technology, the biogas-based methanol production causes an increase in the methanol break-even price. The small-scale methanol synthesis routes proposed in this work comprise an economic performance in the same range of the centralized production, showing that there is a techno-economic potential for this type of processes. This is in part due to the capability of this latter to operate directly from biogas, a cheaper raw material than biomethane. However, this potential can be unlocked only if the transition is supported from decision makers, mainly offering incentives for the production of green methanol. In this sense, in table 5 we provide the values of payback time for the configurations presented in this study. For all the cases, a payback time lower than 8 years is achieved only for a methanol price above 950 CHF/t, which is ca. 2-3 times higher than the current market price of fossil methanol. Therefore, the technological framework for green energy production is already available, but the implementation of the technology is subject to a clear political interest towards the exploitation of carbon-free methanol as a platform molecule for the energy transition.

In order to fully understand the differences between the process studies, it is convenient to refer to the process efficiency (figure 13). Here one can observe that the direct biogas hydrogenation is favoured over the other processes. This is due to the larger production of methane and methanol, thanks to the conservation of the original methane from biogas. The biogas steam reforming process has a low energy efficiency, due to the heat losses in the reforming step. The large-scale process shows a better efficiency thanks to the improved heat integration of the reformer in the process. This difference in efficiency has a direct effect on the CO_2 balance of the processes. In fact, the process based on direct CO_2 hydrogenation offers a better option to avoid CO_2 emissions, as shown in figure 13. The small-scale biogas reforming is particularly penalized on this aspect, because of the significant amount of CO_2 produced in the reforming furnace. This could be improved by installation of a post-combustion CCS unit, which, however, would further decrease the process efficiency. Therefore, we can conclude that the biogas reforming is currently the economically best process for methanol production from biogas, but the lower efficiency and higher CO_2 footprint of this process may penalize its development in future, in case of a different legislation in terms of CO_2 emission and electricity pricing.

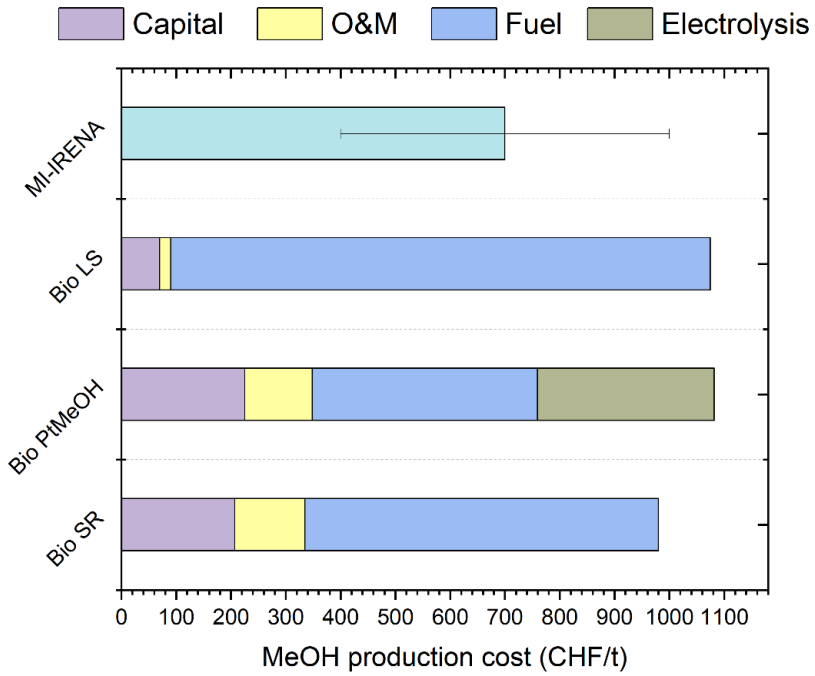

Figure 12 Comparison of the production cost of methanol in various processes. MI-IRENA indicates the reference renewable methanol production according to the study from methanol institute and IRENA. Bio LS indicates the large scale process using biomethane as feedstock. Bio PtMeOH is the process synthesizing methanol from biogenic CO_2 and power-to-methanol. Bio SR indicates the methanol production via biogas steam reforming

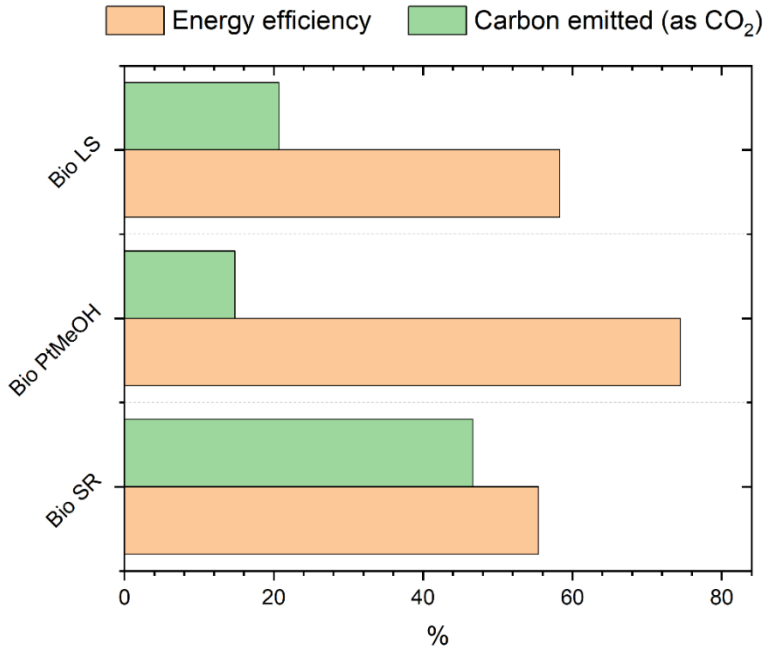

Figure 13 Energy efficiency and carbon emitted in the three different methanol production routes considered

Detailed reactor modelling

The sorption-enhanced reactions are intrinsically discontinuous operations, as water is adsorbed on the surface of the sorbent material until saturation. Once saturated, the material should be regenerated either *in situ* or *ex situ* to remove the water and restore the sorption capacity. The analysed processes, see Figure 4, fixed and entrained flow reactors, differ for the regeneration strategy. In the former case, two identical reactors are operated alternatively in reaction or regeneration. Hence, the regeneration is performed *in situ* and only one reactor at a time is active in the reaction. In the latter case, the regeneration is performed *ex situ* and the spent sorbent is continuously removed from the reactor and replaced by fresh catalyst. In the following, the two strategies are analysed in detail and compared.

Fixed bed reactor

The fixed bed reactor is operated dynamically. Hence, the model used considers the variation of the axial concentration and temperature profile over time. The calculated methanol yield and temperature profiles are shown in figure 14. The results are in good agreement with the experimental results reported in [16]. In the first part of the reactor, the reaction is fast, until reaching a value of approximately 25 % methanol yield. This section corresponds to the reaction hotspot area, as visible from the temperature profile. The calculated position and extension of the hotspot is in line with what experimentally reported for the standard CO_2 to methanol reaction [27]. After this first section, the sorption enhancement effect becomes evident. Initially (50s line), the yield profile increases strongly with the axial coordinate, because the sorbent capacity is high. With the progressive saturation of the sorbent, the profile tends to become flatter, until approximating the standard (non-enhanced) methanol synthesis reaction for a time on stream longer than 150 s. The shift of the water sorption profile is evident in the temperature profile. Initially, most of the water adsorption (exothermic reaction) takes place in the first half of the reactor, so that the heat production in the second half of the reactor is limited. In this way, the cooling is sufficient to reduce the temperature in the second half of the reactor, originating a characteristic hotspot profile. With the proceeding of the reaction, more heat production takes place in the second part of the reactor, as the sorbent in the first part is already saturated. In this way, the heat production is distributed in the

entire reactor, increasing the temperature also in the second half of the reactor. The observed profile is hence the result of two different reaction zones: initially, the heat production is controlled by the (fast) methanol synthesis reaction; when the CO_2 conversion approaches the equilibrium value, the water sorption becomes determining, limiting the conversion to the value allowed by the thermodynamic shift. This suggests that the reactor optimisation depends of the adaptation of the relative ratio of catalyst and sorbent, matching the reaction rate and the thermodynamic shift by water removal. This is particularly important when increasing the pressure. In this case, the reaction yield increases, hence causing an increase in the water production. As the water adsorption is an exothermic reaction, the increase in pressure causes an increase in the outlet temperature, as shown in figure 15. This in turn causes a decrease in the maximum methanol yield reachable, as a higher temperature implies a lower equilibrium yield. Hence, unless the heat transfer is significantly increased, the increase of pressure has a limited effect on the reaction yield. For these reasons, the sorption-enhanced methanol synthesis is particularly suitable for small-scale applications, where low pressure is required due to the economic impact of compression on the process performance [28]. The results elucidated in this section confirm that the sorption enhanced methanol synthesis is feasible in fixed bed reactors, but also showed that the management of the dynamic reactor may be challenging, as the complex interplay of reaction, water adsorption and heat transfer should be controlled with care.

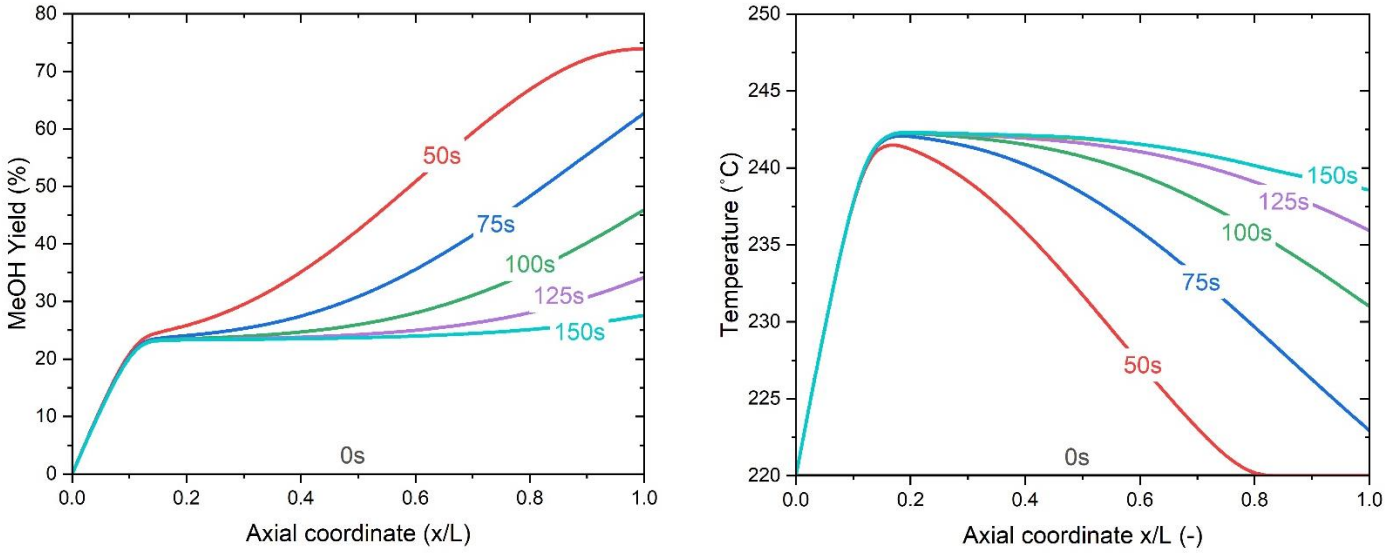

Figure 14. Results of the simulations for the dynamic fixed bed reactor. a) methanol yield profile; b) temperature profile (P = 30 bar, coolant temperature = 220 ˚C, sorbent/catalyst ratio = 1/1)

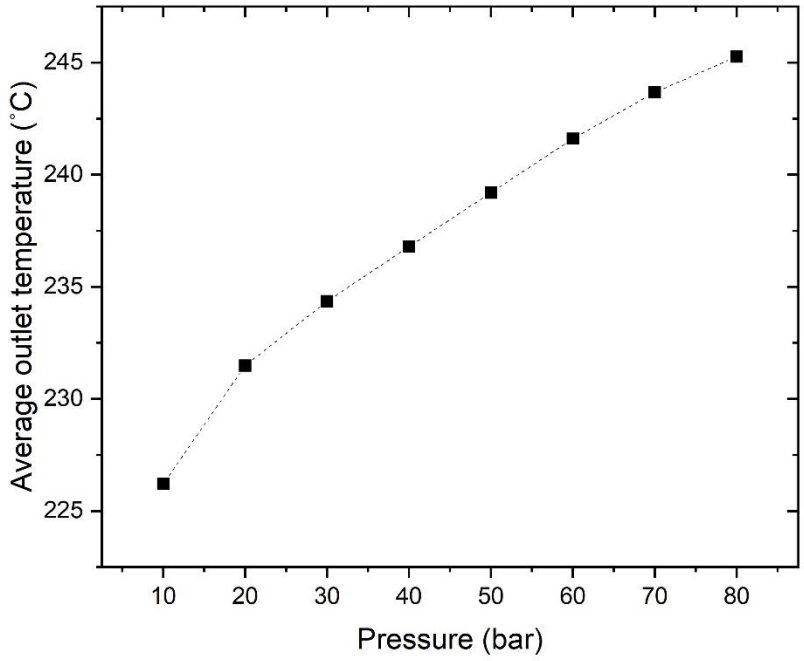

Figure 15 Average outlet temperature in the sorption-enhanced methanol synthesis in the dynamic fixed bed reactor as a function of pressure (coolant temperature = 220 ˚C, sorbent/catalyst ratio = 1/1)

Entrained flow reactor

In the entrained flow reactor, the catalyst and sorbent particles are designed to be entrained by the gas flow. Hence, the residence time of the particles in the reactor is limited and the sorbent does not reach the saturation conditions before leaving the reactor. The sorbent-to-catalyst ratio investigated is 1:1. The results of the simulations for this reactor type are displayed in figure 16. Here, the sorption-enhancement effect is already visible after the first 10 % volume of the reactor. Initially, the water removal increases mainly the extent of the reverse water gas shift reaction, increasing the CO yield. This is well documented by the CO yield curve. After ca. 20 % of the reactor volume, the CO production and consumption start being equilibrated, so that most of the additional CO_2 conversion adds up to the methanol production. In the conditions here investigated, the CO_2 conversion at the reactor outlet is ca. 73 % and the methanol yield is ca. 48 %. The dimensions of the reactor are selected to optimize the space-time yield. An increase of the reactor dimensions could further increase conversion and yield, but the vicinity to the thermodynamic equilibrium would require an excessive volume for a limited increase of reaction yield. The results here presented generally confirm what observed in the existing literature [20]. To summarize the results of the entrained flow reactor, the advantage of the continuous operation is compensated by a low selectivity to methanol. This is mainly due to the short contact time in this reactor type, which results in a significant enhancement of the side RWGS reaction. Additionally, the short contact time results in a low catalyst utilization, as a significant amount of catalyst needs to be continuously fed and withdrawn from the reactor. This results in the requirement of a low apparent GHSV to achieve a significant methanol yield. This drawback can be reduced by changing the catalyst utilization, separating the fluid dynamic properties of catalyst and sorbent.

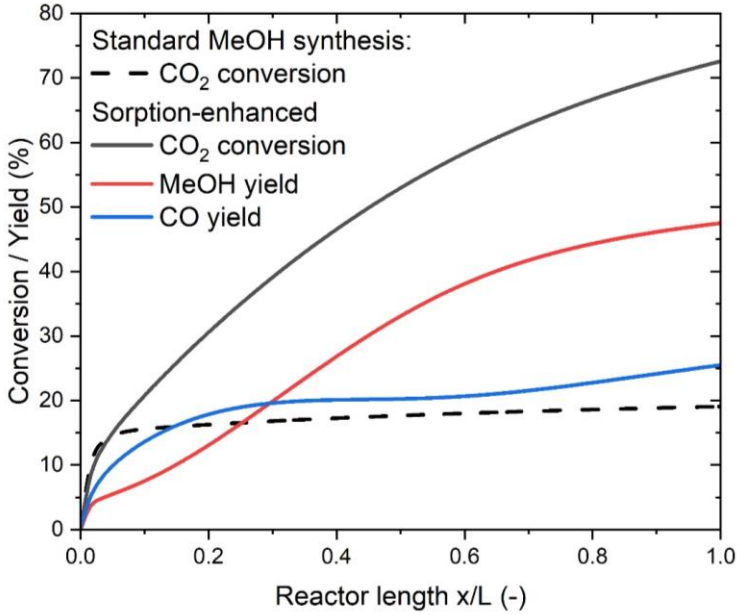

Figure 16. Results of the simulations for the entrained flow reactor, comparing the sorption-enhanced and the standard methanol synthesis (P = 30 bar, coolant temperature = 220 ˚C, sorbent/catalyst ratio = 1/1)

Entrained and fluidised bed reactor

In the entrained and fluidised bed reactor, the flow pattern of catalyst and sorbent is different. The catalyst is sized to constitute the dense phase in the fluidised bed and hence to remain constantly in the reactor. The sorbent is instead of smaller size, so that it is entrained in the gas flow and continuously fed and withdrawn from the reactor together with the gas. In this way, the main drawback of the entrained flow reactor, i.e., the short residence time of the catalyst in the reactor, is overcome. This reactor type was simulated, and the results are reported in figure 17. The CO_2 conversion increases continuously over the axial coordinate, until reaching a value of 70 % at the reactor outlet (the outlet conversion value is determined by the reactor size selected). A slight change in the derivative of the CO_2 conversion curve after approximately 10 % of the reactor volume identifies the change of regime from the preferential production of CO to the sorption-enhancement of the methanol synthesis reaction. This is well visible in the methanol and CO yield curves, as in the first 10 % of the reactor volume the main product is CO, while in the rest of the reactor most of the CO_2 is converted to methanol. The positioning of the CO/methanol crossover point and the shape of the CO yield curve are significantly different from the entrained flow reactor. This is mainly due to the different flow pattern, which modifies the relative concentrations of the components and the extent of the competitive reactions and the positioning of the water sorption over the reactor axial coordinate. Overall, the outlet concentrations of CO, CO_2 and methanol are similar to the entrained flow reactor, but the reactor is significantly smaller, thanks to the lower superficial gas velocity at the reactor inlet.

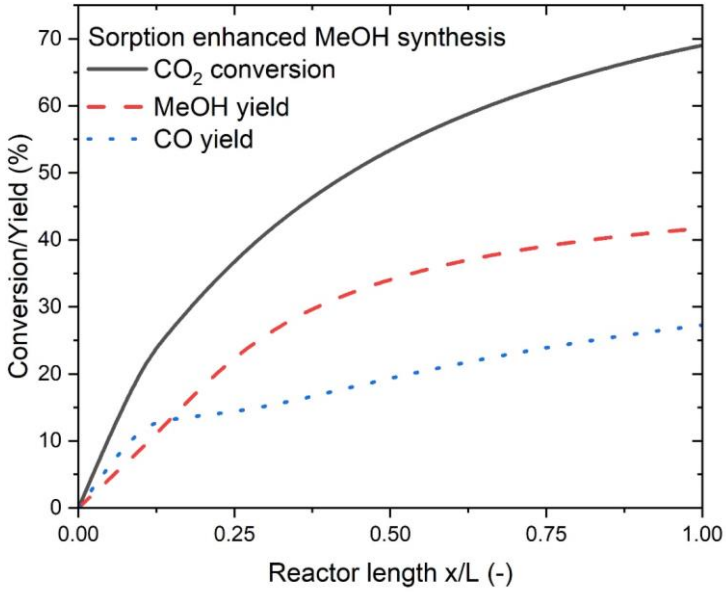

Figure 17. Results of the simulations for the mixed entrained flow/fluidised bed reactor

Comparison of the reactors

The most appropriate way to compare the performance of the reactors is to consider the variation of methanol yield with the space velocity. This allows determining the dimensions required for a reactor to achieve a certain methanol yield, homogenizing the various properties of the three reactors considered. The comparison is shown in figure 18. For the dynamic fixed bed reactor, the calculated space velocity includes the non-reactive residence time due to the sorbent regeneration (e.g., in N_2 flow). One can observe that the fixed bed reactor can reach the highest methanol yield. This is due to the high yield (ideally up to 100%) achieved with a fresh sorbent, at the reaction start. The cumulative yield decreases quickly with the time on stream, due to the progressive saturation of the sorbent. For this reason, it is not convenient to operate this reactor with GHSV higher than 50. A similar trend is observed in the entrained flow reactor. As already observed, high methanol yield is only achieved with a large reactor. In the comparison, it is also evident that the comparison with the dynamic fixed-bed reactor is unfavourable, as the methanol yield at the same GHSV value is lower for the entrained flow reactor. Interestingly, it is also not convenient to operate this reactor at GHSV above 50, because the sorption-enhancement effect is practically absent. This is due to the preferential enhancement of the RWGS reaction in the initial stages of the reaction, making the RWGS reaction dominant for high space velocity. The combined entrained flow/fluidised bed reactor also requires a low space velocity to achieve high methanol yield, due to the preferential methanol synthesis mechanism via RWGS and CO hydrogenation. However, due to the different relative extent of these two reactions, with the continuous increase of CO production over the axial coordinate, the methanol yield tends to remain higher at higher space velocity, compared to the other reactors considered. Hence, this reactor type is suitable to achieve larger methanol yield at high space velocity, resulting in a better possibility to manufacture compact units for the methanol synthesis. The main drawback of this reactor type is the significant amount of CO produced, which results in a lower methanol yield also at low GHSV.

According to this comparison, we can observe that the dynamic fixed bed reactor is suitable for the production of large amounts of methanol in large units, ideally with quick shift between the reaction and regeneration phase. The entrained/fluidised bed reactor can be a good solution for smaller-scale reactors, where high CO_2 conversion can be achieved in compact units. The drawback of low methanol conversion at large space velocity can be overcome by installing consecutive reaction steps (eventually

non-sorption-enhanced) aimed at the conversion of the remaining CO into further methanol. For this reason, a complete comparison of the reactor types should follow the consideration of the reactors in the entire methanol production chain, with the possibility of installing further reactive stages increasing the methanol yield. This optimization problem goes beyond the scope of this study and will be addressed in future research work.

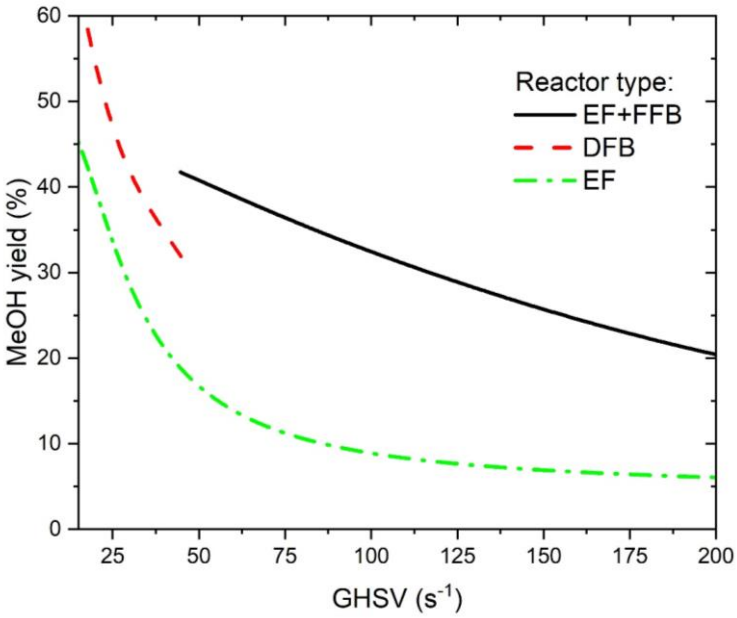

Figure 18. Comparison of the three reactor types. The dynamic fixed-bed reactor (DFB) can achieve high methanol yield (> 50 %), but operates at low apparent GHSV, due to the relatively high amount of gas required in regeneration. The entrained flow reactor (EF) can achieve high yield only at low space velocity, due to the high superficial velocity required to keep the flow regime. The entrained flow and fluidised bed reactor (EF+FFB) can achieve significant methanol yield at higher space velocity.

4 Experimental procedure and methodology

Low TRL experiments (2 to 3) on methanol (MeOH) synthesis involved a bubbling fluidised bed reactor technology (BFB) with a bed-diameter of 21 mm and up to 8 cm bed height (capacity 10 to 25 g), see Figure 19. The core idea of this MeOH synthesis technology is continuous in-situ adsorption of the reaction products by solid sorbents in a BFB reactor applying standard methanol synthesis catalyst (copper-zinc oxide based) as main bed material. The research group already tested this BFB homemade system for the methanation process. A BFB system allows exothermic reactions to occur upon isothermal conditions, thus without the appearance of thermal gradients which are typical of a fixed bed configuration.

The experiments for MeOH synthesis aimed at the selection of the right sorbent material for thermo-dynamic optimization according to the state of the art. The first experiments tested zeolites as sorbent media due to their low acidity. These tests helped to identify the sorbents capability to advance MeOH yield and the rate of desorption when, at first, MeOH and/or H2O flows through the reactor with a carrier gas (either Ar or CO_2). This experimental phase therefore selected a promising sorbent under certain operating conditions (temperatures between 200°C and 300°C, different flow rates) to prepare the tests when CO_2 reacts with stoichiometric H_2 (CO_2:H2 = 1:3) to form MeOH.

In the next stage, the experiments targeted MeOH yield without insertion of sorbent material. The first results allowed a comparison of the reaction yield with experiments including different sorbent materials in a ratio of 1:1 with the catalyst. Different arrangements of fixed beds as well as fluidised bed operation were tested.

As shown in the figures 19 and 20 below, dry (CO_2, H_2) and wet (MeOH, H_2O) compounds are mixed and fed to the vertical reactor from below through a heated line assuring condensation not to occur. The dry gas mixture forms in a mixing line. A second line mixes MeOH and H_2O with, eventually, the dry gasses feeding the reactor system through the heated line. The initial flow of MeOH or H_2O to be tested corresponds to 20% of the total gas mixture volume sent into the system. Preheated air pressure flows along an annular shell surrounding the reactor to assure isothermal conditions.

To reach steady-state conditions (2 barg fixed-pressure and desired temperature from 200 to 300°C) for reliable experiment performance, an initial flux of around 2500 Nml/min composed by reactive gasses and steam flows in a by-pass line connected to the reactor through a 4-pneumatic valves system. At the same time, 2500 Nml/min of N_2 flow by means of the second inlet valve in the reactor as pressure sets to 2 barg. Through the four-valve system, the user can direct the flow of reactive gasses from the by-pass to the reactor path. A pressure regulator placed on the exhausted gasses line keeps the pressure steady inside the reactor.

Prior starting the experiments, 400 Nml/min of H_2 diluted in 400 Nml/min of Ar as inert gas flow over the reactor bed for about 10 minutes at atmospheric pressure and target temperature to activate the catalyst. This way, reduced metal species – thus the active sites for reaction – boost CO_2 conversion rate. During the reaction, catalyst and sorbent “float” upon a fluidisation speed of about 2900 Nml/min (fluidisation number u/u_{mf} = 3-5). Different from the actual test reactor, in up-scaled reactors, the catalyst can remain suspended in the reactor (fluidised phase), while the sorbent always flows with the gas in and out of system.

A high fluidisation speed is necessary to distribute the energy released by the exothermic reaction along the whole bed height. Several thermocouples provide temperature profiles along the reactor. The system can register up to four temperatures over time. As soon as the exothermic reaction takes place, the air pressure system cools down the reactor body to a constant jacket temperature controlled by the thermocouples. Other thermocouples monitor the thermodynamic conditions relevant for CO_2 conversion on the heating lines upstream and downstream the reactor. The reaction heat dissipates outside at the higher part of the bed. A few centimetres above the gas distributor, two thermocouples measure the temperature over the reactor radius to check for temperature gradients along the diameter.

The connection of a micro Gas Chromatography or µGC (CP-4900) either at the by-pass (non-reacted gasses) or at the outlet reactor line (reacted gasses) allows for gas composition measurements, thus MeOH yield, for each sorbent material. On the same streamline, a Mass Spectrometry or MS device (Pfeiffer Vacuum) detects mass-to-charge ratios.

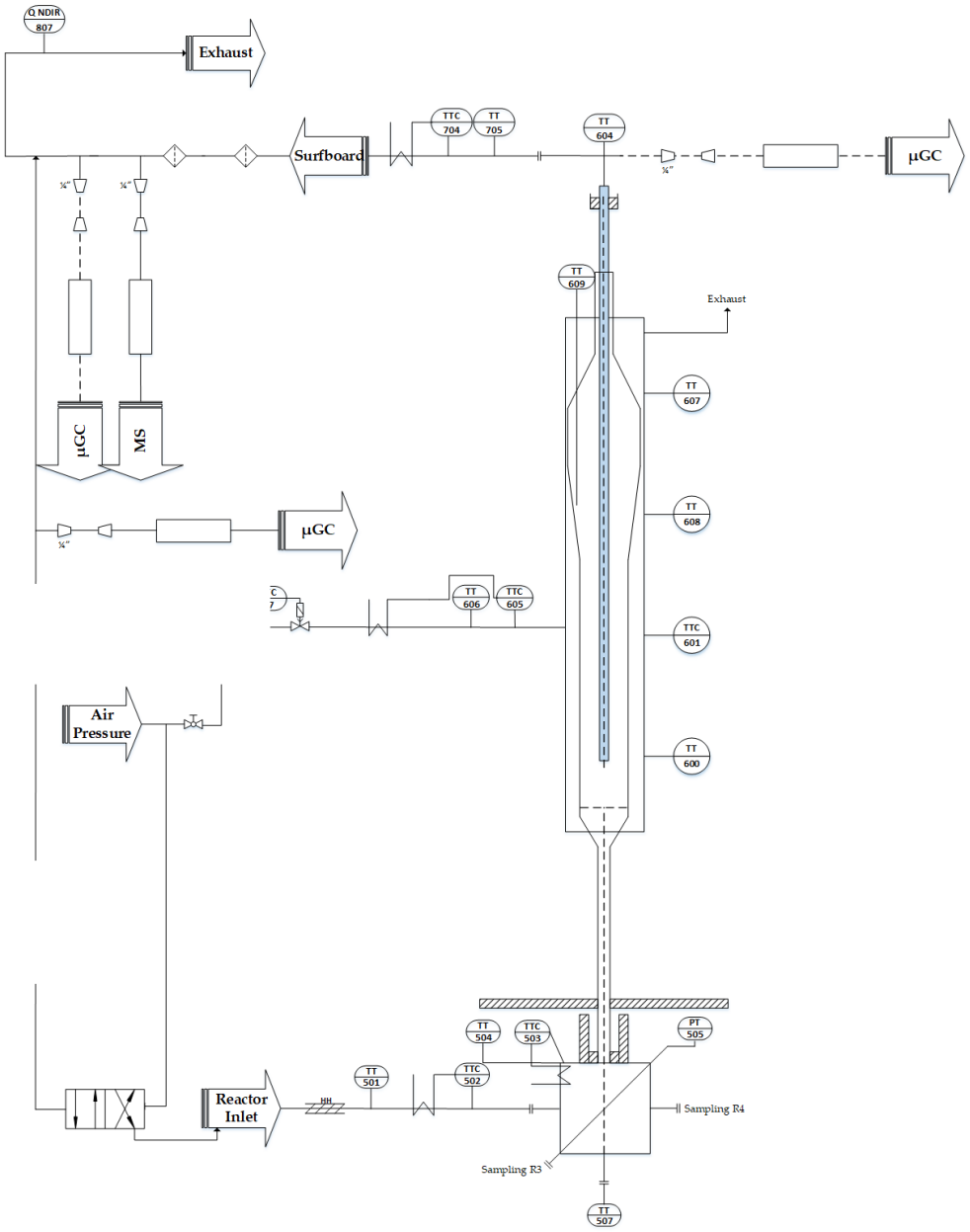

Figure 19 Scheme of the TRL 2-3 set-up

Figure 20 Photographs of the TRL 2-3 set-up

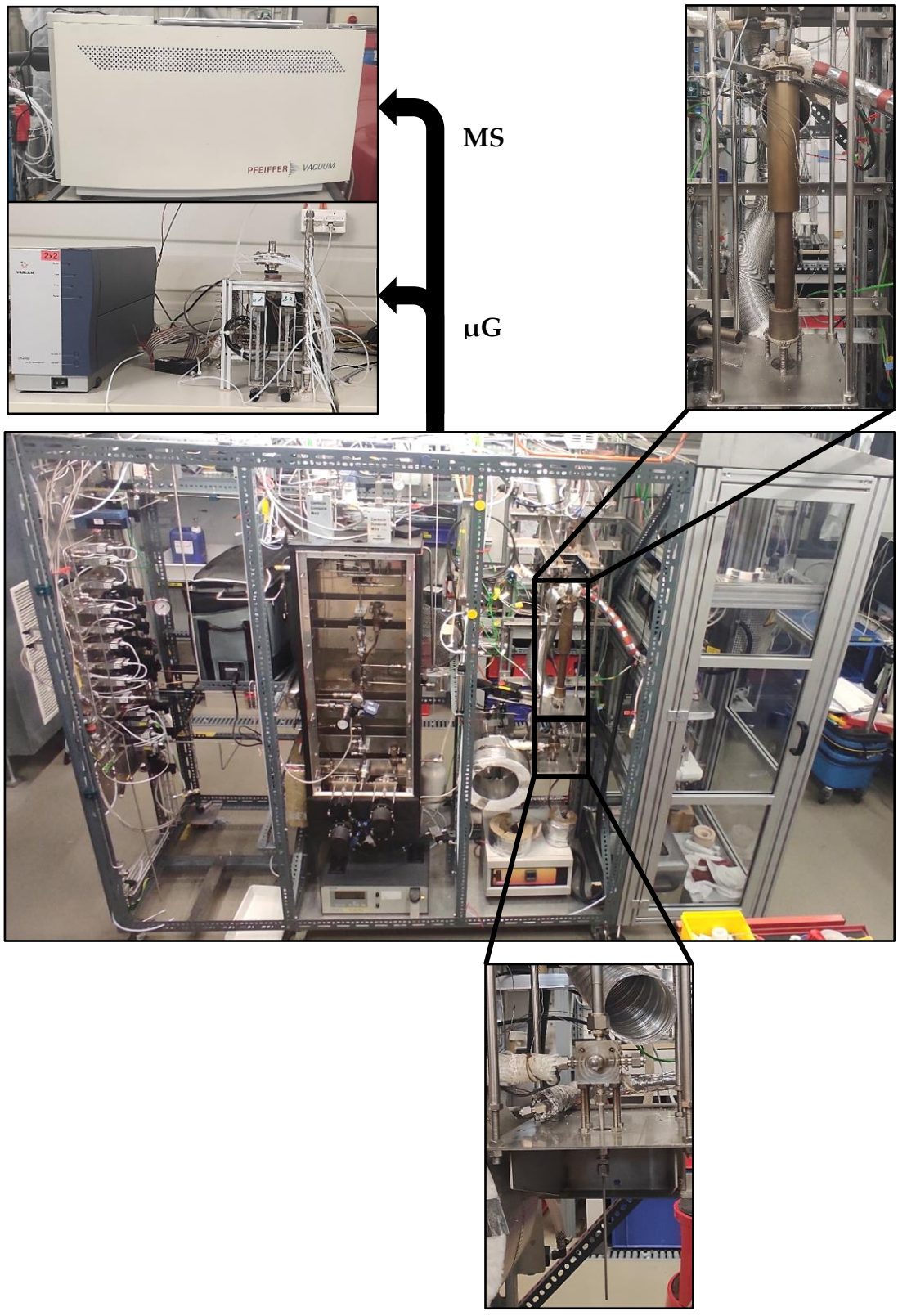

5 Experimental results

Review on potential sorbents

Sorption-enhancement is a well-known technique, which was applied to several reactions, including steam reforming [42], CO_2 methanation [43], water-gas-shift reaction [44] and dimethyl-ether production [45]. Sorption-enhanced methanol synthesis in fixed bed reactors was demonstrated in some recent studies using Cu-based catalysts mixed with zeolites, which act as water sorbents [46,47]. The water adsorption has a double promoting effect on the methanol synthesis. On one hand, the in-situ water removal shifts the thermodynamic equilibrium, hence causing an increase in the reaction yield [48]. On the other hand, the water removal prevents the inhibition of catalyst active sites due to competitive adsorption [49].

Several studies showed that Zeolites 3Å and 5Å are ideal for applications in the methanol synthesis [18,19]. Other studies evaluated Zeolites 4Å [50, 51], Zeolites 13X and dealuminated Y Zeolite (DAY) [52]. Kim et al. [53] evaluated the adsorption isotherm of water vapour on three different types of zeolite pellets; 3A, 13X and DAY. Properties of these Zeolites are listed in the Table 6. According to this study, Zeolite 13X adsorbed the highest amount of water at the evaluated temperatures (293, 303 and 313 K), followed by zeolite 3A and then DAY. The trend in isosteric heats of adsorption was zeolite 3A > zeolite 13X > DAY. For all the zeolites, the decrease in the isosteric heat was observed with increasing adsorbed amount. High adsorption affinity of water on zeolite 3A and 13X was observed in the low pressure range.

Table 6. Physical properties of zeolite pellets; 3A, 13X and DAY.

Property	Zeolite 13X	Zeolite 3X	DAY
Type	bead	pellet	pellet
Bulk density, kg.m^{-3}	640	660	500
BET surface area, m^2/g	743		704
Micropore volume, cm^3/g	0.3964		0.268
Micropore size, Å	8-9	3	7.4
Particle size, mm	2.1	3.7	2
Pore diameter	1.79		2.17
Total porosity	0.2923	0.4219	0.4342

Terreni et al. [46] evaluated the production of methanol from syngas using sorption-enhanced catalysis in a fixed bed reactor. Zeolite 13X was shown to be the appropriate zeolite compound for the adsorption of water. However, some amount of the product was adsorbed by the zeolite, which is a drawback. This work also showed that the selectivity could be influenced by varying the temperature. In a recent study by the same group [52], the reaction mechanism of methanol synthesis over Cu impregnated 13X zeolite is evaluated. According to this study, the formed water is initially removed from the reactive sites to the zeolite, until it is saturated. Thus, the water partial pressure differs over the course of the reaction influencing the individual reaction steps. It was found that methanol and dimethyl ether was formed relatively late without significant water formation indicating that a substantial number of intermediates (CO, methoxy, and methyl groups) is formed at early stages, accumulating in the sorption catalyst before finally reacting to the end product.

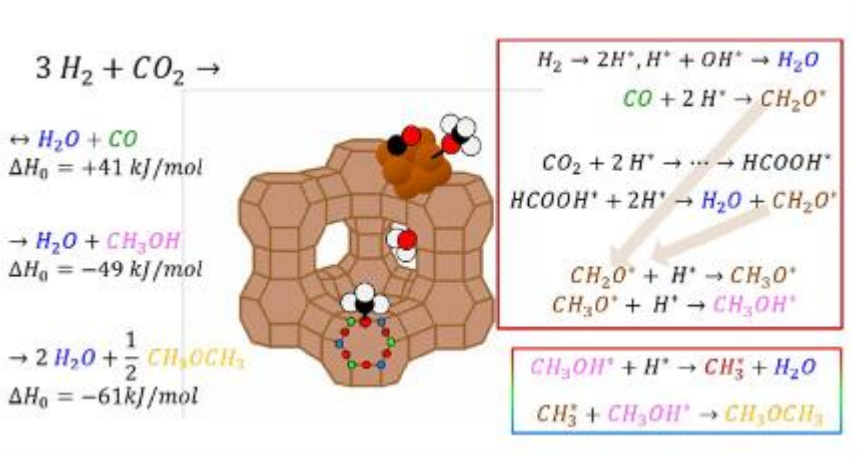

Figure 21. The overall reaction of methanol formation over copper-impregnated zeolite is shown in the left side and on the right side, the potential intermediates are shown [52]*.*

Bayat et al, [50,51] evaluated the use of zeolite 4Å with a mathematical model. Zeolite 4A crystals/membranes are suitable for the separation of polar from non-polar molecules due to their high hydrophilicity. The zeolite 4A, consists of 12 SiO_{2}- and 12 AlO_{2}- units, enclosing a large cavity (α-cage) and a small cavity (β-cage). The negative charge introduced by each aluminium atom in the framework is counter-balanced by a sodium ion. When fully hydrated, there are 27 water molecules in the pseudo unit cell having the composition $Na_{12}(Si_{12}Al1_{2}O_{48})\cdot 27H_{2}O$. The maximum water adsorption capacity of the dehydrated zeolite-4A is 28.51 wt.% or 15.84 mol/kg. Thus, the dynamic simulation result reveals that simultaneous application of water adsorbent and hydrogen permeation in methanol synthesis process contributes to a significant enhancement in methanol production.

Experimental plan, conditions, and selected materials

We divided the experimental effort into two campaigns:

- TRL 2-3 campaign, aiming at a preliminary proof of the new reactor concept by investigation on a lab scale at the low constant relative pressure of 2 barg. The purpose of this campaign was to validate the feasibility of the new reactor concept in a controlled environment and to identify any potential challenges or areas for improvement at an early stage of development. This campaign further identified three sets of experiments:
  (A) Water and methanol adsorption on three sorbents,
  (B) Methanol synthesis without product adsorption,
  (C) Methanol synthesis with product adsorption.

- Parallel lab-scale fluidisation of dense sand and lighter, smaller aluminum oxide particles simulating, respectively, catalyst and sorbent particles in a transparent test tube, which allowed us to observe the fluidisation process and identify particle separation in real-time.

The low TRL campaign considered both fixed and fluidised bed conditions for SE experiments. Results are compared with the current state of the art, mainly focused on fixed-bed reactor types despite the appearance of axial thermal gradients. In the MiWi facility, reactions occurred over a bed volume of 41 ml when particles were fluidised. In fixed-bed configurations, 6 cm, thus 40% of the total available length, was considered for both sorbent and catalyst beds, mixed in a ratio of 1:1. Temperature, initial gas composition, bed configuration, and space velocity were the critical parameters investigated. The reactor temperature was kept between 200 and 300°C, corresponding to the range of activity of the

catalyst for methanol synthesis. For all experiments, desorption was performed by sending 1 L/min of inert gas to the reactor and imposing a jacket (wall) temperature of 350°C.

Commercial $Cu/ZnO/Al_2O_3$ catalyst (KATALCO 51-102 from Jonson Matthey) was characterised for standard and SE methanol synthesis.

For the water adsorption experiments, three different materials were tested based on the results from the literature screening. Molecular sieve type 3X was chosen for its high adsorption affinity to water, while molecular sieve type 4X was selected to verify methanol co-adsorption due to its larger pore size (4Å) and potential subsequent production of dimethyl ether (DME) over the acidic sites of the zeolite's surface.

Due to the hydrophobicity of DAY when compared to zeolites 3X and 13X, a non-type Y molecular sieve with typically smaller pore channels was chosen to monitor CO_2 and methanol co-adsorption. The selected sorbent was sodium mordenite (MOR), which was chosen for its measured pore size of 10Å and a surface area of 631 m^2/g with BET analysis, making it suitable for the experiment.

Methods, results, and discussion

(A) Water and methanol adsorption experiments

The adsorption experiments, thus the MS measurements, were divided into two phases:

Pre-experimental phase

To detect complete adsorption of water and/or methanol, the two are first carried by feed dry gas in the by-pass line at which outlet we connected the mass spectrometer with a manual valve. This way, the MS measures the reference level of signals in the by-pass where adsorption does not occur (Figure 22). Meanwhile, inert gas flows in the reactor to dry the sorbent from moisture and prepare for the experiment. The connection is then switched to the reactor outlet to register the minimum signal of water and/or methanol when only inert gas flows in the reactor (Figure 23). This signal is used as a reference to detect complete desorption.

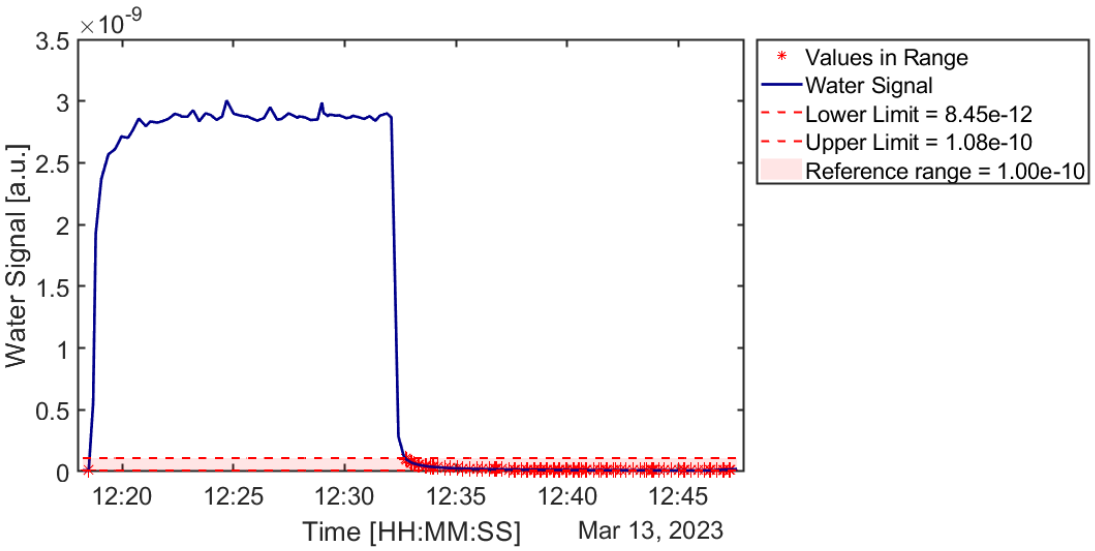

Figure 22 Measurement of water signal at the by-pass outlet via Mass Spectrometry (model GSD 301 O1 by Pfeiffer Vacuum, D-35614 Asslar). Its level, measured prior to each experiment, is used as a reference for complete adsorption.

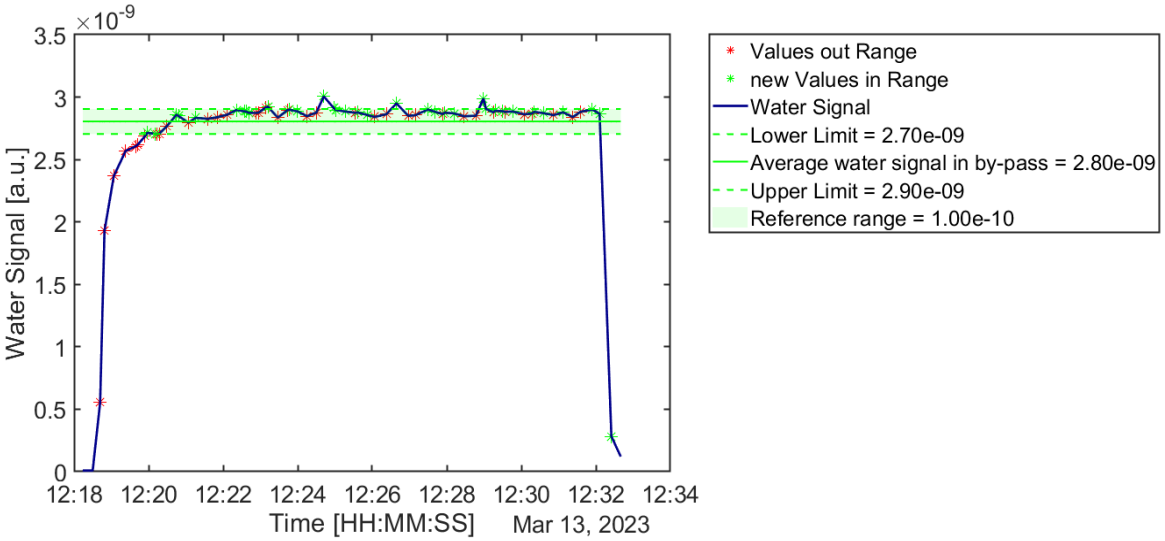

Figure 23 Measurement of water signal at the reactor outlet from 12:32:40 h via Mass Spectrometry when only inert gas flows through the sorbent. The MS detects then the minimum level of water signal, used as a reference for complete desorption.

Experimental phase

When the MS is connected at the reactor outlet, the gas mixture is diverted from the bypass to the reactor to measure adsorption through variations in the signal. During adsorption, the air cools the reactor to a stable jacket temperature, which differs from the internal temperature profile of the reactor. For the adsorption experiments, two inner thermocouples were used to detect a temperature peak characteristic of the adsorption process, as the material releases heat until local saturation is reached. Through these measurements, the initial adsorption time was determined, after which the signal of the adsorbed species remains stable until a breakthrough curve identifies local saturation. Once the material's adsorption capacity is exhausted, the temperature decreases accordingly (Figure 24). Finally, the adsorption time is corrected by matching the signal to the reference range measured at the bypass outlet. The breakthrough curve is then rescaled to the water flow rate (in grams per hour) measured at the MFC and integrated to calculate the water uptake (Figure 25).

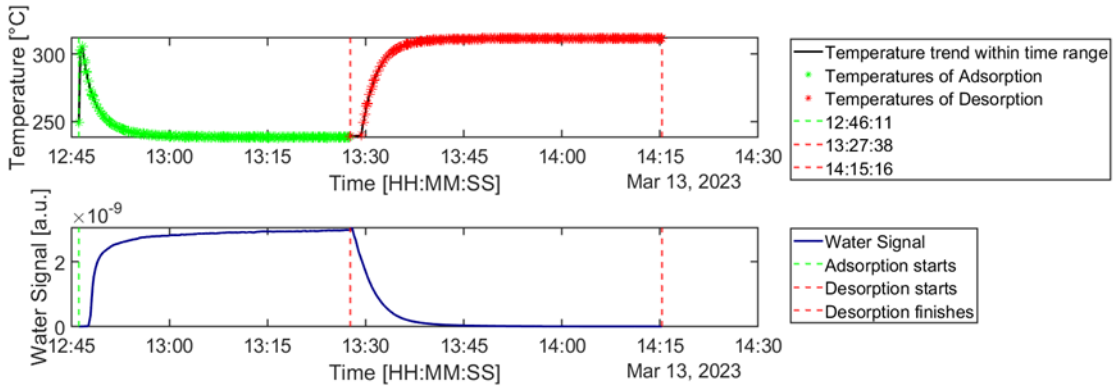

Figure 24 Upper graph: Temperature trend during adsorption (green values) and desorption (red values) for which reactor temperature is set to 310°C. Adsorption is detected with a peak in temperature that stabilizes to a near jacket temperature when the adsorption capacity of the sorbent is exhausted. Lower graph: variations in the water signal during adsorption and desorption.

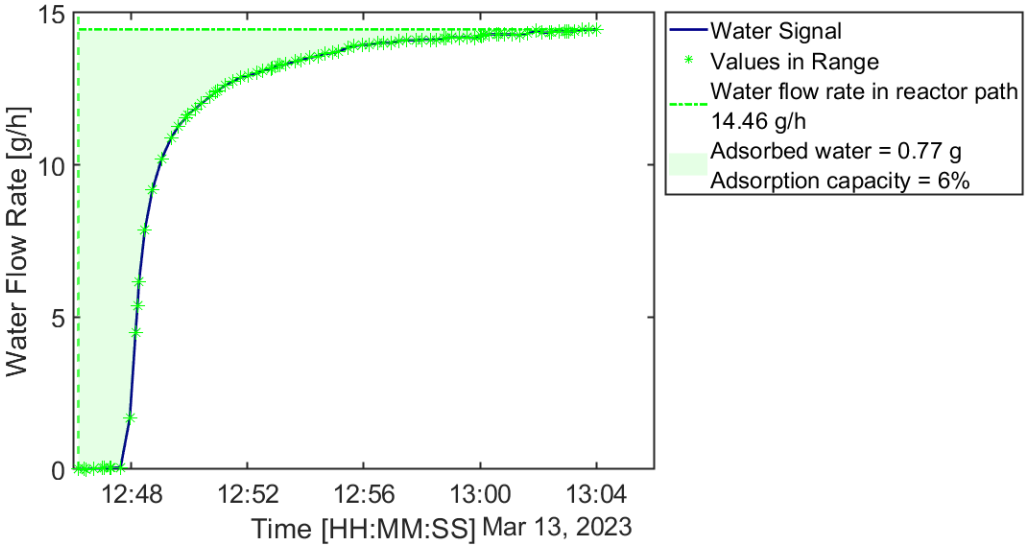

Figure 25 Integration of water signal over adsorption time to calculate grams of adsorbed water, which divided by the grams of sorbent determine its adsorption capacity.

Impact of gas space velocity on water adsorption capacity:

With the above-explained procedure, the water adsorption capacity of MOR was measured to be 5 ± 1% at 250°C, space velocity of 4.5 L/h/$g_{sorbent}$, and water partial pressure of 0.6 bar in inert gas. As shown in Figure 5, the effect of space velocity variations on the adsorption capacity is negligible. Following the established trend of CO_2 conversion concerning gas velocity in hydrogenation processes, this enables the selection of a lower space velocity for the sorption-enhanced methanol reactor, leading to improved conversion in a smaller reactor volume [54].

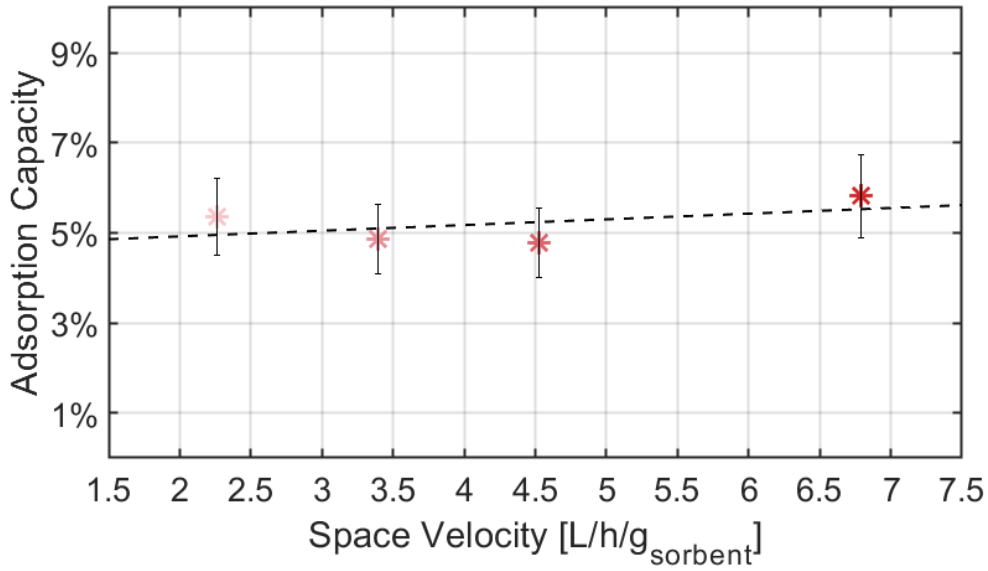

Figure 26 Adsorption capacity of MOR versus space velocities of 2.3 - 6.8 L/h/$g_{sorbent}$. An average random error of 1% is estimated from a preliminary sensitivity analysis.

Impact of temperature on water adsorption capacity:

Following these results, the next breakthrough experiments focused on investigating variations in the water adsorption capacity with temperature. Results are summarized in Figure 27 for MOR and 4A, showing a sharp decrease in the adsorption capacity of both zeolites when temperature increases above 250°C.

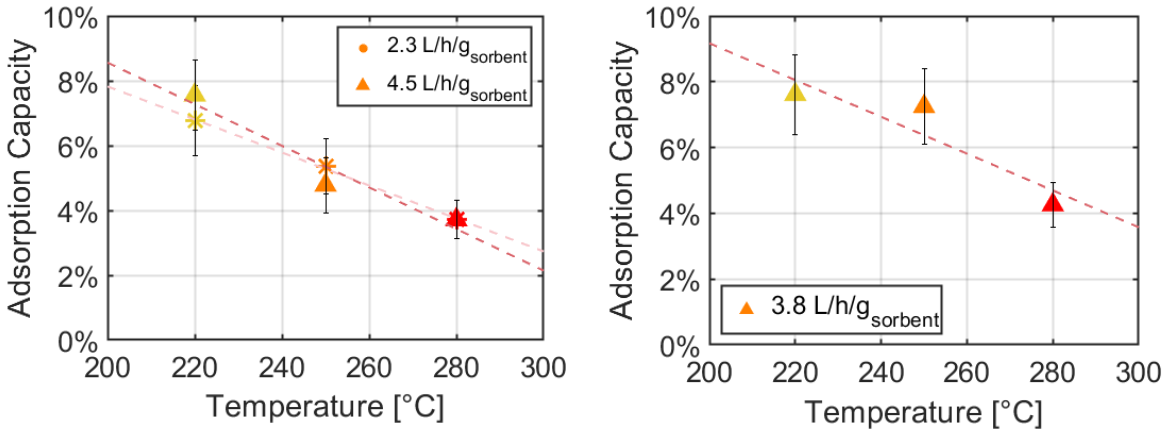

Figure 27 Variation of water adsorption capacity of MOR with temperature for two different space velocities (left), for molecular sieve 4A at the space velocity of 3.8 L/h/$g_{sorbent}$ (right).

These findings align with recent experimental studies that investigated the effect of varying reactor temperatures within the 210–270°C range. The studies highlighted that higher temperatures lead to less favorable adsorption during sorption-enhanced methanol synthesis [54], [55]. As a result, reduced water uptake limits the duration of the sorption enhancement, diminishing its overall effectiveness.
Consequently, the researchers recommended operating a fixed bed methanol reactor before the water breakthrough occurs, emphasizing the importance of determining the adsorption time prior to saturation. Additionally, since CO/CO_2 hydrogenation reactions reach thermodynamic equilibrium at around 250°C in both standard and sorption-enhanced processes, the studies advised an operational temperature window of 210–240°C, with the highest methanol production rate anticipated between 230°C and 250°C. In our reactor concept, the limitation over the operating time prior to saturation is overcome with continuous regeneration of the sorbent bed. However, determining the effect of temperature over adsorption close to the thermodynamic value for methanol synthesis is an essential step of reactor design. Specifically, Figure 27 displays a negligible effect in the water adsorption capacity of zeolite 4A in the 220-250°C temperature range, in accordance with previous studies on 4A crystals [56].

Variations of 3A's adsorption capacity with temperature are not reported here due to experiment outliers caused by the high isosteric heat of adsorption. However, extensive literature is available on molecular sieve 3A, being the most studied zeolite for its highly selective water adsorption. Figure 28 reports the results of Kampen et al. [57] concerning the variation of 3A's water adsorption capacity with temperature. A sharp decrease, as observed with MOR, is visible in the 220-280°C temperature range.

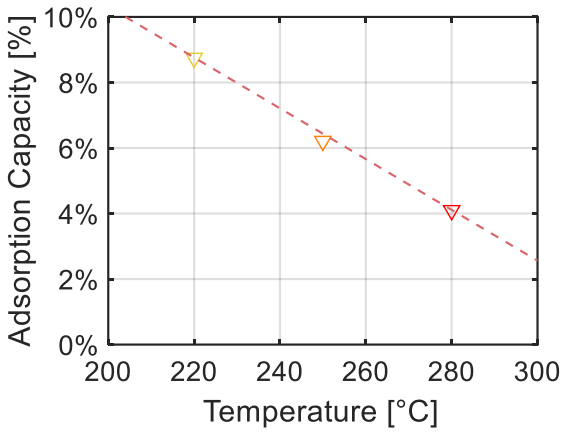

Figure 28 Variation of water adsorption capacity of 3A with temperature according to the breakthrough experiments and fitting of y condensation model performed by Kampen et. al [57].

Impact of feed gas mixture on water adsorption capacity:

The next key findings include the selectivity of the tested sorbents for water adsorption with varying gas mixtures at 250°C. The graph in Figure 8 shows how water uptake shifts when methanol is added to the vapor and inert gas feed (light magenta bars). For both experiments, the partial pressure of water was kept at 0.6 bar. As for the literature's results, the molecular sieve 3A maintains high water selectivity without methanol co-adsorption, resulting in a consistent water uptake of about 5% [57]. Additionally, no methanol breakthrough was observed.
On the contrary, the water adsorption capacity of molecular sieve 4A drastically decreased in the presence of methanol, as observable in Figure 29.
Compared to single water adsorption, this reduction is 13% for MOR and 29% for 4A. This aligns with previous studies that highlighted the co-adsorption of methanol and DME on 4A [58]. Later experimental investigations on the effect of methanol on the water adsorption capacity of pelletized 4A reported a 25% loss after a single adsorption cycle in the presence of methanol, confirming MiWi results. Additionally, a further capacity reduction of up to 70% was observed after just three adsorption cycles [59].

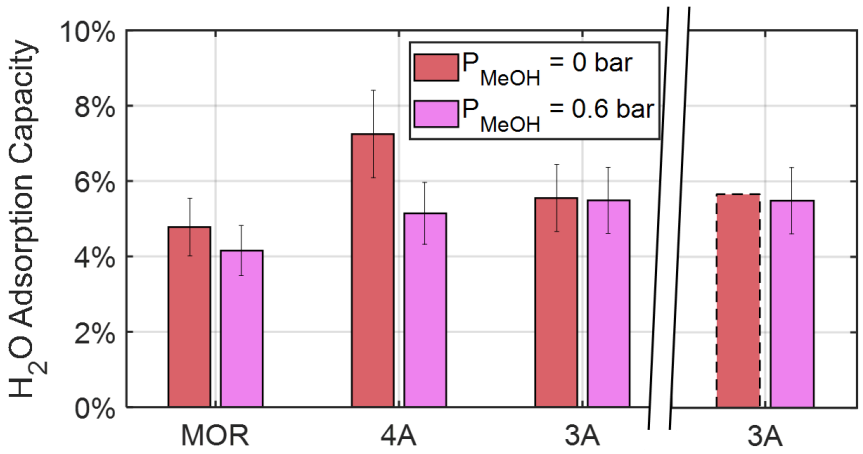

Figure 29 Water adsorption capacity of MOR, 4A, and 3A in the absence and presence of methanol in the gas feed with the same partial pressure of water (0.6 bar), reducing the amount of tracer inert gas. The adsorption capacity of molecular sieve 3A compared with literature studies [57].

Finally, the co-adsorption of methanol with water resulted in a higher methanol uptake over molecular sieves MOR and 4A, reaching 7 and 9% of methanol adsorption capacity, respectively. This outcome was verified with a final set of experiments quantifying the methanol adsorption capacity of MOR and 4A without the presence of water. The partial pressure of methanol was kept at 0.6 bar. The two zeolites exhibited a single methanol adsorption capacity of 10 and 13%, corresponding to twice that of water adsorption.

As shown in Figure 30, the formation of DME occurred for all three investigated zeolites at 250°C during competitive adsorption of methanol and water. Type 4A led to greater production of DME, followed by MOR and 3A, which showed the lowest DME formation. The results presented in this section are congruent with the higher selectivity for water exhibited by zeolites 3A and 4A due to their small pore sizes of 3 and 4Å, excluding larger molecules from the adsorption process and subsequent dehydration of methanol to DME on the zeolite's acidic sites [57], [58]. This concept is highlighted in the right graph of Figure 30, reporting the kinetic diameter of the adsorbed molecules.

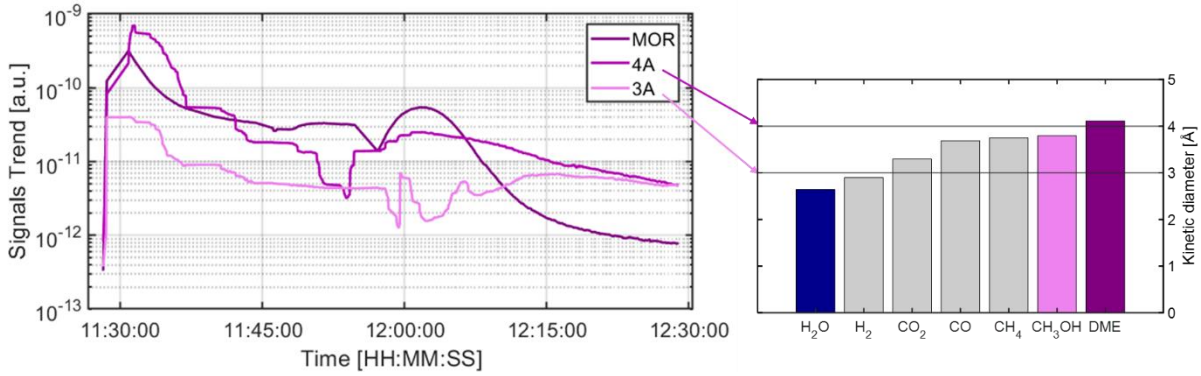

Figure 30 Trend of DME signal at the mass spectrometer (left graph) after the breakthrough of methanol and water for zeolites type 4A, MOR, and 3A. The initial peak indicates DME formation by dehydration of methanol. The amount of formed DME is in accordance with the selectivity of water and methanol adsorption based on the kinetic diameters of the molecules (right graph) with respect to the zeolites' mesopores. The kinetic diameters have been extrapolated from J. Van Kampen et al. (2021) [4].

The phenomenon leading to DME production is better explained in Figure 31. In the lower graph, the DME signal (represented in purple and amplified by a factor of 10) shows a peak following both water (blue) and methanol (magenta) breakthrough, indicating that DME formation occurs during the adsorption phase. This supports the idea of methanol dehydration to form DME on the acidic sites of the zeolite (MOR), facilitated by the removal of water as it gets adsorbed. The co-adsorption of DME along with methanol and water is evident from the concurrent breakthrough times seen in the mass spectrometer signals. This behavior suggests that DME formation halts once the acidic sites on the zeolite are fully blocked, with a subsequent decrease in the signal.

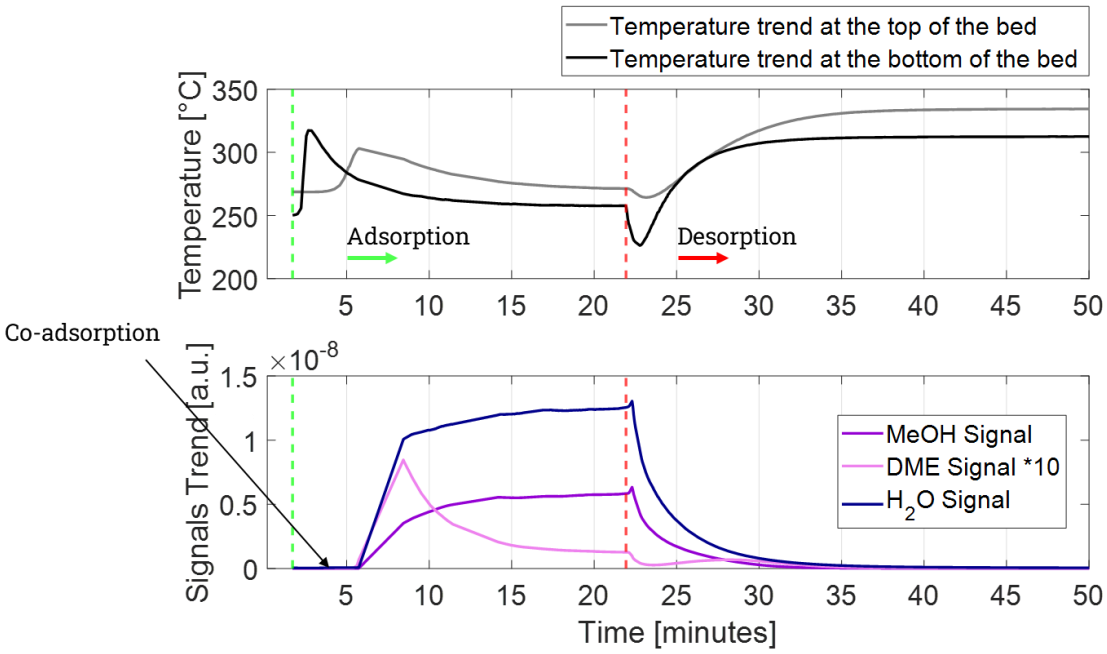

Figure 31 Upper graph: temperature variations measured by the thermocouples TT-609 and TT-604 at the bottom and top of the sorbent bed, respectively. Lower graph: breakthrough curves of methanol, water, and DME during adsorption experiment for zeolite MOR at 250°C, space velocity of 4.3 L/min/$g_{sorbent}$ and partial pressures of water and methanol of 0.6 bar.

Co-adsorption is further confirmed by the single temperature peak observable in the upper graph of Figure 31, coinciding with the breakthrough timing in the lower graph.
The upper graph also highlights the difference in the real-time measurement of the two thermocouples placed at the bottom (TT-609) and at the top (TT-604) of the sorbent bed. The delayed peak measured by TT-604 provides the means for qualitative temperature profile determination along the length of the bed during adsorption.

Following the outcomes indicated in Figures 29 and 30, competitive water-CO_2 adsorption was investigated at 250°C for MOR and 4A only. The same partial pressure of water (0.6 bar) was tested for CO_2 competitive adsorption, for which results are again expressed in terms of the water adsorption capacity (Figure 32).

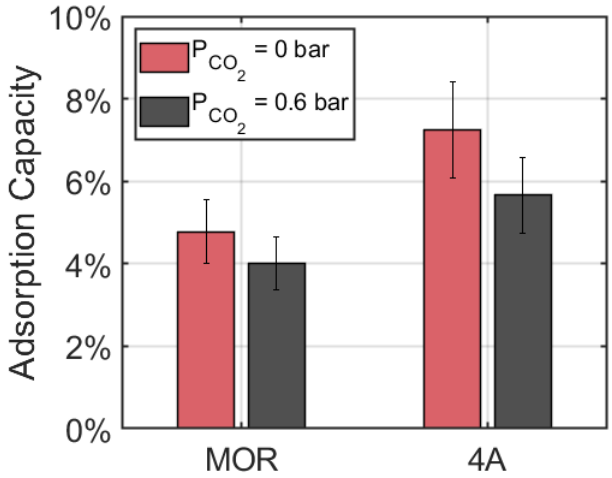

Figure 32 Water adsorption capacity of MOR and 4A w/o and with presence of CO2 in the gas feed with the same partial pressure of water of 0.6 bar, reducing the amount of tracer inert gas.

Figure 32 illustrates that the presence of CO_2 in the feed had an impact on the water adsorption capacity of MOR and 4A, resulting in a reduction of 16% and 22%, respectively. These findings align with previous research, which reported a 15-20% decrease in the water adsorption capacity of zeolite 4A when a 2.4% CO_2 content was present in the feed gas mixture [60]. The same study indicated a low adsorption capacity for CO_2, consistent with MiWi experimental results. The reduced water adsorption capacity of MOR and 4A in the presence of CO_2 is again explained by the larger pore size with respect to CO_2 kinetic diameter.

A second set of experiments verified that there was no reaction occurring on the acid sites of the zeolite MOR when CO_2 is combined with hydrogen in a stoichiometric ratio and sent as a dry gas mixture to the reactor at 250°C [61].

Impact of the water partial pressure on adsorption capacity:
The final focus of this set of experiments was the investigation of the water adsorption capacity under variations in the water partial pressure at 250°C.

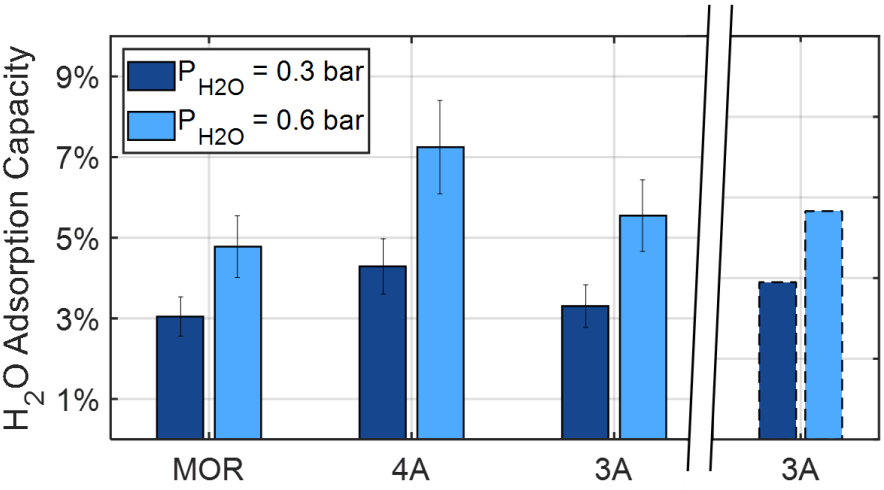

Figure 33 Variation of MOR, 4A and 3A water adsorption capacity with respect to partial pressure of water in inert gas. The adsorption capacity of molecular sieve 3A compared with literature studies [57].

A 50% reduction in the partial pressure of water in inert gas led to a significant decrease of 36 and 40% in the adsorption capacity of MOR and 4A, respectively, at 250°C and a space velocity of approximately 4 L/min/$g_{sorbent}$. This suggests that neither pure physisorption nor strong chemisorption is the sole driving mechanism. The adsorption capacity of zeolite 3A for different water partial pressures was again compliant with literature studies. The values corresponding to water partial pressures of 0.3 and 0.6 bar are depicted as dotted lines in Figure 33, revealing a 30% decrease when the partial pressure is halved.

All the above-described findings reveal that molecular sieves 3A and 4A are the best-suited sorbents for SE methanol synthesis due to their high adsorption capacity. The high selectivity of 3A towards water facilitates modeling work and increases the purity of the final product, eliminating the need for downstream units separating methanol from water and ensuring lower DME formation. This zeolite was widely investigated for the enhancement of CO_2 hydrogenation reactions; however, these studies also report the synergic enhancement of CO production through reverse water gas shift reaction (RWGS) [62], [63].

For an easier comparison of the refined processes, we conducted further experimental work with increased partial pressure of water at 250°C over molecular sieve 3A. The results are reported in Figure 34 and compared with the work of Kampen et al., showing strong consistency again.

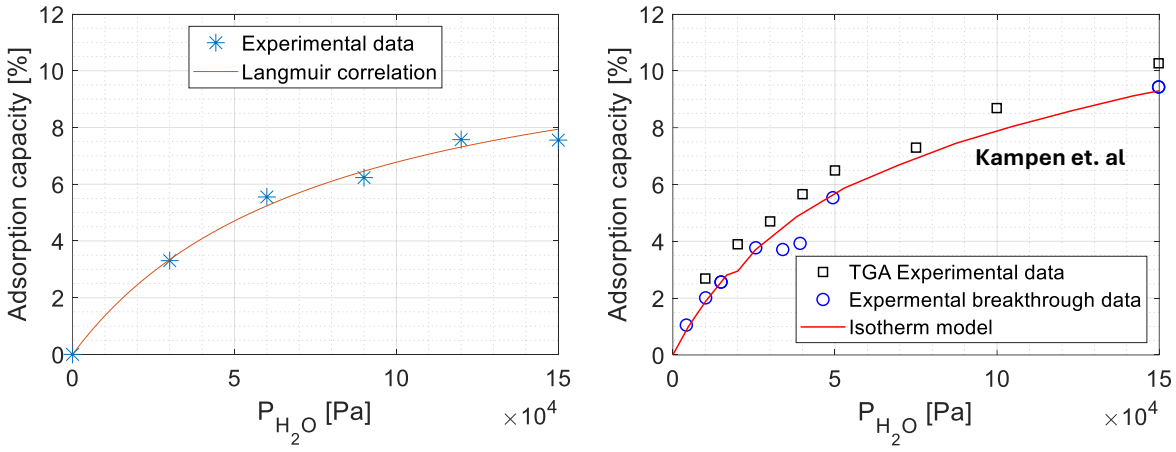

Figure 34 Left graph: adsorption isotherms of water vapor in zeolite 3A at 250°C resulting from MiWi breakthrough experimental data and fitting of Langmuir model; Right graph: adsorption isotherms of water vapor in zeolite 3A at 250°C resulting from TGA measurements (black squares), breakthrough experiments (blue circle), and fitting of condensation model performed by Kampen et. al [58].

The further variations in the water partial pressure for selective adsorption using molecular sieve 3A facilitated the estimation of Langmuir parameters used in simulations for SE methanol synthesis at higher pressures. The parity plot in Figure 35 indicates a maximum deviation of 5% between experimental results and the Langmuir model predictions.

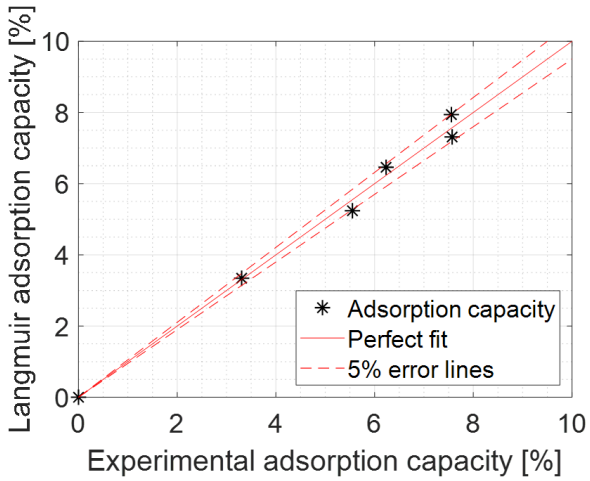

Figure 35 Comparison between Langmuir and experimental adsorption capacities, with a perfect fit line and ±5% error margins.

(B) Methanol synthesis without product adsorption

In this set of experiments, a sequential decrease in temperature was established to acquire information on the methanol and carbon monoxide production at the equilibrium (Figure 36) over KATALCO 51-102 CZA at the constant relative pressure of 2 barg, being the following two reactions concurring to CO_2 hydrogenation:

Methanol Synthesis Reaction (from CO_2):

$CO_2 + 3H_2 \leftrightarrow CH_3OH + H_2O$ $\Delta H = -49.5$ kJ/mol (exothermic)

Reverse Water-Gas Shift (RWGS) Reaction:

$CO_2 + H_2 \leftrightarrow CO + H_2O$ $\Delta H = +41.2$kJ/mol (endothermic)

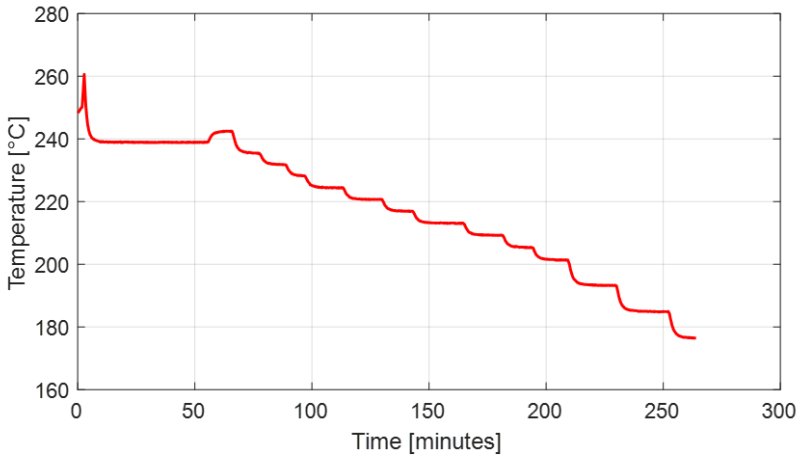

Figure 36 Temperature profile over time for fixed-bed experiments of methanol synthesis without product adsorption.

The outlet gas concentration was measured using the GSD 301 O1 spectrometer. In Figure 37, the signals are presented as intensity, revealing the effect of temperature on the equilibrium concentration of the gas mixture. Lower reactor temperatures result in higher methanol signal intensities, indicating increased methanol production. Conversely, as the reactor temperature decreases, the production of CO and H_2O decreases, as reflected by the diminishing signal intensities.

While the mass spectrometer (MS) provides valuable insights into the ongoing reactions, its signals require calibration against another device capable of measuring absolute molar concentrations, such as the NDIR (Figure 38). The NDIR is positioned at the final stage of the MiWi facility, after the condensation phase, where only a dry gas stream containing different proportions of inert and active gases is analyzed.
Figure 38 displays the molar concentrations of CO and CO_2 during standard methanol synthesis as reactor temperature decreases. A reduction in CO concentration suggests higher methanol yield, while increased CO_2 concentrations indicate overall lower conversion.

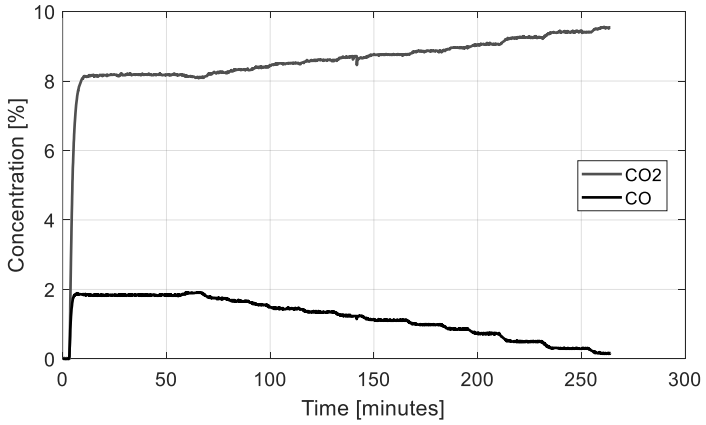

Figure 37 Signals intensity at the mass spectrometer over time for fixed-bed experiments of methanol synthesis without product adsorption.

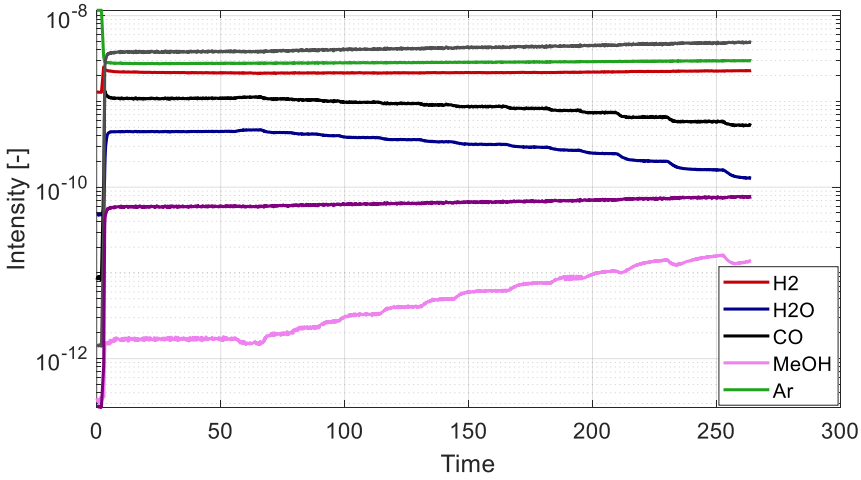

Figure 38 Signals intensity at the NDIR over time for fixed-bed experiments of methanol synthesis without product adsorption.

These measurements allowed for the determination of the selectivity of the methanol synthesis and RWGS reactions over the commercial $Cu/ZnO/Al_2O_3$ catalyst at the low constant relative pressure of 2 barg. The selectivities are pictured for the analyzed temperatures in Figure 39.

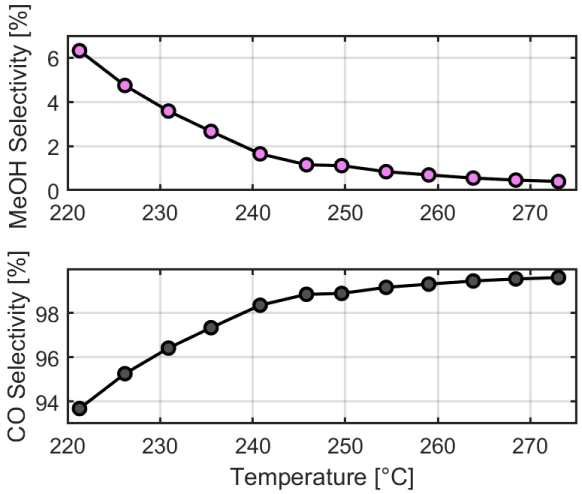

Figure 39 Selectivity of Methanol (MeOH) and RWGS reactions as a function of Temperature over a commercial $Cu/ZnO/Al_2O_3$ catalyst at the low constant relative pressure of 2 barg.

The plot illustrates the effect of temperature on the selectivity of methanol synthesis versus the reverse water-gas shift reaction. As temperature increases, the selectivity towards methanol production decreases, while the selectivity for RWGS (and thus CO production) becomes more dominant. The selectivity shift in the plot reflects the opposing thermodynamic behaviors of these reactions: methanol synthesis is favored at lower temperatures due to its exothermic nature, while the endothermic RWGS reaction is promoted at higher temperatures.

The overall CO_2 conversion at 250°C returned a selectivity towards methanol production of < 2%, corresponding to a methanol yield of 0.19% and a CO yield of 13.9%. Figure 40 illustrates the overall CO_2 conversion with corresponding variations in methanol and CO yields as a function of temperature.

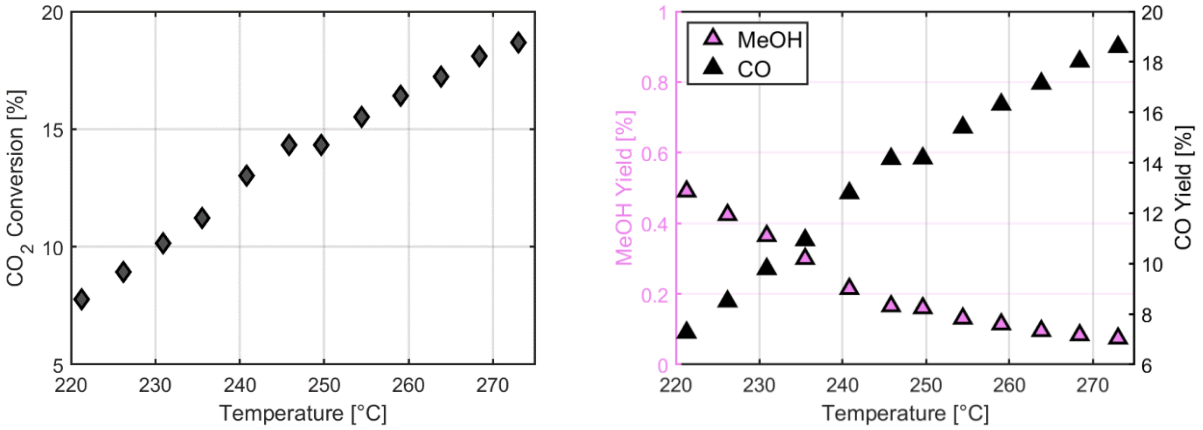

Figure 40 Effect of temperature on CO_2 conversion and product yields. The left plot shows the increase in overall CO_2 conversion as the temperature rises from 200°C to 270°C. The right plot illustrates the corresponding changes in methanol (MeOH) and carbon monoxide (CO) yields with increasing temperature.

Following the findings from section (B), we tested sorption-enhanced methanol synthesis between 220°C and 250°C over molecular sieve 3A, which is expected to enhance both methanol and CO production by selective water adsorption.

(C) Methanol synthesis with product adsorption

For SE methanol synthesis, performed under fixed and fluidised bed configurations, the facility was upgraded with a system of 5 thermocouples for additional information on the temperature profile.

For both fixed and fluidised bed configurations, three experiments were conducted with a mixed bed of 3A and CZA under temperatures of 220, 235, and 250°C. The respective measurements of the mass spectrometer for methanol (in pink) and water (in blue) and the thermocouples system are reported in the upper and lower graphs of Figure 41.

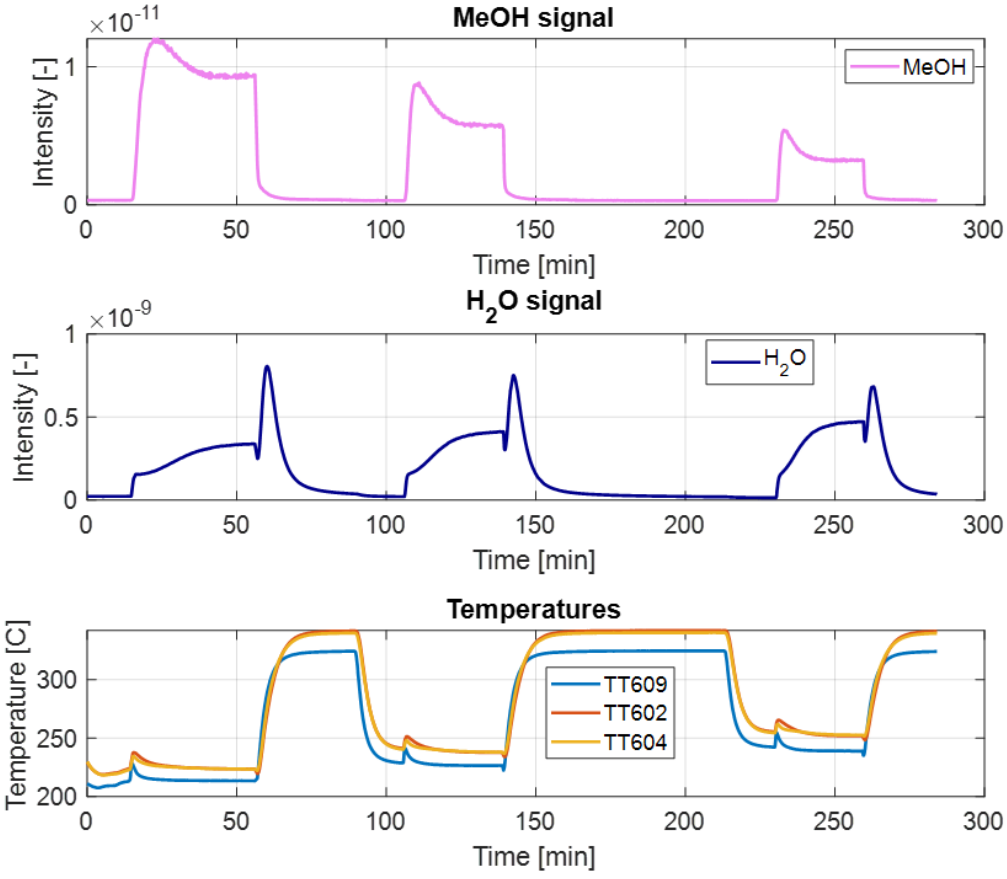

Figure 41 Time-resolved analysis of methanol (MeOH) and water (H_2O) signals, alongside temperature profiles, during three different experiments at 220, 235, and 250°C over a fixed bed CZA-3A configuration. The top panel shows the intensity of methanol detected over time, while the middle panel illustrates the corresponding water signal. Both compounds exhibit peaks aligned with temperature variations shown in the bottom panel. The temperature profiles in the bottom (TT609), middle (TT602), and top (TT604) of the catalyst-sorbent bed indicate different sensor readings during heating and cooling phases, correlating with methanol and water production and adsorption cycles.

The two phases of SE reaction and desorption are distinguishable for each experiment. When the reaction starts, a peak in temperature is observed, corresponding to a peak in the MeOH signal, which represents enhanced production during the water absorption. As the water signal progressively

approaches the sorbent saturation level, the methanol signal lowers to the equilibrium value associated with the reactor temperature. As the sorbent reaches saturation, a stable intensity value for both water and methanol is identified. The desorption phase is conducted at a higher temperature to regenerate the sorbent before restarting with the next experiment. A peak in the water signal is detected as water is released from the sorbent. A similar peak is not observed in the methanol signal due to the high selectivity of zeolite 3A towards water, preventing the adsorption of bigger molecules.

Due to the decrease in the water adsorption capacity with increasing temperature, the sorption enhancement effect is shorter in time with the following trend: SE at 220°C > SE at 235°C > SE at 250°C. The same trend applies to the methanol intensity, being higher at lower temperatures. The opposite trend characterizes the water signal, whose intensity is higher for higher temperatures. This is in accordance with the increase in CO production detected at the NDIR for higher temperatures (Figure 42).

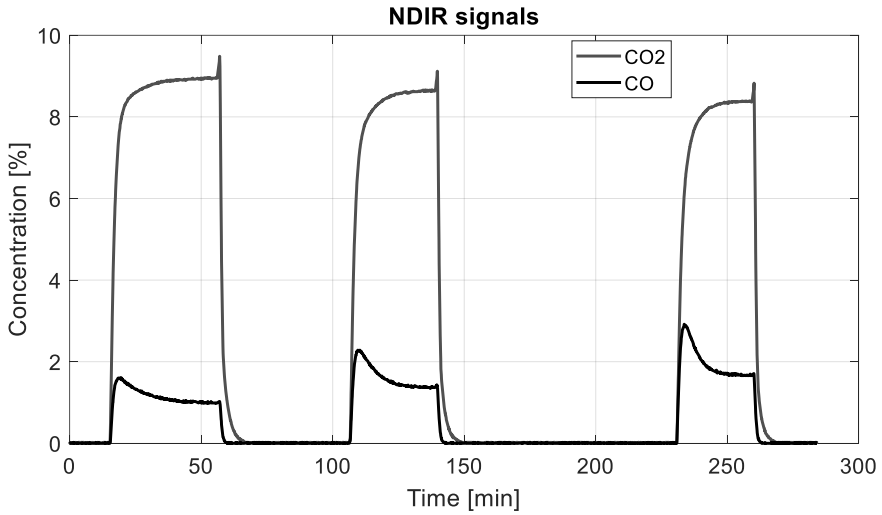

Figure 42 Concentration profiles of CO_2 and CO over time during three different experiments at 220, 235, and 250°C over a fixed bed CZA-3A configuration. The graph shows increasing CO concentrations with increasing reactor temperature. On the contrary, CO_2 exhibits lower concentrations in the product gas with increasing temperature, indicating a higher conversion.

As per the methanol production during the experiment, the CO produced by the RWGS reaction is subjected to an enhancement before stabilizing at the equilibrium level of the operating temperature and pressure when the sorbent saturates.

The same trend is observed for a fluidized-bed configuration of CZA-3A with a 1:1 ratio.

Figure 43 compares the CO enhancement registered at the NDIR during the **fluidization** of the catalyst-sorbent mixture for the three experimental temperatures of 220, 235 and 250°C. It can be seen again that the higher the temperature, the higher sorption-enhancement registered for CO, and the shorter the enhancement effect. It can also be observed that the higher the temperature, the higher the conversion of CO_2, for which a lower percentage is registered at the NDIR.

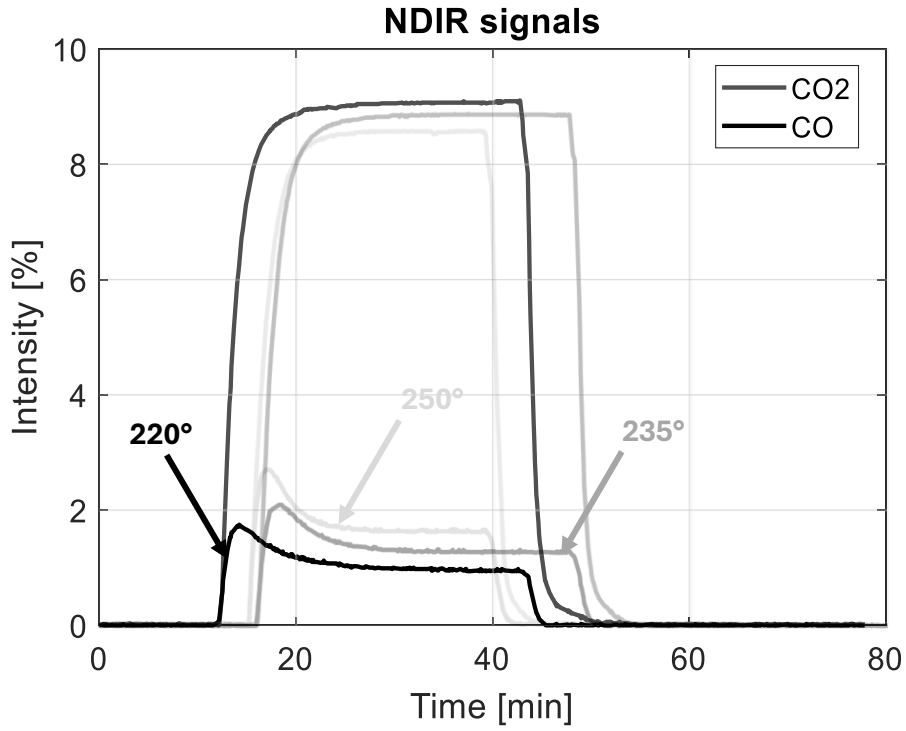

*Figure 43 Concentration profiles of CO_2 and CO over time during three different experiments at 220 (black line), 235 (dark gray line), and 250°C (light gray line) over a **fluidized** bed CZA-3A configuration. The graph shows increasing CO concentrations with increasing reactor temperature. On the contrary, CO_2 exhibits lower concentrations in the product gas with increasing temperature, indicating a higher conversion.*

Figure 44 shows again the time-resolved analysis of temperature, methanol (MeOH) and water (H_2O) signals for a **fluidized** catalyst-sorbent bed configuration at the three experimental temperatures of 220 (A), 235 (B) and 250°C (C). It can be observed that while the methanol enhancement is only slightly higher in a fluidized bed configuration when compared to fixed bed measurements in Figure 20, the fluidized bed configuration allowed for an isothermal temperature profile along the reactor. The trend characterizing a higher methanol production for lower temperatures with an increased adsorption capacity is, again, respected.

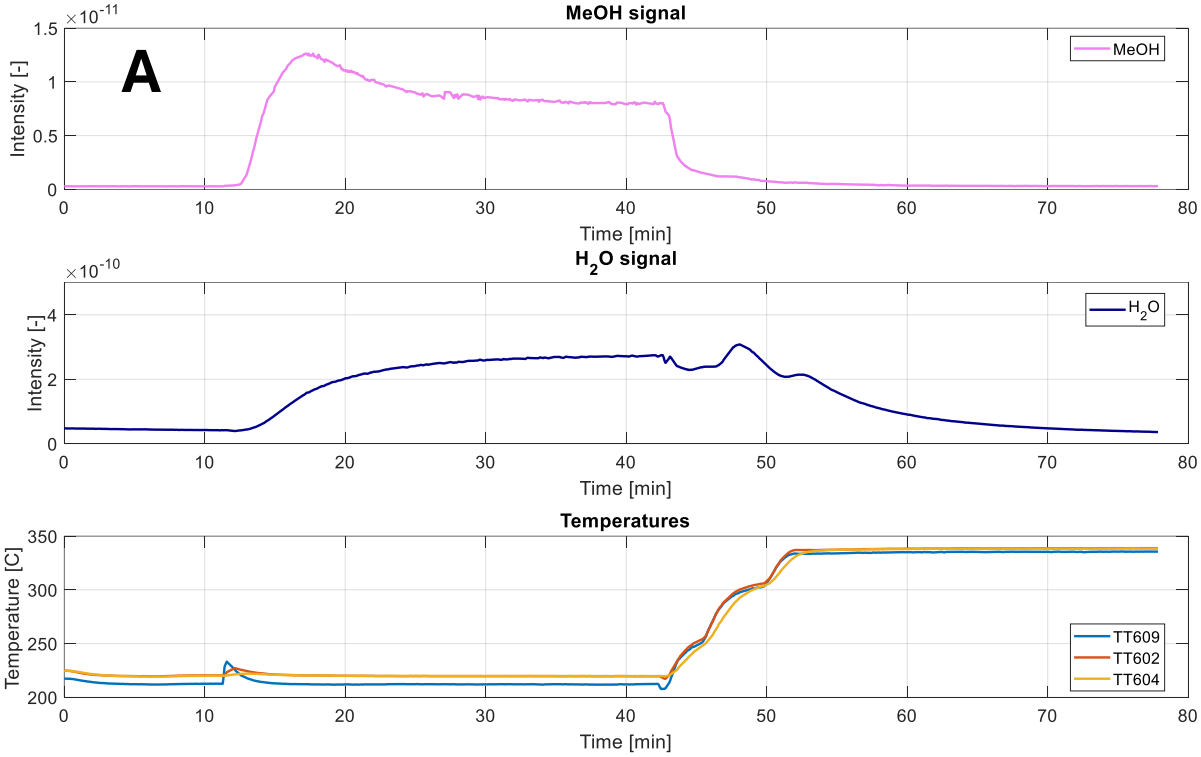
A
MeOH signal
×10^-11
Intensity [-]
MeOH
Time [min]
H2O signal
×10^-10
Intensity [-]
H2O
Time [min]
Temperatures
Temperature [C]
TT609
TT602
TT604
Time [min]

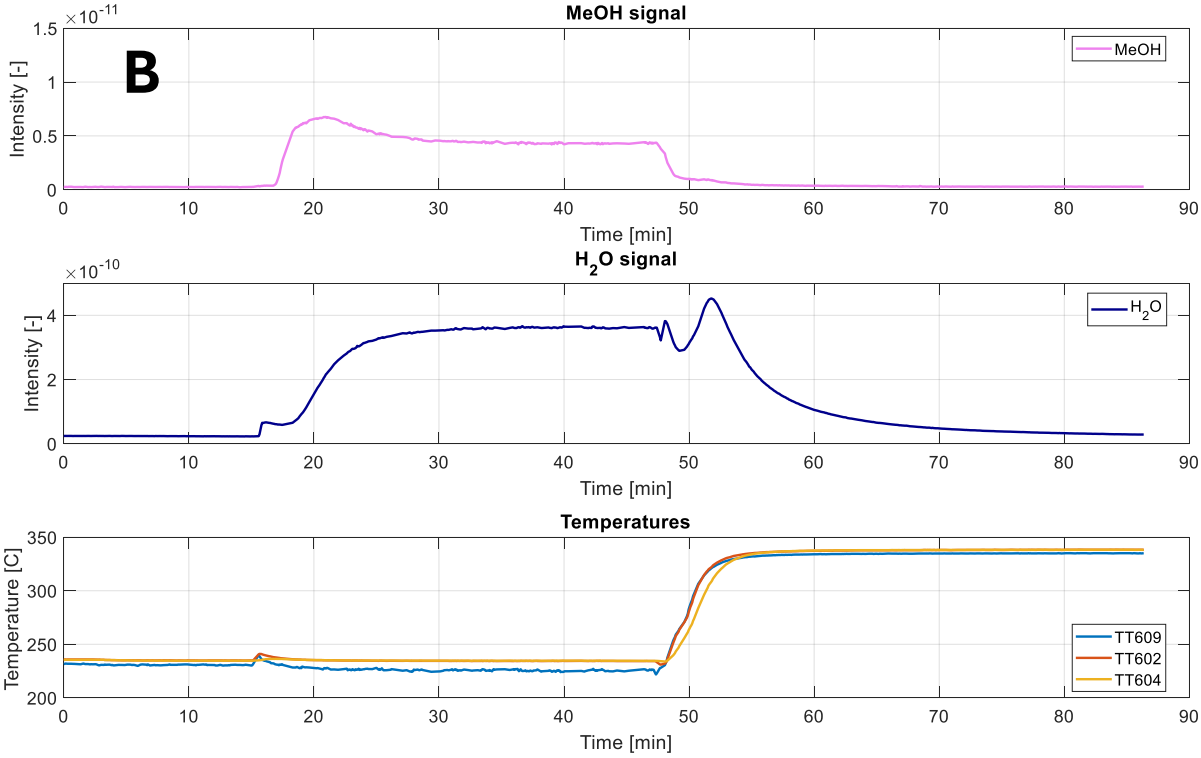
B
MeOH signal
×10^-11
Intensity [-]
MeOH
Time [min]
H2O signal
×10^-10
Intensity [-]
H2O
Time [min]
Temperatures
Temperature [C]
TT609
TT602
TT604
Time [min]

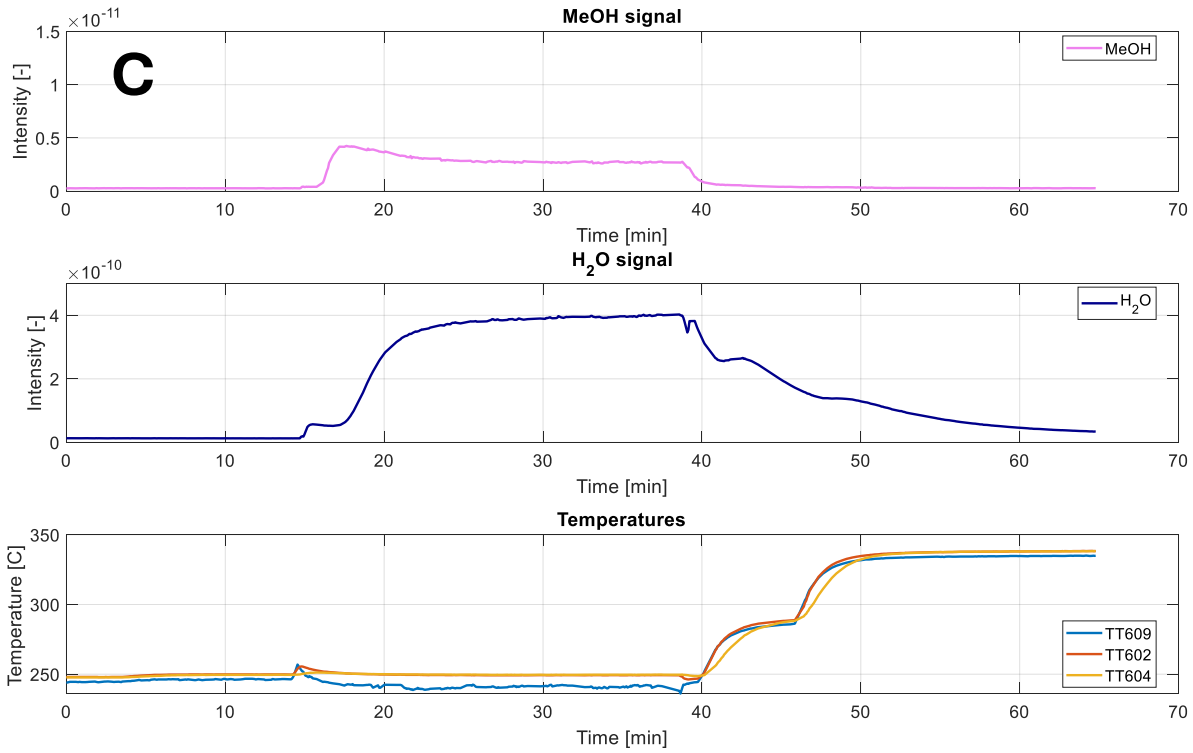

*Figure 44 Time-resolved analysis of methanol (MeOH) and water (H_2O) signals, alongside temperature profiles, during three different experiments at 220 (A), 235 (B), and 250°C (C) over a **fluidized** bed CZA-3A configuration. The top panel shows the intensity of methanol detected over time, while the middle panel illustrates the corresponding water signal. The temperature profiles in the bottom (TT609), middle (TT602), and top (TT604) of the catalyst-sorbent bed exhibit isothermicity along the reactor, typical of fluidization.*

Key stages of the methanol signal treatment:

Once the final product concentrations at the equilibrium are measured through the NDIR, the corresponding value is reported to the intensity level measured at the mass spectrometer. The signal onset and maximum peak are then identified (stage 1, represented in Figure 45).

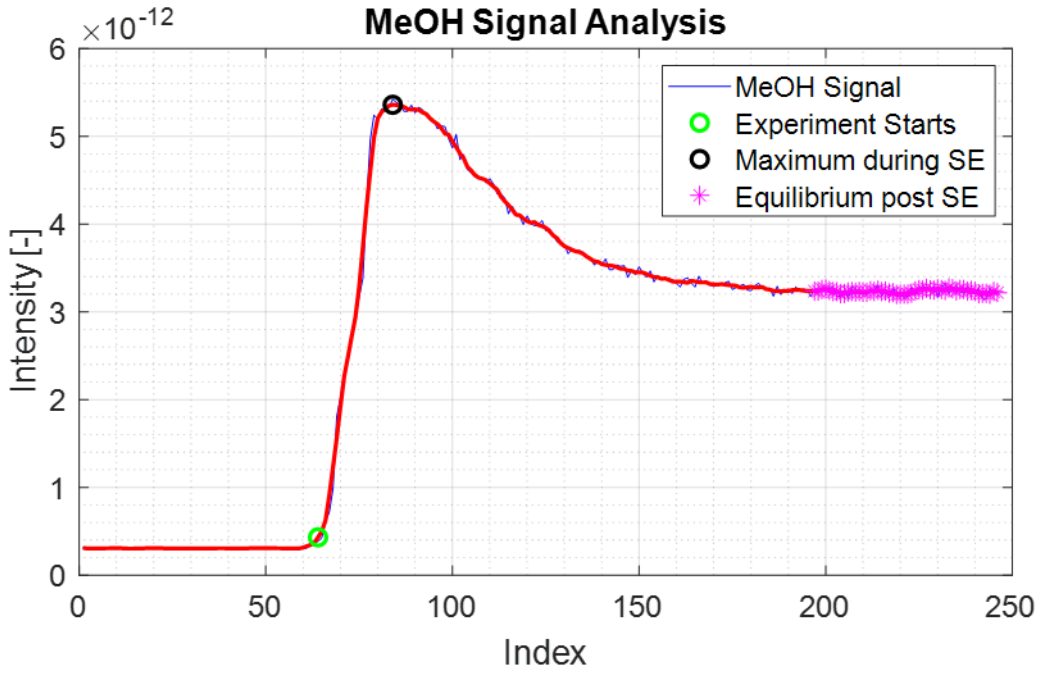

*Figure 45 First stage of the methanol signal postprocessing, identifying the equilibrium level after sorption enhancement through the NDIR measurements (pink *), onset (green open circle), and maximum peak (black open circle) representing SE.*

The equilibrium level is reported at the onset line to detect the area exposed to sorption enhancement (stage 2, represented in Figure 46). By extending the stabilization line to the breakthrough phase, it is possible to estimate the time and quantity of methanol production during adsorption. The intersection point is selected as the recorded closest value to the intersection between the MeOH signal and the stabilization line.

In the final stage, represented by Figure 47, the signal is scaled to the flow of methanol in ml/min according to stage 1, and the area of interest (in green), representing the additional methanol produced, is integrated. The red curve in the figure represents the filtered MeOH signal to assess this processing step. However, this filtered line has not been further employed for any calculation.

A comparison between the areas covered by the sorption-enhanced and standard conversion areas provides key information to determine the methanol yield during both stages.

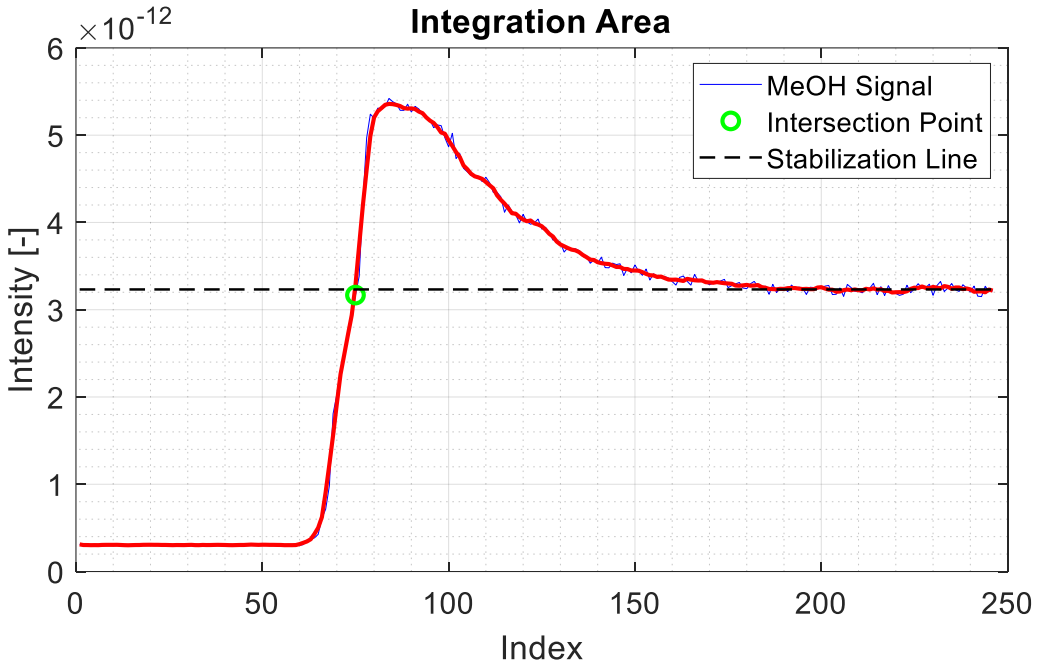

Figure 46 Second stage of the methanol signal postprocessing, identifying the equilibrium level on the onset line (green open circle) to delimit the integration areas.

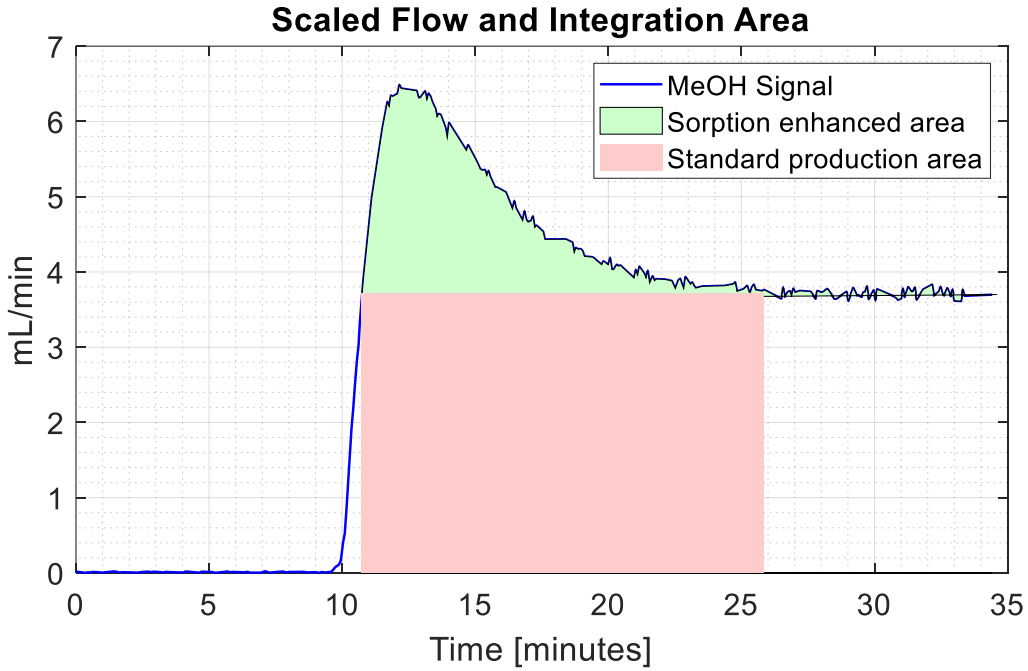

Figure 47 Third stage of the methanol signal postprocessing, scaling the intensity vector to the methanol flow in Nml/min and integrating the sorption-enhancement area to determine the additional methanol produced during adsorption.

The same procedure was applied to analyze the results obtained for the fluidised bed configuration at the three different temperatures of 220, 235, and 250°C. The key findings are reported below.

Key findings:

Figure 48 presents our results at 250°C with increased intensity registered at the mass spectrometer during synthesis. As explained before, the amount of methanol measured at the reactor outlet decreases when the breakthrough of water occurs, indicating saturation of the sorbent bed. The integration of the marked area provides additional methanol due to sorption enhancement, corresponding to 21.2%. On the right, the vertical temperature profile measured along the reactor length by the new 5-thermocouples system can be observed. The temperature difference along the reactor is typical of fixed bed configurations.

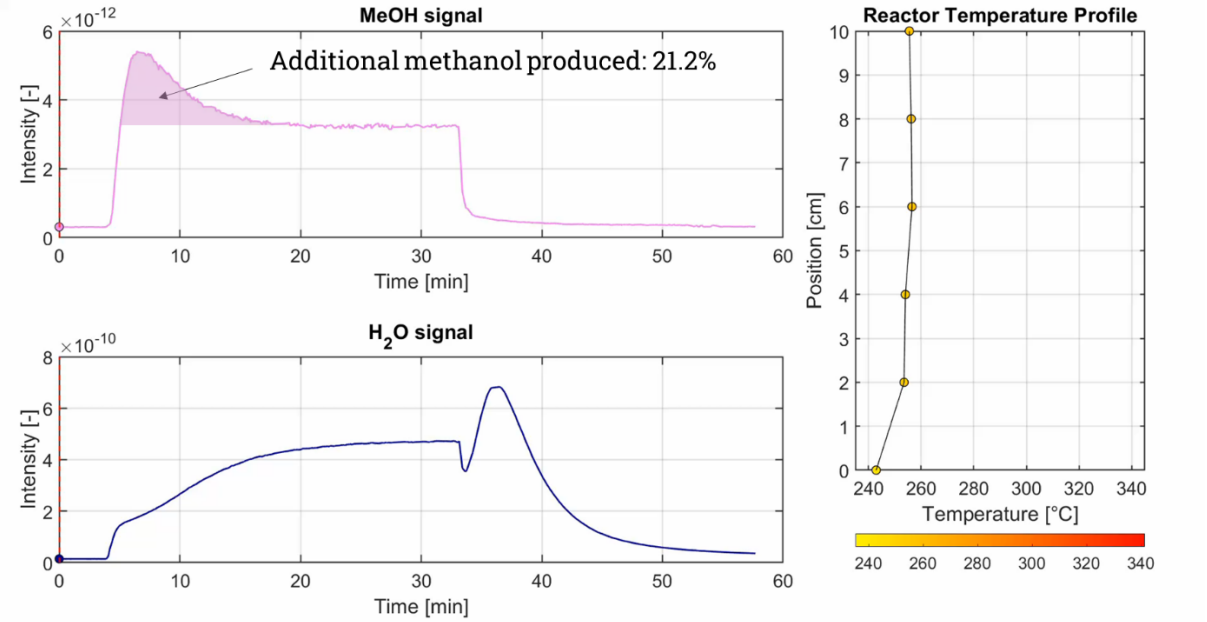

Figure 48 Dynamic temperature and gas analysis in a fixed bed reactor during sorption enhanced methanol synthesis over a CZA-3A mixture at 250°C and 2barg.

The same behavior can be observed in Figure 49 when fluidising the mixture of sorbent and catalyst bed. The temperature graph highlights the isothermal profile registered by the thermocouples, typical of fluidised bed configurations, while the additional methanol remained in the range of the fixed bed experiments (24.5%). Again, only water is desorbed from the zeolite.

Despite a temperature gradient, the similar sorption enhancement (21.2%) resulting from fixed-bed experiments suggests that the potential of the new reactor concept lies in entraining the sorbent bed before saturation to maintain continuous enhancement and maximize methanol production.

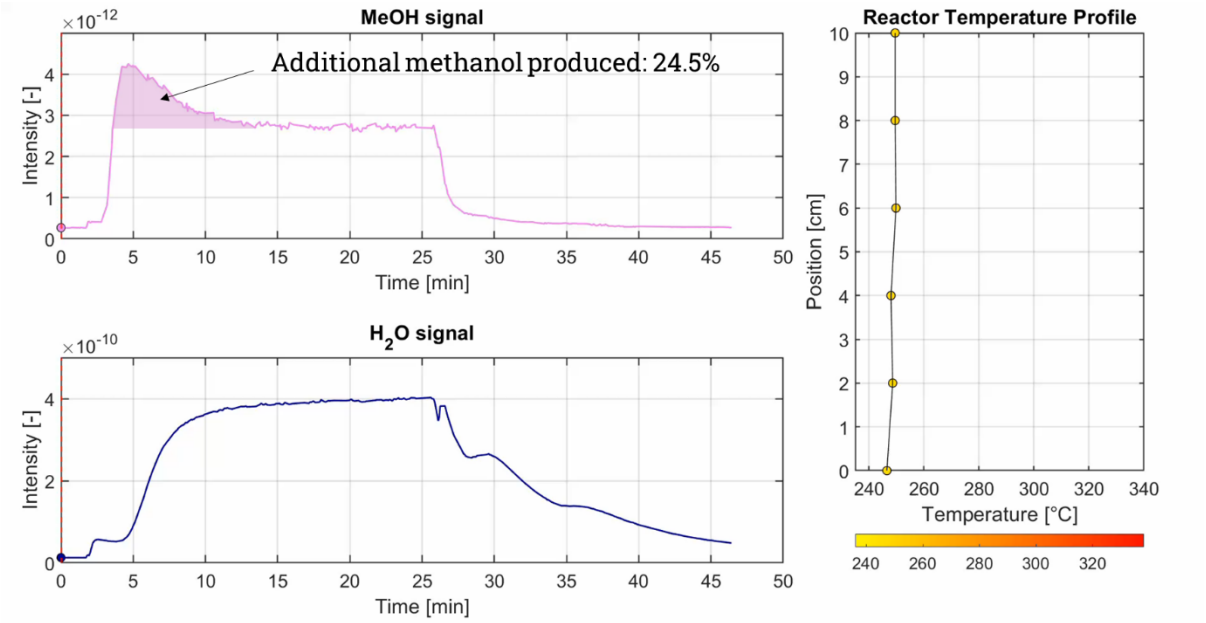

Figure 49 Dynamic temperature and gas analysis in a fluidised bed reactor during sorption enhanced methanol synthesis over a CZA-3A mixture at 250°C and 2barg.

Comparison of processes refined

The parameters obtained from the experimental work were used in MATLAB dynamic simulations for sorption-enhanced methanol synthesis in fixed-bed reactors. Figure 50 shows that, in accordance with the experiments, methanol yield is enhanced at 250°C with increasing pressure from 20 to 100 bar, but the sorption-enhancement effect is limited over time. Once the sorbent bed is saturated, the methanol yield lowers to the thermodynamic equilibrium level. At this point, methanol yield can only be enhanced with increasing pressure.

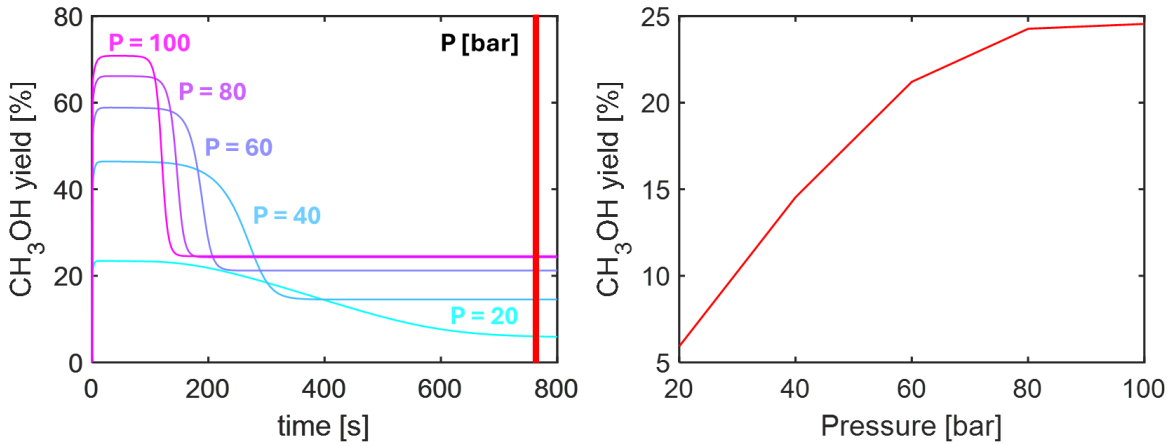

Figure 50 Preliminary modeling results for a fixed bed reactor: sorption enhancement effect with varied reactor pressure between 20 and 100 bar at 250°C.

In summary, despite a higher methanol yield obtained with increased pressure during sorption enhancement, the additional methanol production (represented by the integrated areas) remains unchanged due to the timespan decrease as the sorbent bed quickly reaches saturation (Figure 51).

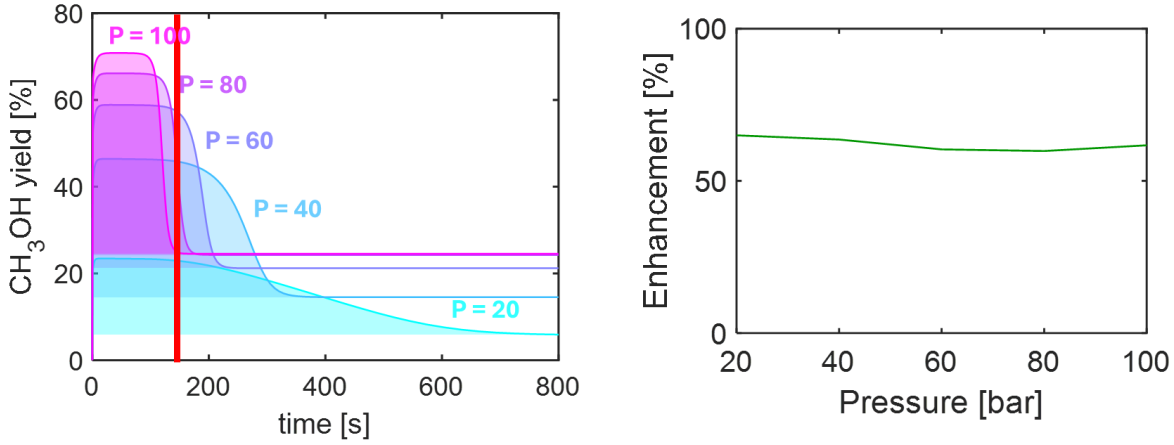

Figure 51 Overall enhancement calculation with varied reactor pressure between 20 and 100 bar at 250°C.

This effect can be overcome by increasing the reactor length, as reported in Figure 52 for a case study at 30 bar, corresponding to the typical delivery pressure of an electrolyzer. However, increasing the reactor length results in a more considerable volume of saturated material. The right graph of Figure 29 indicates that the length of the saturated sorbent bed reaches 5m after 30 minutes only (brown marked area).

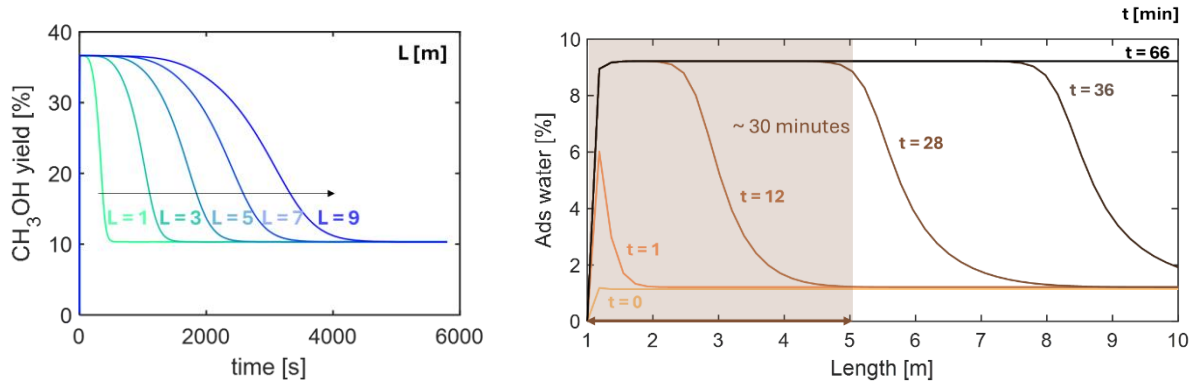

Figure 52 Left graph: effect of the reactor length on sorption enhancement for methanol synthesis at 250°C and 30 bar. Space-time representation of water adsorption during methanol synthesis by molecular sieve 3A, highlighting the trade-off between the methanol yield performance and reactor design constraints for fixed bed configurations.

A fluidised bed (catalyst) and entrained flow (sorbent) reactor can overcome the limited effect of sorption enhancement in dynamically operated fixed-bed reactors by regenerating the sorbent bed in a second vessel when saturation is reached. This way, the methanol yield can be kept at its enhanced level in more compact reactor volumes, combining the advantages of in-situ adsorption and improved temperature control.

Further improving of the methanol yield can be achieved by continuous operation.

Cold flow fluidisation experiments

The synergic fluidisation of catalyst particles and entrainment of sorbent particles was proved to be dynamically possible in a cold flow setup, a lab-scale facility we built with transparent test sections to mimic and observe the particles' movement. The facility is schematized in Figure 53.

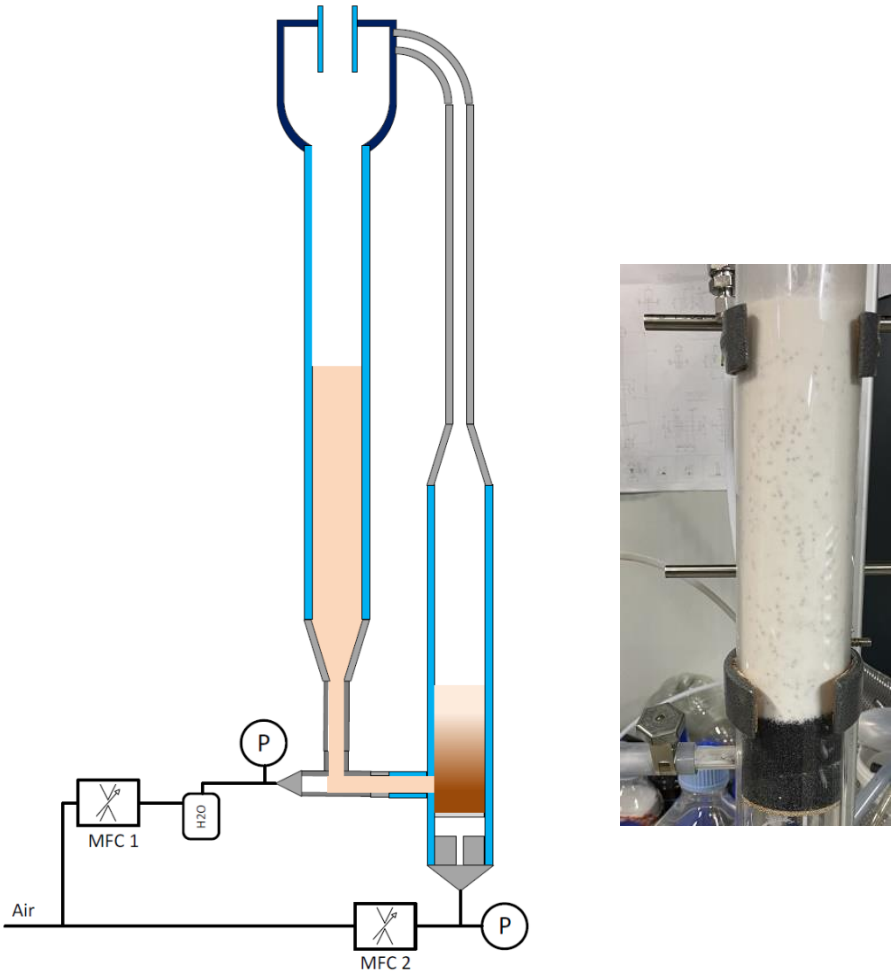

Figure 53 Schematic illustration of the cold flow setup, which demonstrates the feasibility of the new reactor concept

In this setup, white alumina particles mimicking the sorbent are entrained at 120cm height and enter the second test section at the top left before being transported back to the bottom of a fluidised bed of black sand particles, mimicking the CZA catalyst.

This system works at room temperature in a steady state when a significant difference in the fluidisation velocity of the two-particle types is applied, and pressure drops in the systems are overcome.

Uninterrupted operation for several hours was achieved repeatedly for a fluidisation number equal to 3, sand particles of 0.8mm, and alumina particles of 0.125-160mm. By this, the fluid-dynamic feasibility of the reactor concept is successfully demonstrated.

6 Evaluation of results

The results obtained show that methanol production is a critical element in the shift of energy and chemical industries towards a de-fossilised environment. In fact, the currently used methanol synthesis process (via steam reforming of natural gas) shows an important carbon footprint and strongly bases the economic performance on the availability of cheap natural gas. Hence, the shift from the fossil-based to a renewable-based synthesis may significantly increase the methanol production cost by a factor two to three. This phenomenon may open the way for the entrance in the market of new technological solutions that utilise better the renewable resources available. In particular, the localized biogas reforming can become competitive, thanks to the use of biogas as heat source, a cheaper commodity than biomethane. The methanol production from power-to-methanol (i.e. from renewable H_2) can be also beneficial, as it can take advantage of cheap H_2 and CO_2, providing a competitive methanol production with a low environmental impact.

In the context of biogas utilisation, it was observed that the combined heat and power technology, currently leader on this market, might lose in competitiveness due to changing support schemes. Hence, the biogas valorisation towards other products, such as biomethane and bio-methanol can be beneficial, thanks to the better adaptation to the market demand, due to the possibility of product storage. In particular, methanol appears as the most promising product molecule, thanks to the higher market value. However, the most suitable methanol production scheme offers the co-production of biomethane and bio-methanol, avoiding the direct combustion of the methane contained in biogas.

In this study, it was observed that the biogas plants might become a platform for energy storage, offering the climate neutral CO_2 required for the synthesis of appropriate energy carriers. In this context, it was shown that the selection of the most appropriate energy carrier to use depends on the final energy carrier to produce after the storage. It was observed that methane is has a slight advantage as molecule to use for the storage of electricity, thanks to the possibility of producing electricity from methane in a combined cycle. For the storage of H_2, methanol is slightly better suited thanks to the lower temperature required from the reforming reaction.

The results show that biogas valorisation in methanol has a potential, especially in the context of H_2 storage. An optimal utilization of biogas would couple biogas upgrading and the use of the waste biogenic CO_2 stream in a methanol plant aimed at producing this molecule for H_2 storage. Additionally, as the methanol production via the standard natural gas reforming process may become significantly more expensive due to its important carbon footprint, the small-scale methanol production from biogenic CO_2 may gain a significant market share in the future. Hence, it is beneficial to develop a new reactor technology specifically addressed at the conversion of biogenic CO_2 in the context of energy storage. To this scope, the new reactor should be able to achieve high CO_2 without utilizing high pressure or high recycle rates, as both options require significant amounts of electricity (hence not adapting well to the energy storage context).

In order to develop this new technology, the possibility of developing a sorption-enhanced methanol synthesis was selected as the most promising option. This is based on the consideration that the in-situ water removal is the most energy-efficient way to overcome the thermodynamic limitation present in methanol synthesis. To this scope, two main technologies will be assessed: the dynamic fixed-bed reactor and the entrained flow reactor. The former technology is characterised by a simple construction, counterbalanced by the need of having several units operating either in the reaction phase or in the regeneration of the sorbent. The latter technology can instead be operated continuously, but the reactor shows a higher complexity (due to the continuous movement of the catalyst and sorbent). These two reactors were modelled and analysed in detail to determine the respective pros and cons. The equipment was optimized in terms of productivity and dimension.

In the next step, we compared the performance of dynamic fixed bed, entrained flow and mixed entrained/fluidised bed reactors in the sorption-enhanced methanol synthesis. All the reactors are suitable to perform the desired process, but each of them presents pros and cons. The dynamic fixed bed reactor can achieve high methanol yield, thanks to the high utilisation of the sorbent (up to the saturation point). However, this reactor is intrinsically discontinuous, as the sorbent must be regenerated. Consequently, the operation requires at least two reactors in series, hence demanding a high amount of catalyst per unit of methanol. The entrained flow reactor achieves a continuous operation of the sorption-enhanced methanol synthesis, but is characterised by a large superficial gas velocity, required to entrain sorbent and catalyst. A better compromise in terms of reactor dimensions and space time yield is achieved by separating the flow pattern of catalyst and sorbent in the reactor, with the former being maintained in the reactor and the latter being entrained. In this case, ad adequate methanol yield is achieved also with higher space velocity. However, the methanol selectivity in this reactor is about 60 %, so that further processing of the coproduced CO is required.

The results of this study demonstrate that it is not possible to identify a reactor that clearly shows the best performance in the sorption-enhanced methanol synthesis. The optimal reactor technology strongly pends on external factors, such as required productivity and product purity, availability of heat for the sorbent regeneration and size of the equipment. In fact, these elements influence the number of alternating units required in the dynamic fixed bed reactor operation or the size of the post-processing unit to convert CO after the entrained/fluidised bed reactor. In general, it can be observed that the dynamic fixed bed reactor is particularly suitable to produce high amounts of methanol when a fast exchange of the reactive units is possible (i.e. when it is possible to install several units in parallel). The hybrid the entrained/fluidised bed reactor could show a better performance for applications that require high CO_2 conversion in a single stage (e.g. small-scale applications). Therefore, this reactor concept was chosen for further experimental investigation at TRL 2-3.

The experimental investigation of the reactor concept tested sorbents chosen based on the literature study and commercial catalyst. Aim of these experimental activities was the technical verification of suitability of sorbents, reaching a technology readiness level (TRL) of 2-3. In this phase, the effect of various sorbents was analysed varying operation parameters such as temperature, flow rates, water and CO_2 concentration. Detailed quantitative results were obtained that are in line with literature findings validating our experimental approach.

In the next step, catalyst and sorbent were mixed in the reactor and tested for batchwise sorption enhancement in both, fixed and fluidised bed arrangement, i.e., with different particle sizes.

While the temperature graphs highlight the isothermal profile typical of fluidised bed configurations, the additional methanol production remained in the range of the fixed bed experiments (24.5%). The similar sorption enhancement (21.2%) resulting from fixed-bed experiments suggests that the potential of the new reactor concept lies in entraining the sorbent bed before saturation to maintain continuous enhancement and maximize methanol production.

To test the fluid-dynamic feasibility of a bubbling fluidised bed with entrained smaller particles moving through it, a cold-flow model was successfully tested for this most critical step. In this setup, white alumina particles mimicking the sorbent are entrained and enter a second vessel (replacing the regenerator) before being transported back to the bottom of a fluidised bed of black sand particles, mimicking the CZA catalyst.

Uninterrupted operation for several hours was achieved repeatedly which successfully demonstrates the fluid-dynamic feasibility of the reactor concept.

7 Next steps

With the obtained data from the lab, in future projects, a rate-based model of a reactor with entrained sorbent particles can be set up and used for simulating different configurations and operation conditions. Together with first experimental results in a larger reactor, the concept then can be scaled-up to TRL 4/5. This will allow long duration tests and will give detailed data both for model validation and improved economic assessment. The first experiments in larger scale will take place within the framework of the European Union project HERMES, while the modelling work and the building of a TRL 4/% set-up are part of the activities in the refuel.ch project fnded within the SFOE SWEET program.

8 National and international cooperation

The preliminary results of the project were discussed in the first Swiss methanol workshop organized by the Ostschweizer Fachhochschule in Rapperswil, on 25.11.2021.

Results of this project enabled successful funding proposals leading to work packages that are part of the European Union project HERMES and of the BfE-SWEET project refuel.ch

9 Communication

Selected results from the project were presented during an oral contribution at the 13th European Congress of Chemical Engineering (online conference) on 20.09.2021, with the title: "*Challenges and opportunities in the coupling of power-to-methanol and biogas upgrading*"

Further, an oral contribution at the International Symposium on Chemical Reaction Engineering (ISCRE) in Turku (Finland) in May 2024 presented part of the experimental results.

10 Publications

The results here presented are reported in the following publications:

1. E. Moioli, H. Madi, T. Schildhauer, Comprehensive Analysis of Renewable Energy Integration in Decarbonised Mobility: Leveraging Power-to-X Storage with Biogenic CO2 Sources, accepted for publication in Energy Conversion and Management
2. E. Moioli, T. Schildhauer, Tailoring the Reactor Properties in the Small-Scale Sorption-Enhanced Methanol Synthesis, Chemie Ingenieur Technik 95, Special Issue: Reaktionstechnik und Wärme- und Stoffaustausch, 631-641 (2023), https://doi.org/10.1002/cite.202200200
3. E. Moioli, T. Schildhauer, Techno-economic-environmental assessment of the integration of power-to-X and biogas utilization towards the production of electricity, hydrogen, methane and methanol, Sustainable Energy Fuels, 2023,7, 2690-2706, https://doi.org/10.1039/D3SE00052D
4. E. Moioli, A. Wötzel, T. Schildhauer, Feasibility assessment of small-scale methanol production via power-to-X, Journal of Cleaner Production 359 (2022), 132071, https://doi.org/10.1016/j.jclepro.2022.132071

11 References

[1] A. Bosmans, I. Vanderreydt, D. Geysen, L. Helsen, The crucial role of Waste-to-Energy technologies in enhanced landfill mining: A technology review, J. Clean. Prod. 55 (2013) 10–23. https://doi.org/10.1016/j.jclepro.2012.05.032.

[2] R. Kadam, N.L. Panwar, Recent advancement in biogas enrichment and its applications, Renew. Sustain. Energy Rev. 73 (2017) 892–903. https://doi.org/10.1016/j.rser.2017.01.167.

[3] J.P. Sheets, A. Shah, Techno-economic comparison of biogas cleaning for grid injection, compressed natural gas, and biogas- to-methanol conversion technologies Johnathon, Biofuels, Bioprod. Biorefining. 12 (2017) 412–425. https://doi.org/10.1002/bbb.

[4] S.E. Hosseini, M.A. Wahid, Development of biogas combustion in combined heat and power generation, Renew. Sustain. Energy Rev. 40 (2014) 868–875. https://doi.org/10.1016/j.rser.2014.07.204.

[5] F. Cucchiella, I. D'Adamo, Technical and economic analysis of biomethane: A focus on the role of subsidies, Energy Convers. Manag. 119 (2016) 338–351. https://doi.org/10.1016/j.enconman.2016.04.058.

[6] R. Kapoor, P. Ghosh, M. Kumar, V.K. Vijay, Evaluation of biogas upgrading technologies and future perspectives: a review, Environ. Sci. Pollut. Res. 26 (2019) 11631–11661. https://doi.org/10.1007/s11356-019-04767-1.

[7] W.M. Budzianowski, C.E. Wylock, P.A. Marciniak, Power requirements of biogas upgrading by water scrubbing and biomethane compression: Comparative analysis of various plant configurations, Energy Convers. Manag. 141 (2017) 2–19. https://doi.org/10.1016/j.enconman.2016.03.018.

[8] B.R. de Vasconcelos, J.M. Lavoie, Recent advances in power-to-X technology for the production of fuels and chemicals, Front. Chem. 7 (2019) 1–24. https://doi.org/10.3389/fchem.2019.00392.

[9] E. Moioli, T. Schildhauer, Negative CO 2 Emissions from Flexible Biofuel Synthesis : Concepts , Potentials , Technologies, Preprints. (2021). https://doi.org/10.20944/preprints202108.0463.v1.

[10] A. Sternberg, A. Bardow, Power-to-What?-Environmental assessment of energy storage systems, Energy Environ. Sci. 8 (2015) 389–400. https://doi.org/10.1039/c4ee03051f.

[11] J. Xu, G.F. Froment, Methane steam reforming, methanation and water-gas shift: I. Intrinsic kinetics, AIChE J. 35 (1989) 88–96. https://doi.org/10.1002/aic.690350109.

[12] F. Koschany, D. Schlereth, O. Hinrichsen, On the kinetics of the methanation of carbon dioxide on coprecipitated NiAl (O) x, Appl. Catal. B, Environ. 181 (2016) 504–516. https://doi.org/10.1016/j.apcatb.2015.07.026.

[13] K.M. Vanden Bussche, G.F. Froment, A steady-state kinetic model for methanol synthesis and the water gas shift reaction on a commercial Cu/ZnO/Al2O3 catalyst, J. Catal. 161 (1996) 1–10. https://doi.org/10.1006/jcat.1996.0156.

[14] D.M. Riley, J. Tian, G. Güngör-Demirci, P. Phelan, J. Rene Villalobos, R.J. Milcarek, Techno-economic assessment of chp systems in wastewater treatment plants, Environ. - MDPI. 7 (2020) 1–32. https://doi.org/10.3390/environments7100074.

[15] U.S. Department of Energy, Combined Heat & Power eCatalog: Recognized Packaged CHP Systems, (2021). https://chp.ecatalog.lbl.gov/.

[16] I. Angelidaki, L. Treu, P. Tsapekos, G. Luo, S. Campanaro, H. Wenzel, P.G. Kougias, Biogas

upgrading and utilization: Current status and perspectives, Biotechnol. Adv. 36 (2018) 452–466. https://doi.org/10.1016/j.biotechadv.2018.01.011.

[17] G.D. Ulrich, P.T. Vasudevan, Chemical Engineering Process Design and Economics : A Practical Guide, 2nd ed., Taylor & Francis, Bosa Roca, United States, 2004.

[18] K. Ibsen, Equipment design and cost estimation for small modular biomass systems, synthesis gas cleanup and oxygen separation equipments, San Francisco, California, 2015. http://www.nrel.gov/docs/fy06osti/39946.pdf.

[19] Swissgrid, Production and consuption electricity data for Switzerland, (2021). https://www.swissgrid.ch/en/home/operation/grid-data/generation.html#downloads.

[20] G. Collodi, G. Azzaro, N. Ferrari, S. Santos, Demonstrating Large Scale Industrial CCS through CCU - A Case Study for Methanol Production, Energy Procedia. 114 (2017) 122–138. https://doi.org/10.1016/j.egypro.2017.03.1155.

[21] J. Witte, A. Kunz, S.M.A. Biollaz, T.J. Schildhauer, Direct catalytic methanation of biogas – Part II: Techno-economic process assessment and feasibility reflections, Energy Convers. Manag. 178 (2018) 26–43. https://doi.org/10.1016/j.enconman.2018.09.079.

[22] Energie360˚, Natural gas price, (2021). https://www.energie360.ch/de/energie-360/wissen/erdgas-biogas/gaspreise/ (accessed July 26, 2021).

[23] S. Ghosh, V. Uday, A. Giri, S. Srinivas, Biogas to methanol: A comparison of conversion processes involving direct carbon dioxide hydrogenation and via reverse water gas shift reaction, J. Clean. Prod. 217 (2019) 615–626. https://doi.org/10.1016/j.jclepro.2019.01.171.

[24] E. Moioli, R. Mutschler, A. Züttel, Renewable energy storage via CO 2 and H 2 conversion to methane and methanol : Assessment for small scale applications, Renew. Sustain. Energy Rev. 107 (2019) 497–506. https://doi.org/10.1016/j.rser.2019.03.022.

[25] J. Witte, A. Kunz, S.M.A. Biollaz, T.J. Schildhauer, Direct catalytic methanation of biogas – Part II: Techno-economic process assessment and feasibility reflections, Energy Convers. Manag. 178 (2018) 26–43. https://doi.org/10.1016/j.enconman.2018.09.079.

[26] A.H. Seifert, S. Rittmann, C. Herwig, Analysis of process related factors to increase volumetric productivity and quality of biomethane with Methanothermobacter marburgensis, Appl. Energy. 132 (2014) 155–162. https://doi.org/10.1016/j.apenergy.2014.07.002.

[27] M. Prussi, M. Padella, M. Conton, E.D. Postma, L. Lonza, Review of technologies for biomethane production and assessment of Eu transport share in 2030, J. Clean. Prod. 222 (2019) 565–572. https://doi.org/10.1016/j.jclepro.2019.02.271.

[28] L. Jürgensen, E.A. Ehimen, J. Born, J.B. Holm-Nielsen, Utilization of surplus electricity from wind power for dynamic biogas upgrading: Northern Germany case study, Biomass and Bioenergy. 66 (2014) 126–132. https://doi.org/10.1016/j.biombioe.2014.02.032.

[29] P. Collet, E. Flottes, A. Favre, L. Raynal, H. Pierre, S. Capela, C. Peregrina, Techno-economic and Life Cycle Assessment of methane production via biogas upgrading and power to gas technology, Appl. Energy. 192 (2017) 282–295. https://doi.org/10.1016/j.apenergy.2016.08.181.

[30] J. Gorre, F. Ortloff, C. van Leeuwen, Production costs for synthetic methane in 2030 and 2050 of an optimized Power-to-Gas plant with intermediate hydrogen storage, Appl. Energy. 253 (2019) 113594. https://doi.org/10.1016/j.apenergy.2019.113594.

[31] D. Previtali, A. Vita, A. Bassani, C. Italiano, A.F. Amaral, C. Pirola, L. Pino, A. Palella, F. Manenti, Methanol synthesis: A distributed production concept based on biogas plants, Chem. Eng. Trans. 65 (2018) 409–414. https://doi.org/10.3303/CET1865069.

[32] M. Rivarolo, D. Bellotti, L. Magistri, A.F. Massardo, Feasibility study of methanol production from different renewable sources and thermo-economic analysis, Int. J. Hydrogen Energy. 41 (2016) 2105–2116. https://doi.org/10.1016/j.ijhydene.2015.12.128.

[33] R.O. dos Santos, L. de S. Santos, D.M. Prata, Simulation and optimization of a methanol synthesis process from different biogas sources, J. Clean. Prod. 186 (2018) 821–830. https://doi.org/10.1016/j.jclepro.2018.03.108.

[34] R. Gao, C. Zhang, Y.J. Lee, G. Kwak, K.W. Jun, S.K. Kim, H.G. Park, G. Guan, Sustainable production of methanol using landfill gas via carbon dioxide reforming and hydrogenation: Process development and techno-economic analysis, J. Clean. Prod. 272 (2020) 122552. https://doi.org/10.1016/j.jclepro.2020.122552.

[35] F.M. Baena-Moreno, L. Pastor-Pérez, Q. Wang, T.R. Reina, Bio-methane and bio-methanol co-production from biogas: A profitability analysis to explore new sustainable chemical processes, J. Clean. Prod. 265 (2020) 121909. https://doi.org/10.1016/j.jclepro.2020.121909.

[36] P.J. Megiá, A.J. Vizcaíno, J.A. Calles, A. Carrero, Hydrogen Production Technologies: From Fossil Fuels toward Renewable Sources. A Mini Review, Energy and Fuels. 35 (2021) 16403–16415. https://doi.org/10.1021/acs.energyfuels.1c02501.

[37] H. Project, L.C. Stages, U. Processes, D. Processes, O. Processes, R.M. Extraction, M. Production, M. Manufacture, Life Cycle Greenhouse Gas Emissions from Solar Photovoltaics, 2012.

[38] A. Moro, L. Lonza, Electricity carbon intensity in European Member States: Impacts on GHG emissions of electric vehicles, Transp. Res. Part D Transp. Environ. 64 (2018) 5–14. https://doi.org/10.1016/j.trd.2017.07.012.

[39] C. Antonini, K. Treyer, A. Streb, M. Van der Spek, C. Bauer, M. Mazzotti, Hydrogen production from natural gas and biomethane with carbon capture and storage – a techno-environmental analysis, Sustain. Energy Fuels. 4 (2020) 2697–2986. https://doi.org/10.1039/d0se00222d.

[40] C. Antonini, K. Treyer, E. Moioli, C. Bauer, T. Schildhauer, M. Mazzotti, Hydrogen from wood gasification with CCS - a techno-environmental analysis of production and use as transport fuel, Sustain. Energy Fuels. 5 (2021) 2602–2621. https://doi.org/10.1039/d0se01637c.

[41] IRENA AND METHANOL INSTITUTE, Innovation Outlook: Renewable Methanol, Abu Dhabi, 2021.

[42] I. Aloisi, A. Di Giuliano, A. Di Carlo, P. U. Foscolo, C. Courson, K. Gallucci, Chem. Eng. J. 2017, 314, 570–582. DOI: 10.1016/j.cej.2016.12.014.

[43] A. Borgschulte, N. Gallandat, B. Probst, R. Suter, E. Callini, D. Ferri, Y. Arroyo, R. Erni, H. Geerlings, A. Züttel, Phys. Chem. Chem. Phys. 2013, 15 (24), 9620–9625. DOI: 10.1039/c3cp51408k.

[44] J. Boon, K. Coenen, E. van Dijk, P. Cobden, F. Gallucci, M. van Sint Annaland, Sorption-Enhanced Water–Gas Shift, 1st ed., Vol. 51, Elsevier Inc. 2017.

[45] S. Guffanti, C. G. Visconti, J. van Kampen, J. Boon, G. Groppi, Chem. Eng. J. 2021, 404, 126573. DOI: 10.1016/j.cej.2020.126573.

[46] J. Terreni, M. Trottmann, T. Franken, A. Heel, A. Borgschulte, Energy Technol. 2019, 7 (4), 1–9. DOI: 10.1002/ente.201801093.

[47] P. Maksimov, A. Laari, V. Ruuskanen, T. Koiranen, J. Ahola, Chem. Eng. J. 2021, 418, 129290. DOI: 10.1016/j.cej.2021.129290.

[48] K. Fujimoto, Y. Yu, Elsevier Sci. 1993, 77, 393–396.

[49] J. van Kampen, J. Boon, M. van Sint Annaland, Adsorption. 2021, 27 (4), 577–589. DOI:

10.1007/s10450-020-00283-8.

[50] Bayat, M.; Dehghani, Z.; Rahimpour, M.R. Membrane/sorption-enhanced methanol synthesis process: Dynamic simulation and optimization. J. Ind. Eng. Chem. 2014, 20, 3256–3269, doi:10.1016/j.jiec.2013.12.007.

[51] Dehghani, Z.; Bayat, M.; Rahimpour, M.R. Sorption-enhanced methanol synthesis: Dynamic modeling and optimization. J. Taiwan Inst. Chem. Eng. 2014, 45, 1490–1500, doi:10.1016/j.jtice.2013.12.001.

[52] Nikolic, M.; Daemen, L.; Ramirez-Cuesta, A.J.; Xicohtencatl, R.B.; Cheng, Y.; Putnam, S.T.; Stadie, N.P.; Liu, X.; Terreni, J.; Borgschulte, A. Neutron Insights into Sorption Enhanced Methanol Catalysis. Top. Catal. 2021, 64, 638–643, doi:10.1007/s11244-021-01461-w.

[53] Kim, K.M.; Oh, H.T.; Lim, S.J.; Ho, K.; Park, Y.; Lee, C.H. Adsorption Equilibria of Water Vapor on Zeolite 3A, Zeolite 13X, and Dealuminated y Zeolite. J. Chem. Eng. Data 2016, 61, 1547–1554, doi:10.1021/acs.jced.5b00927.

[54] P. Maksimov, A. Laari, V. Ruuskanen, T. Koiranen, and J. Ahola, “Methanol synthesis through sorption enhanced carbon dioxide hydrogenation,” Chemical Engineering Journal, vol. 418, p. 129290, Aug. 2021, doi: 10.1016/j.cej.2021.129290.

[55] P. Maksimov, H. Nieminen, A. Laari, and T. Koiranen, “Sorption enhanced carbon dioxide hydrogenation to methanol: Process design and optimization,” Chemical Engineering Science, vol. 252, p. 117498, Apr. 2022, doi: 10.1016/j.ces.2022.117498.

[56] Y. Wang, “Measurements and Modeling of Water Adsorption Isotherms of Zeolite Linde-Type A Crystals,” Ind. Eng. Chem. Res., vol. 59, no. 17, pp. 8304–8314, Apr. 2020, doi: 10.1021/acs.iecr.9b06891.

[57] J. Van Kampen, J. Boon, and M. Van Sint Annaland, “Steam adsorption on molecular sieve 3A for sorption enhanced reaction processes,” Adsorption, vol. 27, no. 4, pp. 577–589, May 2021, doi: 10.1007/s10450-020-00283-8.

[58] J. van Kampen, J. Boon, F. van Berkel, J. Vente, and M. van Sint Annaland, “Steam separation enhanced reactions: Review and outlook,” Chemical Engineering Journal, vol. 374, pp. 1286–1303, Oct. 2019, doi: 10.1016/j.cej.2019.06.031.

[59] P. Azhagapillai, M. Khaleel, F. Zoghieb, G. Luckachan, L. Jacob, and D. Reinalda, “Water Vapor Adsorption Capacity Loss of Molecular Sieves 4A, 5A, and 13X Resulting from Methanol and Heptane Exposure,” ACS Omega, vol. 7, no. 8, pp. 6463–6471, Mar. 2022, doi: 10.1021/acsomega.1c03370.

[60] Z. Dehghani, M. Bayat, and M. R. Rahimpour, “Sorption-enhanced methanol synthesis: Dynamic modeling and optimization,” Journal of the Taiwan Institute of Chemical Engineers, vol. 45, no. 4, pp. 1490–1500, Jul. 2014, doi: 10.1016/j.jtice.2013.12.001.

[61] J. Terreni, M. Trottmann, T. Franken, A. Heel, and A. Borgschulte, “Sorption-Enhanced Methanol Synthesis,” Energy Tech, vol. 7, no. 4, p. 1801093, Apr. 2019, doi: 10.1002/ente.201801093.

[62] A. Borgschulte et al., “Sorption enhanced CO2 methanation,” Phys. Chem. Chem. Phys., vol. 15, no. 24, p. 9620, 2013, doi: 10.1039/c3cp51408k.

[63] A. Borgschulte et al., “Manipulating the reaction path of the CO 2 hydrogenation reaction in molecular sieves,” Catal. Sci. Technol., vol. 5, no. 9, pp. 4613–4621, 2015, doi: 10.1039/C5CY00528K.